NASA CR-72474
GA-8835

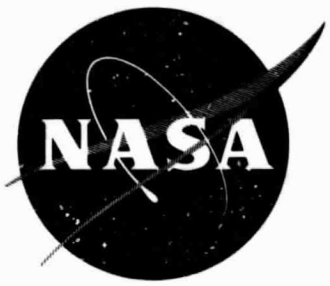

NEUTRON CAPTURE CROSS SECTIONS OF TUNGSTEN AND RHENIUM

by

W. M. Lopez, M. P. Fricke, D. G. Costello,
and S. J. Friesenhahn

Gulf General Atomic
Incorporated

prepared for

NATIONAL AERONAUTICS AND SPACE ADMINISTRATION

NASA Lewis Research Center
Contract NAS 3-11188
Sam Barile, Project Manager

NASA CR-72474
GA-8835

ANNUAL SUMMARY REPORT

NEUTRON CAPTURE CROSS SECTIONS OF TUNGSTEN AND RHENIUM

by

W. M. Lopez, M. P. Fricke, D. G. Costello,
and S. J. Friesenhahn

Gulf General Atomic
Incorporated
P.O. Box 608, San Diego, California 92112

prepared for

NATIONAL AERONAUTICS AND SPACE ADMINISTRATION

September 30, 1968

CONTRACT NAS 3-11188

Technical Management
NASA Lewis Research Center
Cleveland, Ohio
Nuclear Systems Division
Sam Barile, Project Manager
John C. Liwosz, Jr.

ABSTRACT

Neutron capture cross sections for natural tungsten and rhenium were measured from 1 to 700 keV energy using the time-of-flight technique. The neutron flux spectrum was monitored with ^{3}He proportional counters that were calibrated against measurements based on the $^{10}B(n,\alpha)^{7}Li$ cross section below 80 keV and on the n+p scattering cross section at higher energies. Some new data were also obtained for the reactions $^{3}He(n,p)T$ and $^{10}B(n,\alpha)^{7}Li$. The measured energy variation of the capture cross sections above 80 keV relies solely upon the n+p cross section and differs significantly from previous data based on other standard neutron cross sections.

SUMMARY

Neutron capture cross sections for natural samples of tungsten and rhenium were measured over the neutron energy range 1 to 700 keV using an electron LINAC pulsed neutron source, a 220-meter neutron flight path, and a liquid scintillator to detect the capture gamma rays. The cross sections were normalized to low-energy saturated resonances and were corrected for multiple scattering and resonance self-shielding. The over-all statistical uncertainty in the results is less than 10% at all energies, and the total uncertainty in the normalization of the cross sections is also about 10%.

The incident neutron flux was monitored by ^{3}He gas proportional counters whose response for different neutron energies was calibrated against that of other counters containing BF_3 and methane gas. The measured energy variation of the neutron flux is thus based on the cross section for the $^{10}B(n,\alpha)^{7}Li$ reaction for neutron energies below 80 keV, and on the n+p scattering cross section at higher energies. Some new data were also obtained for the $^{3}He(n,p)T$ cross section relative to the $^{10}B(n,\alpha)^{7}Li$ cross section, and for the $^{10}B(n,\alpha)^{7}Li$ cross section relative to the n+p scattering cross section. The present result for the $^{3}He(n,p)T$ cross section shows a more marked deviation from a (1/v)-behavior above 25-keV neutron energy than was indicated by previous data. The present result for the $^{10}B(n,\alpha)^{7}Li$ reaction is consistent with a (1/v) cross section extrapolated from the thermal value to about 200 keV.

Measurements of neutron flux with the methane counter were accomplished with a computer-based, on-line data acquisition system which permits a correlation of neutron flight time and proton-recoil energy. Since the proton energy spectrum varies with the neutron energy, such data are necessary to determine the efficiency of the counter (which varies with neutron energy for a fixed electronic threshold). The energy variation of the W and Re capture cross sections above 80-keV neutron energy could then be based on the exceedingly well known n+p scattering cross section, and the results differ significantly from previous data based on other standard neutron cross sections.

CONTENTS

ILLUSTRATIONS

ILLUSTRATIONS (Continued)

ILLUSTRATIONS (Continued)

1. INTRODUCTION

The objectives of the research program being conducted at Gulf General Atomic under Contract NAS3-11188 are:

1. To develop a methodology for accurate ($\leq$ 5%) measurements of relative and absolute neutron spectra in the energy range 1-400 keV.

2. To measure the absolute neutron capture cross sections of tungsten and rhenium with the following precisions:

   a. 1-100 keV: $\pm$10% in $\sigma(n, \gamma)$ and $\Delta E/E \leq 5\%$

   b. 100-400 keV: $\pm$15% in $\sigma(n, \gamma)$ and $\Delta E/E \leq 10\%$.

The first objective is a prerequisite for the second objective, since the determination of capture cross sections by the time-of-flight technique generally requires knowledge of the magnitude and energy dependence of the neutron flux used in the measurement. Historically, the precision of most capture cross-section measurements in the keV neutron energy range has been limited by the poor precision obtained in auxiliary measurements of the corresponding neutron flux. With the exception of the associated particle technique,[1] measurements of neutron flux must ultimately rely on a "standard" neutron cross section.

In this work, we rely on the hydrogen scattering cross section as the primary standard in the energy range 80 keV to 1 MeV. Using this standard cross section, we are attempting to improve the precision of the cross sections for the $^{10}B(n, \alpha)^{7}Li$ and $^{3}He(n, p)T$ reactions. The latter reaction is then used as an intermediate standard cross section for the purpose of continuously monitoring the neutron spectrum used in capture cross-section measurements.

In the following sections we describe the experimental facility (Section 2), the details of the equipment and techniques for the measurement of neutron flux (Section 3), and the procedures and results for the capture cross-section measurements for Re and W (Section 4).

2. EXPERIMENTAL FACILITY

2.1 NEUTRON SOURCE

Neutrons are generated by the (γ, n) reaction for time-of-flight experiments in the form of intense, short duration pulses by bombarding high-Z targets with bursts of 30- to 50-MeV electrons from the Gulf General Atomic linear accelerator. The electron burst width can be varied from 10 nsec to 5 μsec, which results in a neutron pulse of the same width provided the target is small and does not contain moderating materials. The neutron yield can be as large as $\sim 10^{11}$ neutrons/burst and has an energy spectrum very similar to that of a fission spectrum,[2] which peaks at $\sim$ 1 MeV.

The target will also emit a prompt, intense burst of bremsstrahlung radiation which can produce undesirable effects in the neutron detection systems used in time-of-flight experiments. Consequently, the targets are usually designed to enhance the neutron-to-bremsstrahlung ratio and to modify the neutron energy spectrum to suit the needs of a particular experiment.

For this program, we have designed a target configuration (shown in Fig. 1) which consists of a small water-cooled, fansteel target surrounded by a larger cylindrical lead shield. The lead shield serves the dual purpose of absorbing bremsstrahlung radiation and degrading the primary neutron energy spectrum by the inelastic scattering process. The capture cross section of lead is small ($\sim$ 4 mb at 500 keV),[3] so that neutron absorption in the lead shield is negligible. Figure 2 shows the calculated change in the primary energy spectrum due to the lead cylinder.

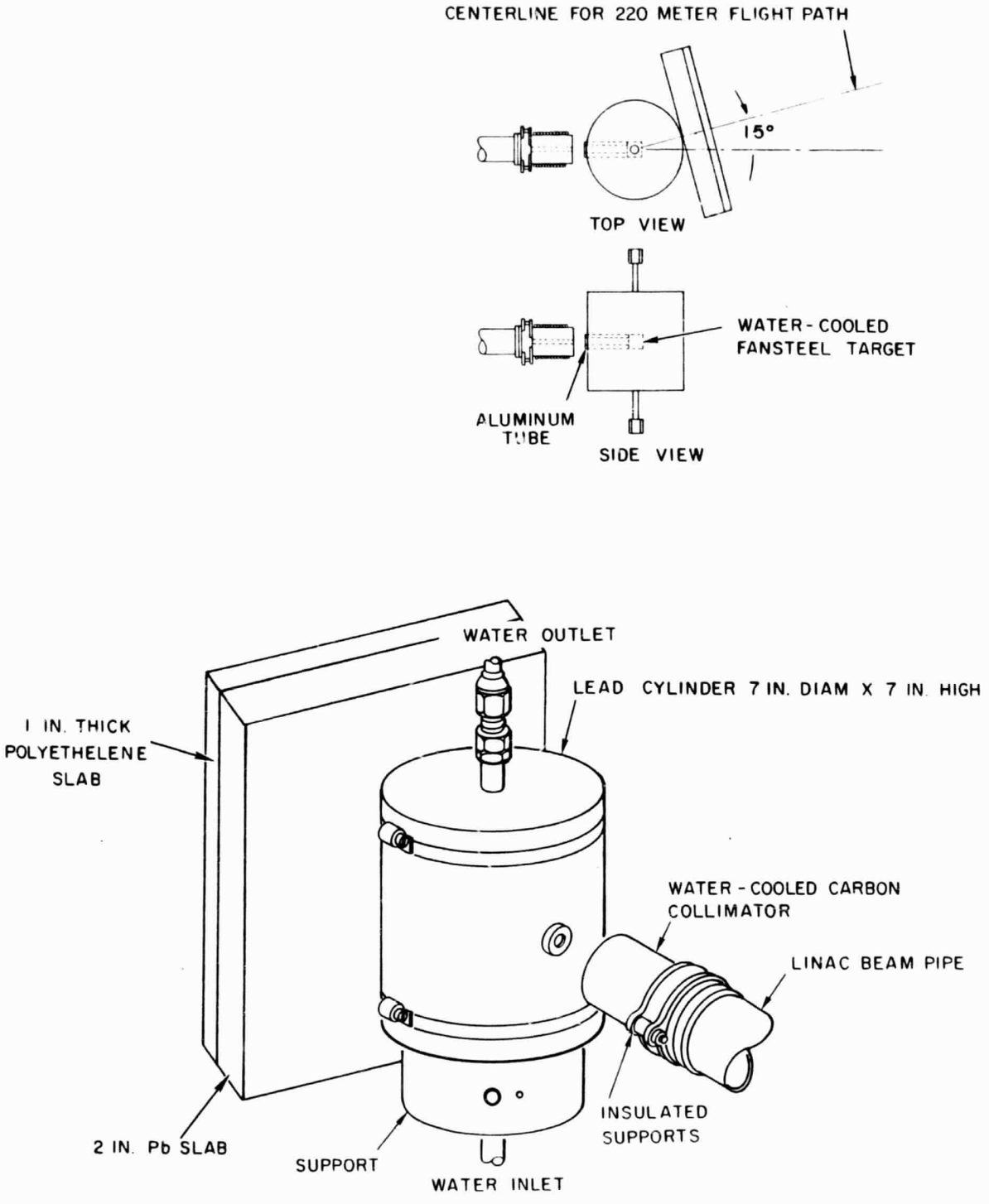

Figure 1. Neutron source configuration used with the 220-meter flight path facility.

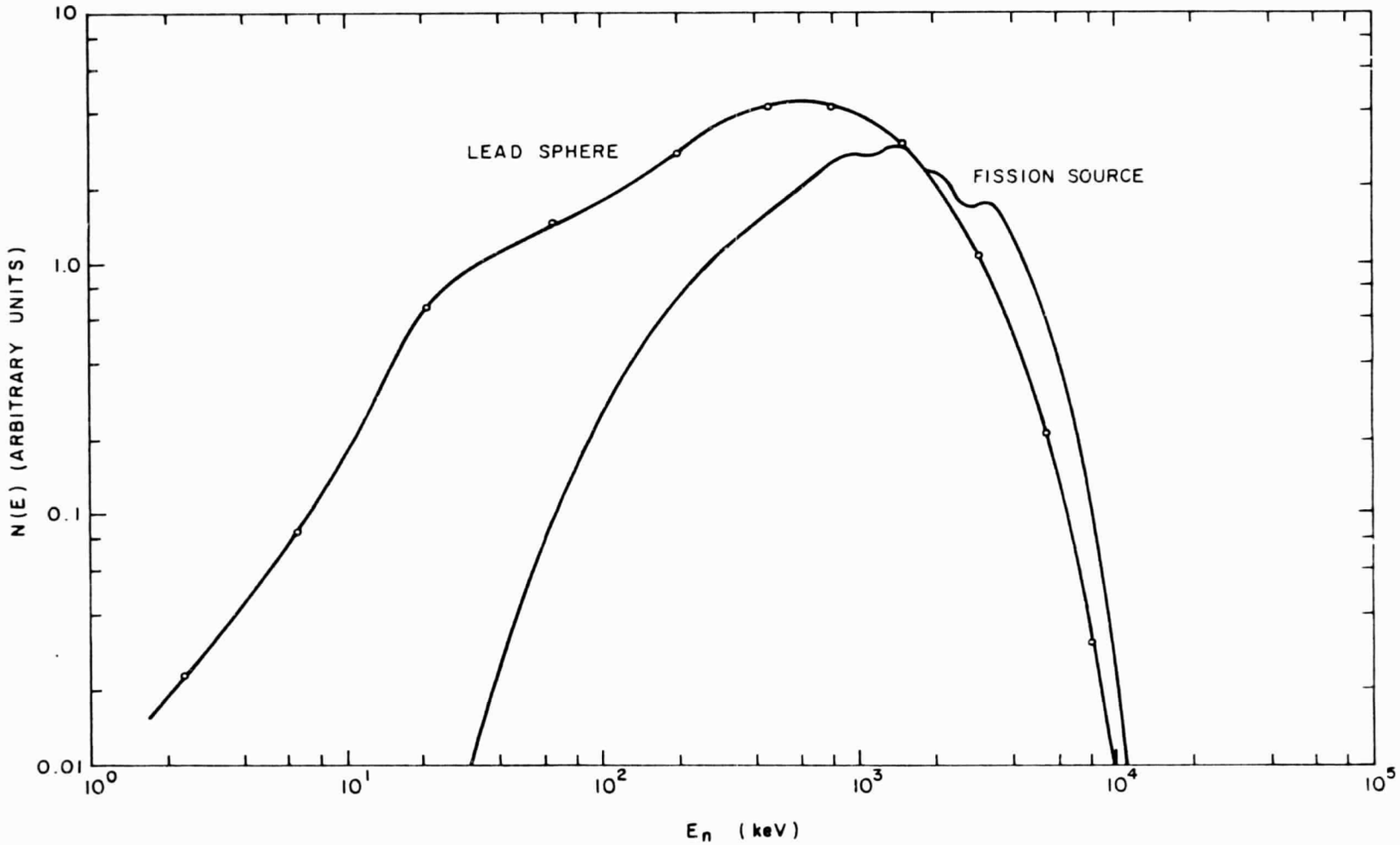

Figure 2. A calculation of the effect of a 7-in. (17.78-cm) diam lead sphere on a primary neutron energy spectrum (fission spectrum) from a point source located at the center of the sphere. The calculation was performed with the one-dimensional transport code 1DF.

τ also results in a constant fractional energy resolution related to an effective length uncertainty:

$$\Delta L = 4.2\,\Sigma_s^{\circ}/B^2 \simeq 12 \text{ cm.}$$

Consequently, for the 220-meter flight path, the lead cylinder limits the fractional energy resolution to $\sim 10^{-3}$ for neutron energies of $\gtrsim 1$ MeV. For lower energies the transmission of the polyethylene slab is low, and transmitted neutrons are degraded to energies where the time spread introduced by the lead is insignificant.

2.2 220-METER FLIGHT PATH

An aerial view of the evacuated neutron flight path used in this program is shown in Fig. 3. It consists of a 12-in. (30.48-cm) diameter section 385 ft (117.35 m) in length and a 24-in. (60.96-cm) diameter section 321 ft (97.84 m) in length. A vacuum of < 0.1 Torr. ($< 13 N/M^2$) is maintained over its entire length, and the entrance and exit windows consist of 12-mil (0.0305-cm) Mylar. The length of the flight path has been precisely measured by a team of professional surveyors who employed a geodimeter, a device based on optical interferometry. The calibrated distances along the flight path are permanently marked by brass plugs set in concrete slabs (see Fig. 4).

Various anti-scatter baffles are contained in the 12-in. and 24-in. diameter sections of the flight path. These restrict the beam diameter to 10 in. (25.4 cm) at the point of incidence on the first collimator, which is shown in Figs. 5 and 6. The first collimator reduces the beam diameter to 6 in. (15.24 cm), and the second and third collimators define a 4-in. (10.16-cm) diameter beam which passes through a 5-in. (12.7-cm) diameter drift tube located in the center of the liquid scintillator.

An aluminum container (7-in., or 17.78-cm, diameter) filled with ^{10}B powder (0.452 g/cm^2) was placed in front of the first collimator to

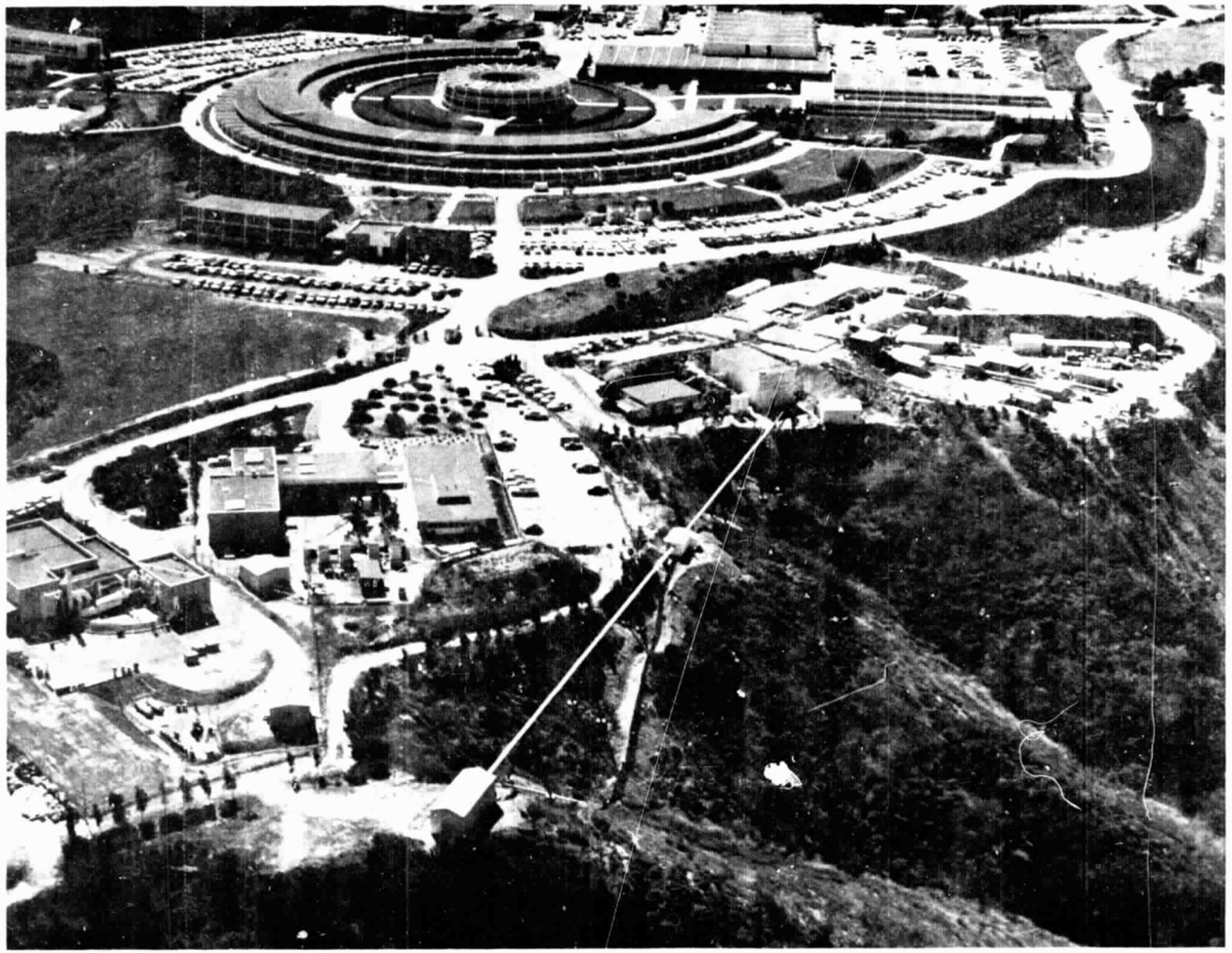

Figure 3. Aerial view of the 220-meter flight path emerging from the LINAC facility.

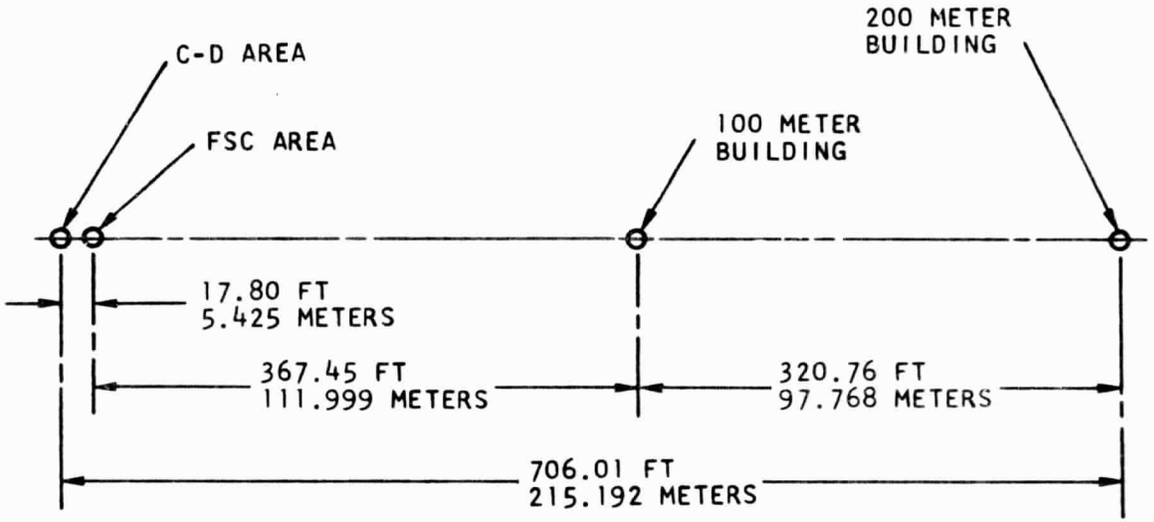

O INDICATES 1-1/4 IN. BRASS TABLET. MEASUREMENTS MADE BY ELECTRONIC METHODS USING A MODEL G GEODIMETER.

MEASUREMENTS BY M. H. GALER, OCTOBER 31, 1967

THE FOLLOWING ERROR OF EACH MEASUREMENT IS AS FOLLOWS:

706.01 ± 0.05 FT

320.76 ± 0.03 FT

367.45 ± 0.03 FT

17.80 ± 0.005 FT

Figure 4. Calibrated distances along the 220-meter flight path.

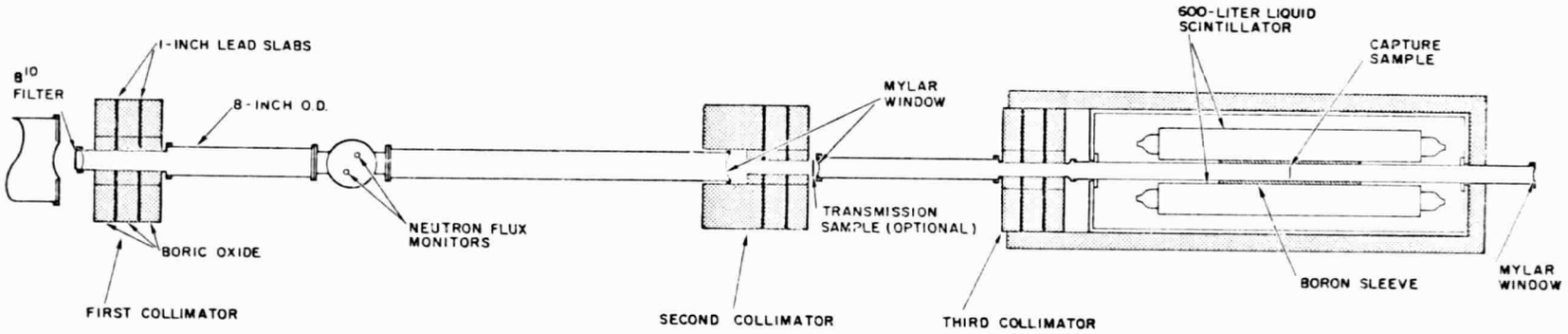

Figure 5. Collimators and vacuum system used with the 600-liter liquid scintillator for capture cross section measurements. The above apparatus is located at the end of a 220-meter evacuated neutron flight path.

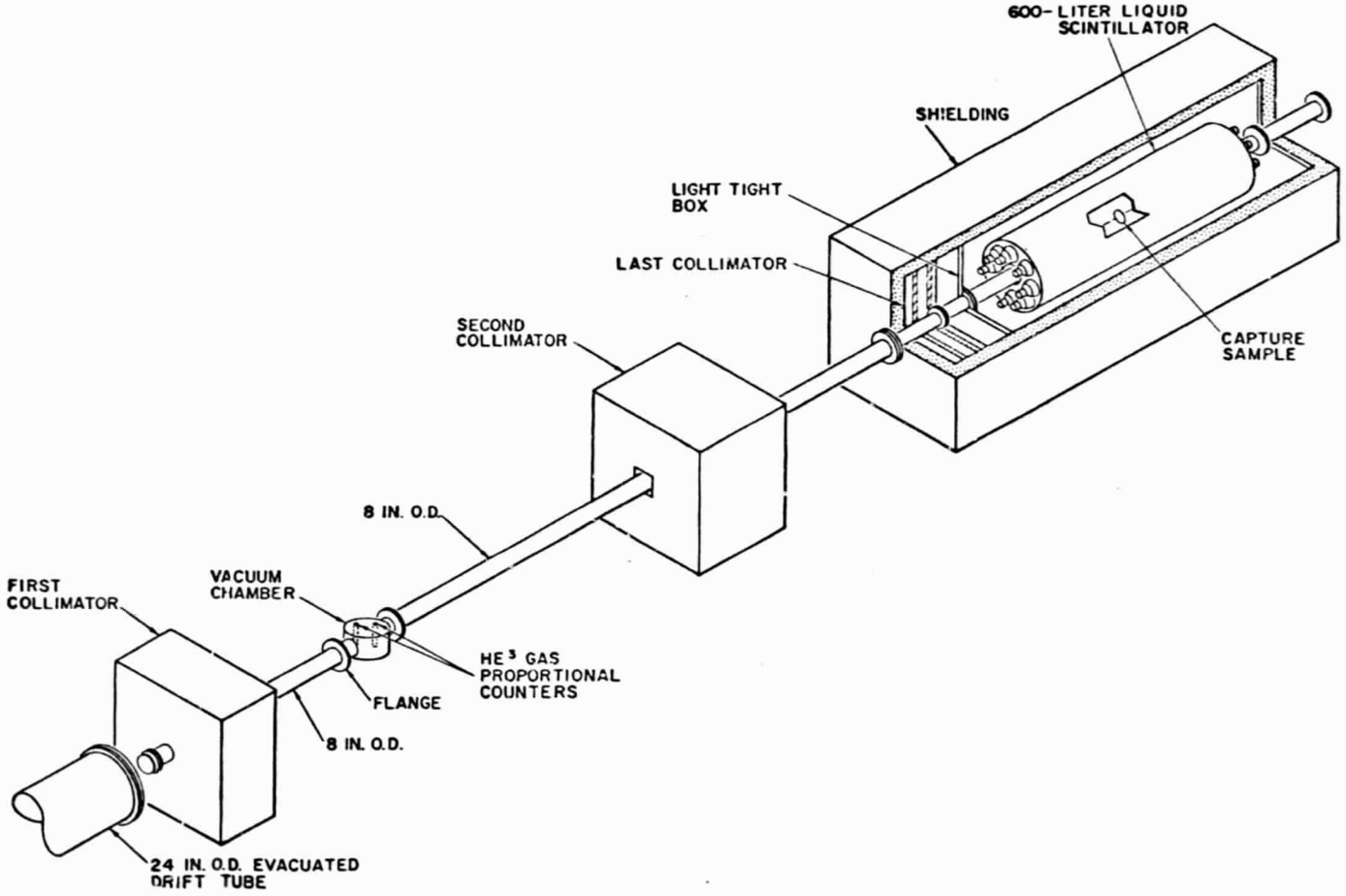

Figure 6. Facility for capture cross section measurements located at the end of the 220-meter evacuated neutron flight path.

remove neutrons with energies below 10 eV. This allowed operation of the LINAC at 180 pulse/sec repetition rate with no significant overlap of neutrons from previous pulses.

2.3 COMPUTER FOR DATA ACQUISITION

A CDC-1700 computer has been installed and serves as the central element in our "on-line" data acquisition system. Some of the features of this computer are:

1. 12 k-word magnetic core memory size,
2. 18 bits/word, which includes one parity bit and one memory protect bit,
3. 1.1-μsec memory cycle time,
4. 14 interrupt data channels, priority under program control,
5. 1.25×10^6-word storage in a removable magnetic disc-pack.

The capabilities for high-speed data acquisition, coupled with the large storage area of the magnetic disc, allow simultaneous storage of several time-of-flight spectra.

For this program, the data acquisition system is used to store capture cross-section data and neutron flux data obtained simultaneously at the 220-meter flight path with two separate detection systems: (1) a 600-liter liquid scintillator for the capture gamma rays, and (2) a bank of ^{3}He gas proportional counters for the neutrons. The detection systems are shown in Figs. 5 and 6 and described in Sections 3.5 and 4.1. The time-of-flight information from either detection system goes to a time encoder which generates binary numbers identifying the flight time of the observed events. These binary numbers are stored in the magnetic core memory of the computer via an interrupt data channel. Each detection

system uses a unique interrupt line, and the data are stored in separate arrays corresponding to each interrupt line. During the course of the experiment, the time information in these arrays is converted to energy, grouped into equal lethargy intervals ($\Delta\ell$nE), and displayed on an oscilloscope. At the end of a measurement, the information is transferred to the magnetic disc and stored until it is needed for further data processing.

For the measurements of neutron flux with the proton-recoil gas proportional counter, a two-parameter mode of data acquisition was used in which the neutron flight time and pulse height for each proton recoil event were stored as a pair of binary numbers. This mode of operation is described in more detail in Section 3.3.1.

For all the measurements discussed in the following sections, corrections for electronic dead time were made "automatically" by the various computer codes employed for data processing. In most cases, the data acquisition rates were so low that these corrections were negligible ($< 1\%$). Exceptions to this are measurements which employ the two-parameter mode of data acquisition. For these cases the analog-to-digital converter introduces a large, variable dead time. Consequently, the data accumulation rate was electronically limited to a maximum of one event per LINAC pulse to simplify the correction for missed events. Then the average data arrival rate was adjusted so that the magnitude of the correction was $\leq 20\%$ over the neutron energy range of interest.

3. NEUTRON FLUX MEASUREMENTS

Under the guidelines set forth in Task I, Paragraphs A, B, and C of Exhibit A of NAS3-11188, and as a result of the study of techniques for the measurement of fast neutron spectra as reported previously, the following methods were selected for use in the performance of Task II, the measurement of the neutron flux spectrum:

1. The $^{3}He(n, p)T$ reaction implemented by two or more gas proportional counters,

2. The $^{10}B(n, \alpha)^{7}Li$ reaction implemented by two or more gas proportional counters,

3. The hydrogen n-p scattering interaction implemented by one or more proton-recoil gas proportional counters.

The $^{3}He(n, p)T$ reaction was selected for the purpose of continuously monitoring the magnitude and energy dependence of the neutron flux during the capture gamma-ray measurements called for in Task III. The primary reason for this selection is that ^{3}He gas proportional counters are commercially available in small-diameter, high-pressure configurations which have performance characteristics (described in Sections 3.2 and 3.5) suitable for time-of-flight measurements. The small dimensions of a high pressure counter allow one to sample the outer edges of a collimated neutron beam with adequate detection efficiency while the central, unperturbed portion of the beam is used for the capture measurements. However, it was believed that the $^{3}He(n, p)T$ cross section was not known with sufficient precision to deduce the absolute magnitude and shape of the neutron flux over the entire energy range required for the capture

cross-section determinations of Task III.* Consequently, the $^{10}B(n,\alpha)^{7}Li$ cross section and the n-p scattering cross section are used as primary standards in the neutron energy regions 2 eV to 80 keV, and 80 keV to 700 keV, respectively. The response of the ^{3}He gas proportional counters (and hence the $^{3}He(n,p)T$ cross section) is then calibrated against the response of the counters which rely on the primary standards. The following subsections describe the experimental details, methods of analysis and resulting precisions for these intercalibration procedures.

3.1 BREMSSTRAHLUNG EFFECTS

One of the primary considerations in the selection of gas proportional counters for these measurements was the requirement of low sensitivity to the bremsstrahlung rays which accompany any LINAC pulsed neutron source. These rays are capable of inducing severe ionization of a detection medium and could give rise to long-term saturation effects in the detector and/or the associated electronic system.

In this work, the combination of a long flight path (~225 meters), a specially designed target configuration (Section 2.1), and the use of gas proportional counters has succeeded in reducing the bremsstrahlung problem to negligible proportions. For the three types of gas counters (^{3}He, $^{10}BF_3$, and CH_4) used in this work, the amplitude of the bremsstrahlung pulse, as observed at the output of the linear amplifier of the system, was always well within the dynamic range of the amplifier and less in amplitude than most pulses due to the neutron induced events (protons or alphas) used in the neutron flux measurements. Linearity

*Although the neutron energy range specified in Task III for the $\sigma_{n,\gamma}$ determinations is 1 keV to 400 keV, the normalization procedures used in this work require that the neutron flux be measured down to about 2 eV. These procedures are described in detail in Section 4.

checks of the pulse-height spectrum made as a function of time after the bremsstrahlung pulse fail to show any significant bremsstrahlung effects. These checks are discussed in Sections 3.3.1 and 3.5.

3.2 TIMING UNCERTAINTY OF GAS PROPORTIONAL COUNTERS

There is an inherent timing uncertainty or "time-jitter" in gas proportional counters which is due to the time required for electrons to migrate from the point of ionization to the region near the anode where gas multiplication takes place. The magnitude of this time jitter must be known to evaluate the neutron energy resolution of a particular time-of-flight neutron spectrum measurement.

The time jitter for the three types of gas proportional counters used in this work was measured directly with a 1-curie Pu-Be neutron source, and the delayed coincidence schemes used are illustrated by the block diagram in Fig. 7. These techniques have been described previously in detail.[7] The measurements give time jitters (see Fig. 8) of 2.5, 5.5, and 0.66 μsec for the ^{3}He, $^{10}BF_3$, and CH_4 gas counters, respectively. An estimate of the width of the time jitter distributions can also be obtained from the drift time necessary for electrons to migrate from the cathode to the anode in a cylindrical counter:[7]

$$t = \frac{1}{m} \frac{P}{V} \frac{r_c^2}{2} \ln \frac{r_c}{r_a} ,$$

where m is the electron mobility, P the gas pressure, V the applied voltage, r_c the cathode radius, and r_a the anode radius. Using the mobilities of ^{3}He and $^{10}BF_3$ gases obtained by Harling,[7] and a mobility of CH_4 gas deduced from the results of English and Hanna,[8] we find drift times of 2.3 ± 0.7, 5.8 ± 0.5, and ~ 0.4 μsec for the ^{3}He, $^{10}BF_3$, and CH_4 counters, respectively, for the voltage, pressure, and dimensions

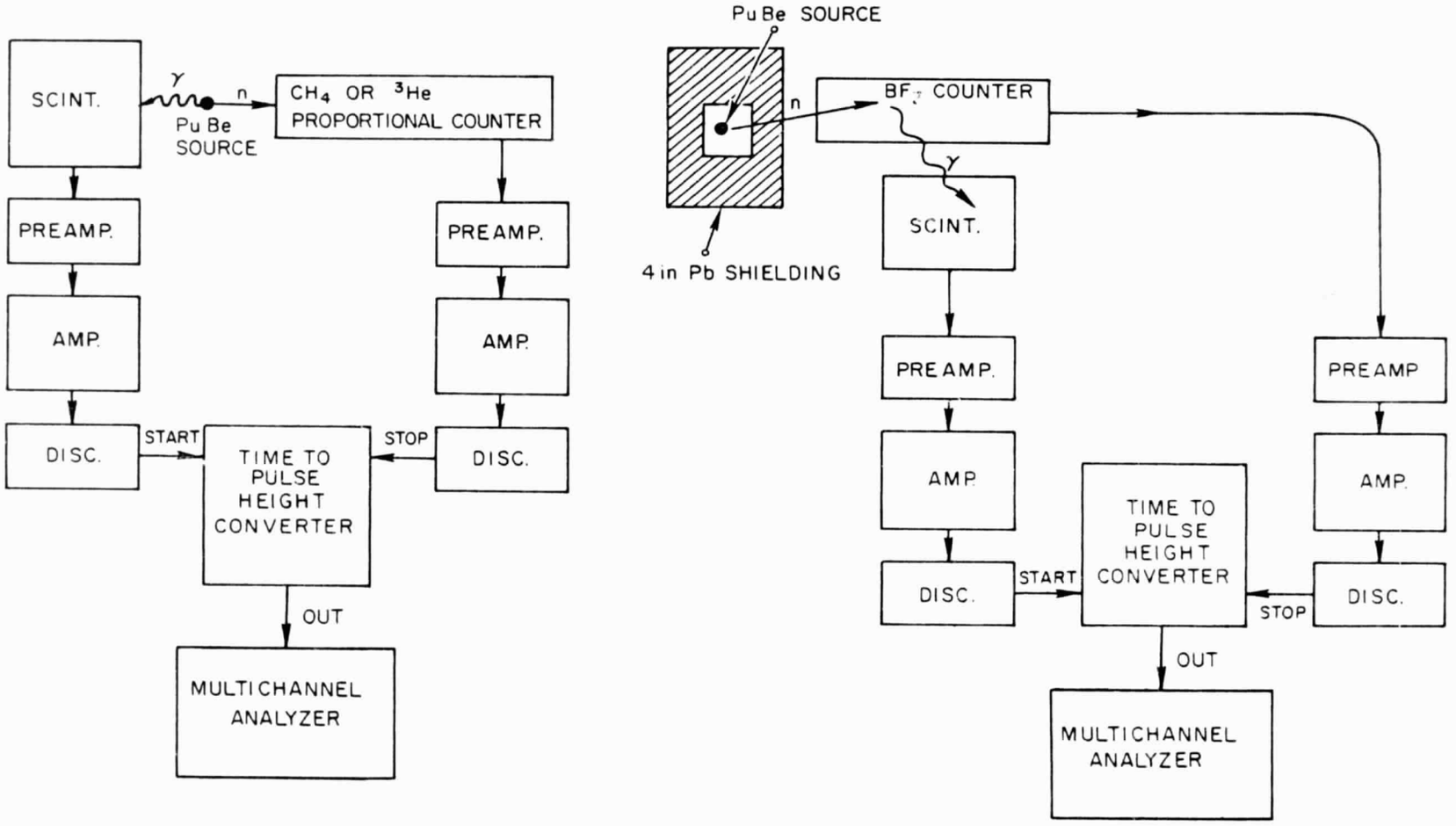

Figure 7. A simplified block diagram of the instrumentation used for time-jitter measurements of CH_4, ^3He, and $^{10}BF_3$ gas proportional counters.

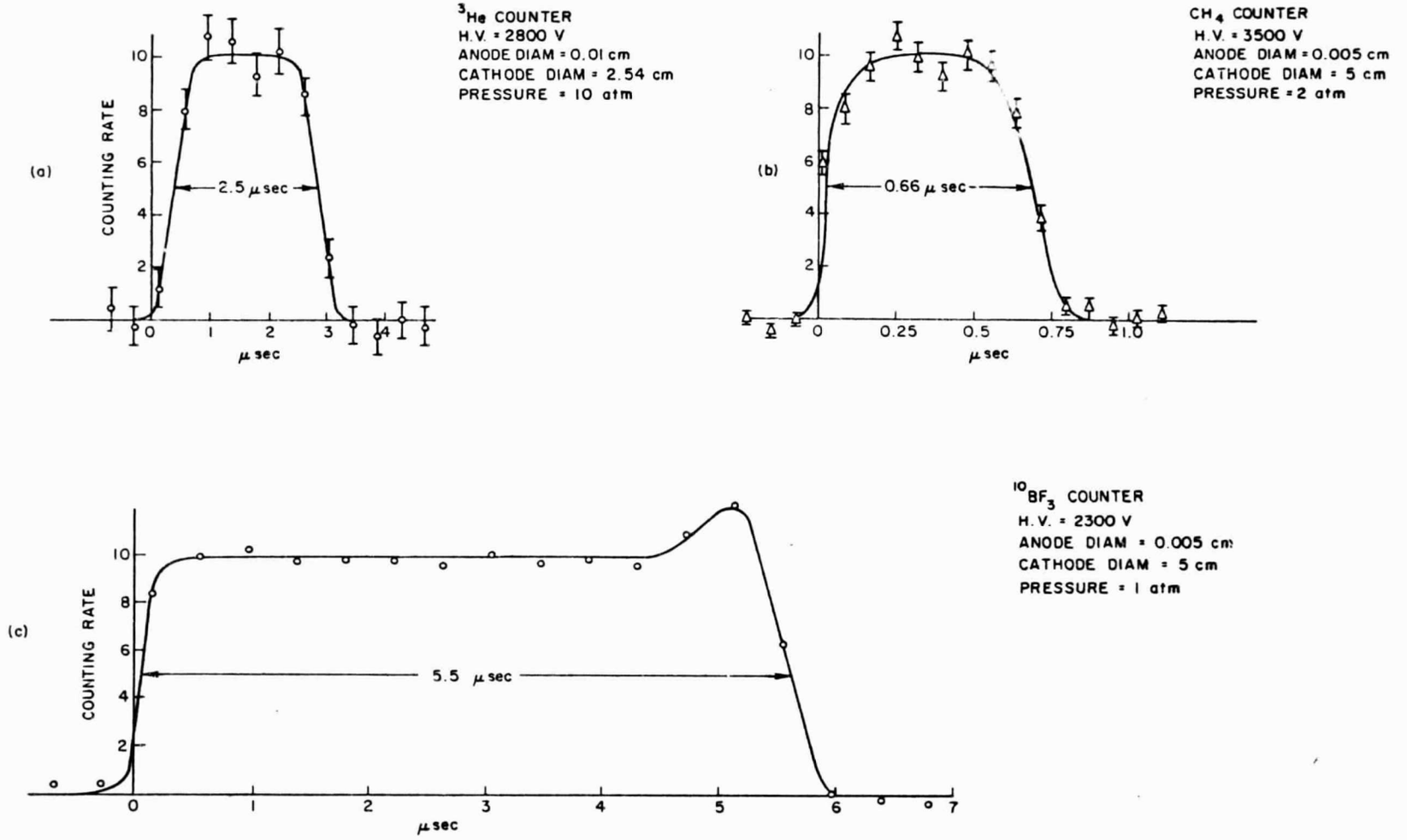

Figure 8. Measured time-jitter distributions of CH_4, ^3He, and $^{10}BF_3$ gas proportional counters.

given in Fig. 8. These estimates are in good agreement with our measured values.

3.3 PROTON-RECOIL GAS COUNTER

The n-p scattering cross section has been intensively investigated in fundamental studies of the nucleon-nucleon interaction. A description of the n-p interaction was developed by Schwinger[9] and Bethe[10] that agrees with experimental determinations to better than 1% over the entire energy range from thermal to 10 MeV.[11] Neutron capture is the only nonelastic channel open to the n-p interaction, and this reaction becomes negligible compared to elastic scattering at energies above thermal.[12] Consequently, there is much to support the conclusion that the n-p scattering cross section is presently the best standard cross section available for fast neutron physics. In principle this cross section could be used as a standard down to energies of a few keV. The actual limit of its usefulness at low energies is imposed by the practical problem of detecting low-energy protons.

In this work, n-p scattering was implemented for neutron flux measurements with a 2-in. (5.08-cm) diameter by 24-in. (60.96-cm) long gas proportional counter containing methane as the major part (94%) of the filling gas. Table 1 lists the pertinent details of the counter. The counts obtained from this counter per unit time-of-flight $\frac{dC}{dt}(E_n)$ at a time corresponding to the neutron energy E_n are related to the incident

Table 1

METHANE GAS COUNTER SPECIFICATIONS

Cathode:	2.00 ± 0.01-in. (5.08 ± 0.025-cm) o.d., 304 S.S., 0.036-in. (0.0914-cm) wall
Anode:	0.002-in. (0.005-cm) diam tungsten
End Window:	0.080-in. (0.203-cm) thick aluminum-oxide ceramic (Al_2O_3)
Connector:	HN, magnesium with Al_2O_3 insulator
Gas Filling:	Total pressure = 31.20 ± 0.16 PSIA (215,000 ± 1,000 N/m^2)

Constituents by Volume (%)	
Nitrogen	5.9 ± 0.2
Methane	94.0 ± 0.2
Oxygen	0.0012
Carbon Dioxide	0.0010
Argon	0.0032

Measured Active Length of Counter:	61.8 ± 0.6 cm	see text
Measured Time Jitter (FWHM):	0.66 μsec	
Operating Voltage:	3 to 3.5 kV	

neutron flux $\frac{d\varphi}{dt}(E_n)$ (neutrons per unit area per unit time-of-flight) by*

$$\frac{dC}{dt}(E_n) = T(E_n)\epsilon_b(E_n)\frac{d\varphi}{dt}(E_n)\,SN\,\sigma_{n,n}(E_n)\left[1-\delta(E_n)\right] + \frac{dB}{dt}(E_n)\,, \quad (1)$$

where ϵ_b is the detection efficiency for a given electronic discriminator threshold or "bias", S the area of gas intercepting the neutron beam, N the number of hydrogen nuclei per unit area, $\sigma_{n,n}$ the scattering cross section for the n-p interaction, $\frac{dB}{dt}$ the counts due to background, T the transmission of the alumina end window on the counter, and δ is a correction for self-shielding and multiple-scattering effects. The determination of the various quantities in Eq. 1 are discussed below.

3.3.1 Measurements of $\frac{dC}{dt}(E_n)$ and $\frac{dB}{dt}(E_n)$

To obtain the observable $\frac{dC}{dt}(E_n)$, the methane gas counter was located at position B shown in Fig. 9, where it views the central 2-in. (5.08-cm) portion of the 6-in. (15.24-cm) diameter neutron beam. The center of the counter is located 227.05 ± 0.05 meters from the neutron source, so that the neutron beam is essentially parallel over the length of the counter. A simplified block diagram of the electronics used with the methane counter is shown in Fig. 10. Since the counter contains a small quantity of nitrogen gas (~100 Torr. or 13,000 N/m^2), thermal neutrons from a moderated Pu-Be neutron source produce pulses corresponding to 616-keV deposited energy from the $^{14}N(n,p)^{14}C$ reaction. These pulses

---

*Here and elsewhere, we will write observed time-of-flight spectra simply as $\frac{dN}{dt}(E)$ when the spectra vary little over the time resolution Δt of the observation. It will also be understood that observed quantities written as $f(E)\frac{dN}{dt}(E)$ differ negligibly from

$$\frac{1}{\Delta t}\int_{t(E)-\Delta t/2}^{t(E)+\Delta t/2} f(\tau)\frac{dN}{dt}(\tau)d\tau\,,$$

where $E(t) = \frac{1}{2}m\left(\frac{L}{t}\right)^2$.

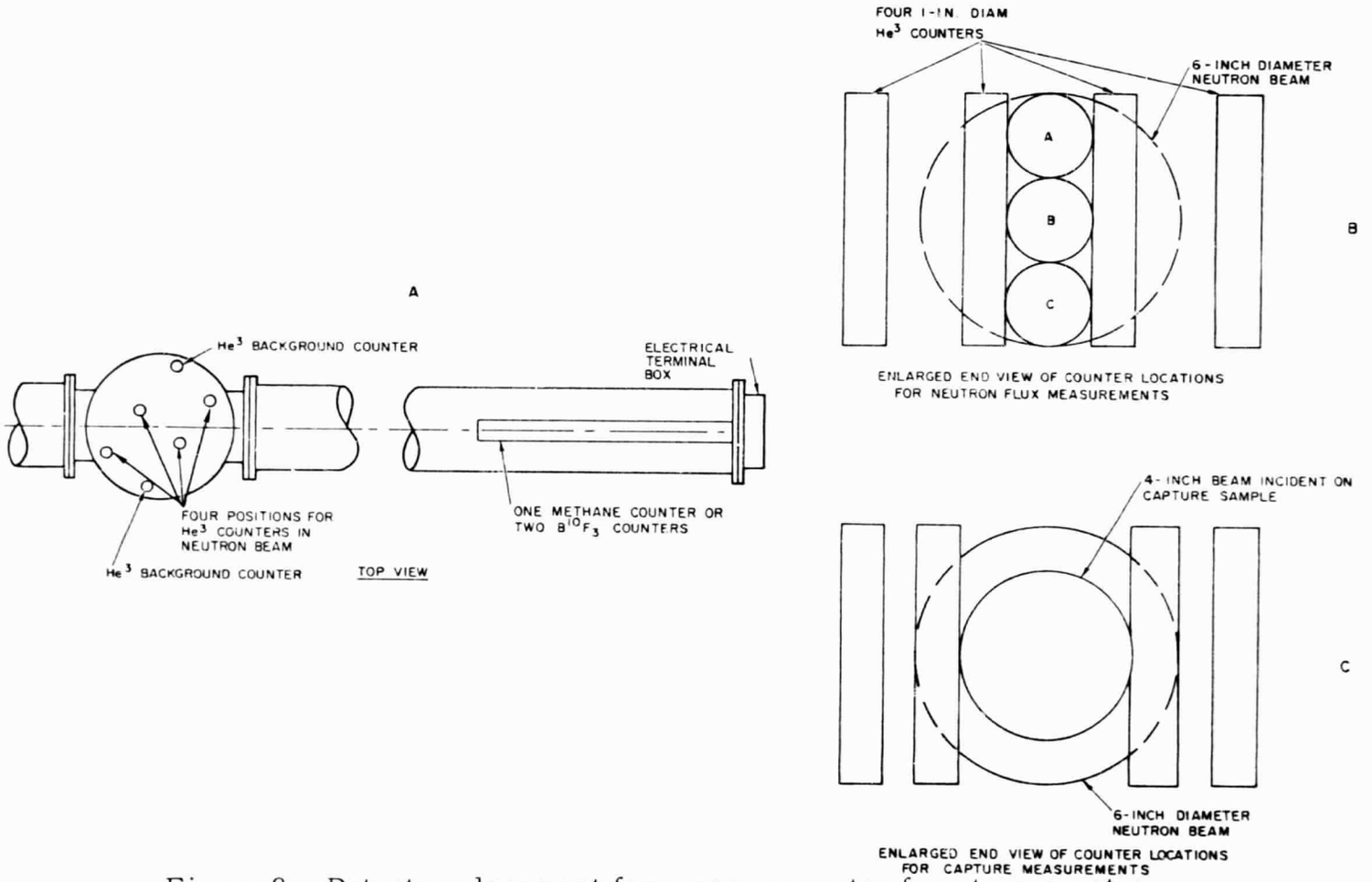

Figure 9. Detector placement for measurements of neutron spectra with the 220-meter facility.

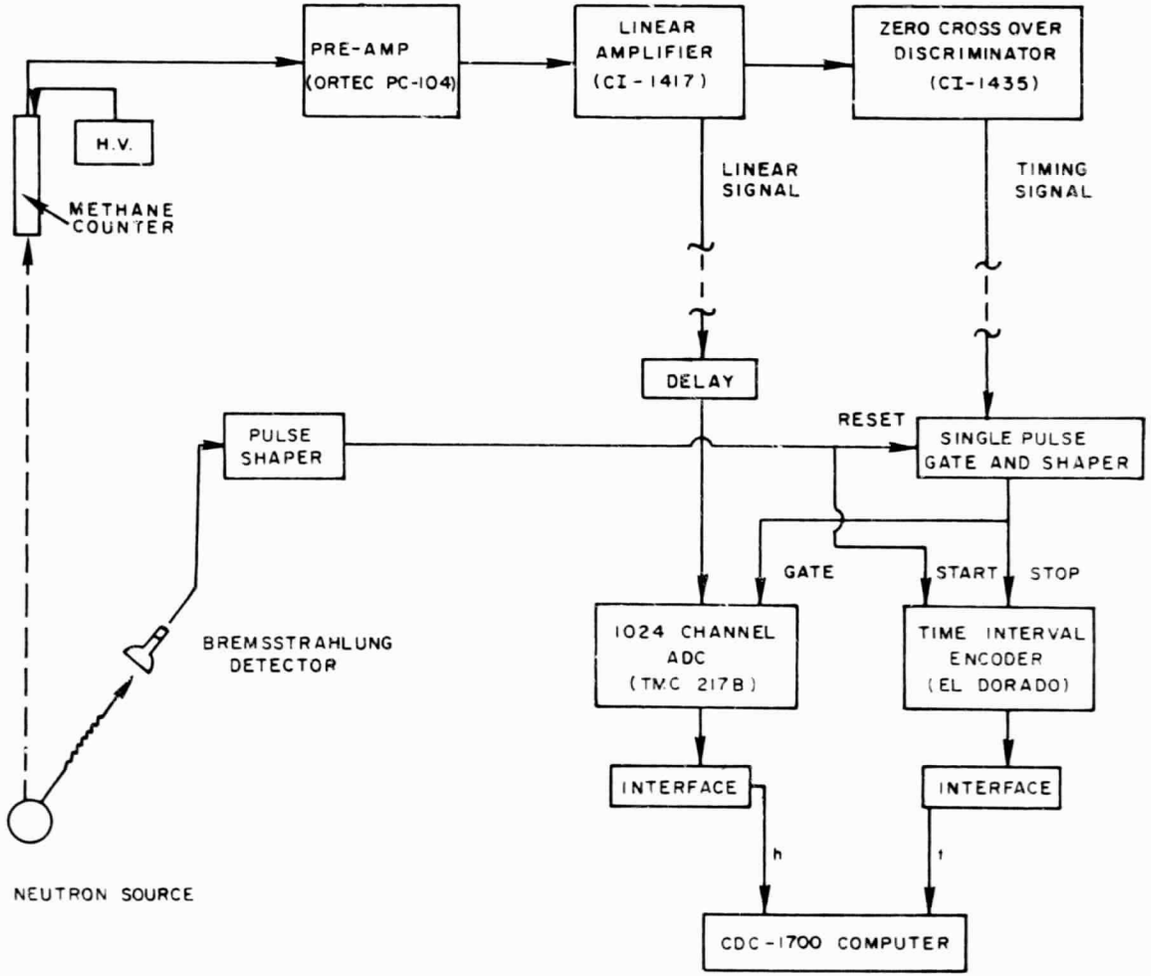

Figure 10. Simplified block diagram of electronics used with methane gas proportional counter.

were used to adjust the gain of the amplification system such that the 1024-channel analog-to-digital converter spans a pulse-height range equivalent to about 0-800 keV proton energy.

The pulse height h of events from the methane gas counter is stored in digital form by the data acquisition system together with the flight time t of the event relative to a reference pulse derived from the bremsstrahlung emitted by the pulsed neutron source. The energy E_n of the neutron causing the proton recoil event is related to the flight time, after correcting for any other time delays, by

$$E_n = \left[72.3\ (eV^{1/2}\ \mu s\ m^{-1})\ \frac{L}{t}\right]^2 , \qquad (2)$$

where L is the distance between the detector and the neutron source. Consequently, the events $\frac{d^2C}{dtdh}(t, h)$ that are sorted in two-parameter form in the computer can be sorted in such a way as to extract a proton-recoil pulse-height spectrum

$$\int_{t_1}^{t_2} \frac{d^2C}{dtdh}(t, h)dt$$

resulting from neutrons with energies between $E_1(t_1)$ and $E_2(t_2)$.

Figure 11 shows four typical recoil pulse-height spectra obtained in this manner. We note that at the higher neutron energies the pulse-height spectrum contains a contribution from carbon recoils that must be discriminated from the proton spectrum. Since the maximum recoil energy a neutron can impart to a carbon nucleus is about 28% of the neutron energy, and since the energy necessary to create an ion pair is about 40% greater for carbon ions than for protons,[13] we decided to accept all pulse heights equal to or greater than that equivalent to 0.3 times the maximum proton-recoil energy (see dotted lines in Fig. 11). The maximum

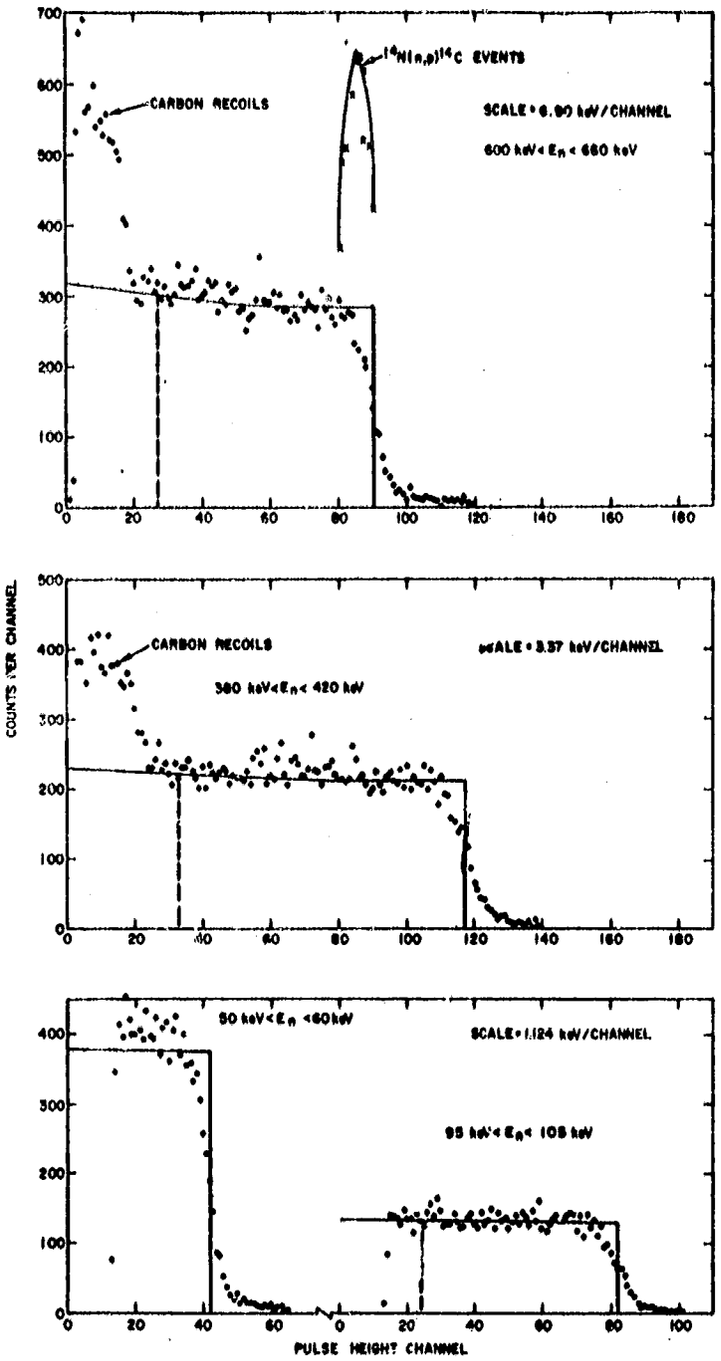

Figure 11. Proton-recoil pulse-height spectra obtained with methane gas proportional counter. The top inset shows the peak (x) obtained with thermal neutrons via the $^{14}N(n, p)^{14}C$ reaction. The solid curves are shapes of the proton-recoil spectra calculated with a Monte-Carlo computer code written by Parker, et al.[15]

observed proton-recoil pulse height h_{max} is a linear function of the neutron energy, namely

$$h_{max} = aE_n - b, \tag{3}$$

where b is related to the minimum proton energy in methane gas that results in ion pairs. The constants a and b are found by plotting h_{max} vs E_n (as shown in Fig. 12) and fitting a straight line to the data points. In this procedure, h_{max} is obtained from the 50% point on the high-energy edge of the recoil spectrum. (The linearity of the plot of h_{max} vs E_n shown in Fig. 12 gives further evidence that the counter does not suffer significantly from bremsstrahlung effects.) The minimum acceptable pulse height $h_{min}(t)$ can then be calculated as a function of flight time:

$$h_{min}(t) = 0.3\, aE_n(t) - b, \tag{4}$$

using the relation (2) between flight time and neutron energy.

The number of proton counts in the pulse-height spectrum above h_{min} for a given neutron energy interval (or flight-time interval) may then be sorted from the two-parameter events $\frac{d^2C}{dtdh}(t, h)$:

$$\frac{dC}{dt}(E_n)\Delta t = \int_{t-\frac{\Delta t}{2}}^{t+\frac{\Delta t}{2}} \int_{h^*}^{\infty} \frac{d^2C}{dtdh}(t, h)dhdt \equiv \epsilon_b(E_n) \int_{t-\frac{\Delta t}{2}}^{t+\frac{\Delta t}{2}} \int_{0}^{\infty} \frac{d^2C}{dtdh}(t, h)dhdt, \tag{5}$$

where h^* is the greater of h_{min} and the electronic threshold h_o used for the counter, and where again $E_n(t)$ is given by Eq. 2. In this work, it was convenient to sort the data using constant time intervals Δt as indicated above, and then to average the net count rate $\left(\frac{dC}{dt} - \frac{dB}{dt}\right)$ over equal lethargy intervals $\Delta E_n = 0.025\, E_n$. Methane gas counter data obtained this way are shown in Fig. 13.

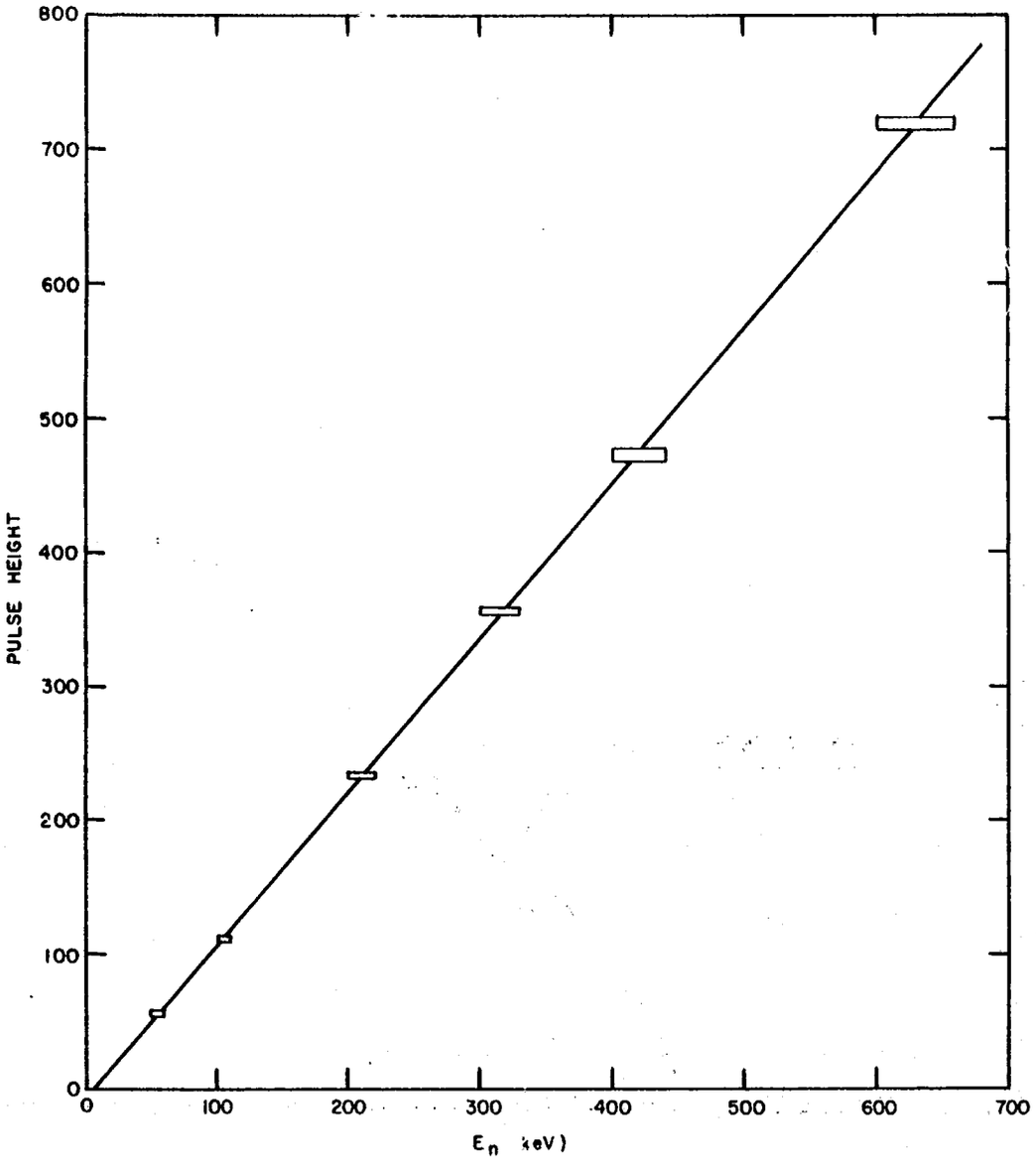

Figure 12. A plot of maximum pulse height vs incident neutron energy. The width of the rectangles are equal to the width of the neutron energy interval from which the pulse-height spectrum is obtained (see Fig. 11 for examples of pulse-height spectra). The height of the rectangles is equal to the uncertainty in defining the maximum pulse height, which is taken to be the 50% point on the high-energy side of the proton-recoil spectrum.

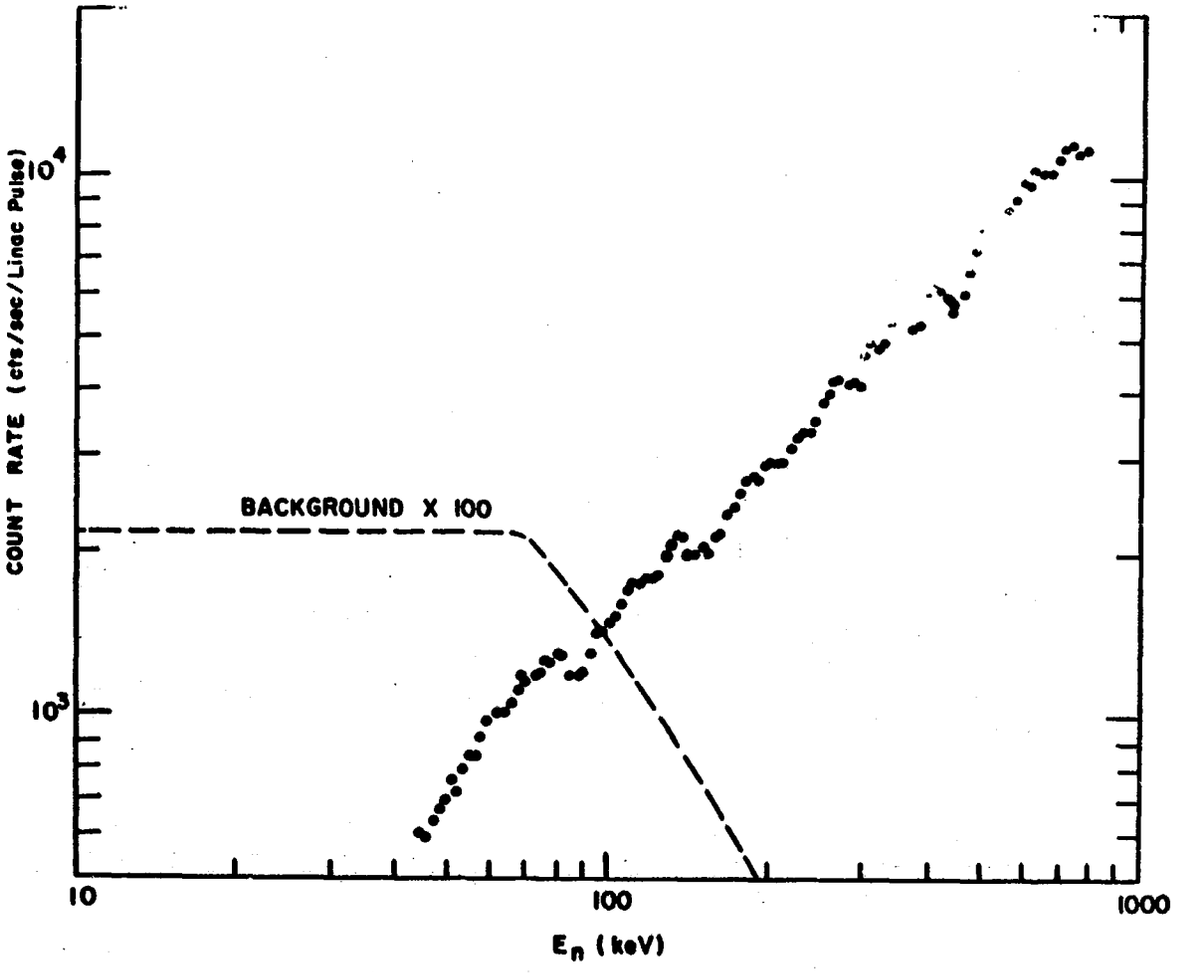

Figure 13. A plot of typical methane-counter time-of-flight data obtained with a 227-meter flight path, a 0.4 μsec LINAC burst width, a peak current of 350-mA, and an electron energy of 40 MeV.

The background count rate $\frac{dB}{dt}(E_n)$ subtracted from $\frac{dC}{dt}(E_n)$ is also shown in Fig. 13. At neutron energies greater than about 80 keV, $h_{min}(E_n) > h_o$ and the background decreases because the pulse-height spectrum of background events is essentially independent of neutron energy while the "sliding bias" $h_{min}(E_n)$ rejects more background pulses at higher neutron energies. The energy dependence of the background was checked in an auxiliary measurement by placing the methane gas counter outside the 8-in. (20.32-cm) o.d. drift tube but at the same flight-path distance used for the neutron flux measurements. Since this position is at least two meters from the concrete floor and the nearest collimator, the background due to the environment should not change over a distance ~12 cm. The background pulse-height spectrum was found to be independent of neutron energy and to have the exponential shape

$$\frac{d^2B}{dtdh}(h) = \frac{K}{\lambda}\exp(-h/\lambda)\,, \tag{6}$$

where K is a constant independent of energy and λ is a decay constant.

To find the background $\frac{dB}{dt}(E_n)$, for the methane counter in the neutron beam, the two-parameter data $\frac{d^2C}{dtdh}(t, h)$ were examined in the region 500 eV - 2 keV neutron energy, where there are essentially no proton-recoil events. After sorting these data into a pulse-height spectrum, the decay constant λ was determined by graphical means using Eq. 6. By sorting the same data into a time spectrum (for all observed pulse heights) the value of K was then established from the constant background $\frac{dB}{dt}$ observed at lower energies where $h_{min}(E_n) < h_o$:

$$\frac{dB}{dt} = \int_{h_o}^{\infty} \frac{d^2B}{dtdh}(h, t)\,dh = K\exp\left[-h_o/\lambda\right]. \tag{7}$$

The background could then be continued to higher energies and used to reduce the proton-recoil data:

$$\frac{dB}{dt}(E_n) = K \exp\left[-h_{min}(E_n)/\lambda\right], \quad h_{min} > h_o . \tag{8}$$

3.3.2 Wall Scattering Effects

Some of the background counts observed with the methane gas counter could be due to neutrons which are scattered by the counter wall into the gas volume. These events, if significant in number, would result in a contribution to the observable count rate $\frac{dC}{dt}(E_n)$ which is not accounted for by our methods of background determination described above and would therefore result in a systematic error in the neutron flux determined from Eq. 1.

An estimate of the wall scattering contribution was made as follows: (The counter geometry is illustrated in inset a of Fig. 14.) With the counter positioned so that its axis of symmetry is exactly parallel to the neutron beam, all neutrons incident on the frontal surface presented by the edge of the wall (ΔS) are scattered (absorption is negligible for stainless steel in the energy range of interest). A pessimistic assumption is that half of all these scattered neutrons enter the gas volume. Thus the count rate $\frac{dC'}{dt}$ due to these events satisfies

$$\frac{dC'}{dt} < \epsilon_b \frac{d\varphi}{dt} \frac{\Delta S}{2} \Sigma_s^H \bar{r} , \tag{9}$$

where ϵ_b and $\frac{d\varphi}{dt}$ were defined previously (Eq. 1), Σ_s^H is the macroscopic scattering cross section of hydrogen, and $\bar{r}$ is the average path length of the scattered neutrons in the gas volume. The scattered proton count rate $\frac{dC}{dt}$ is approximately (from Eq. 1)

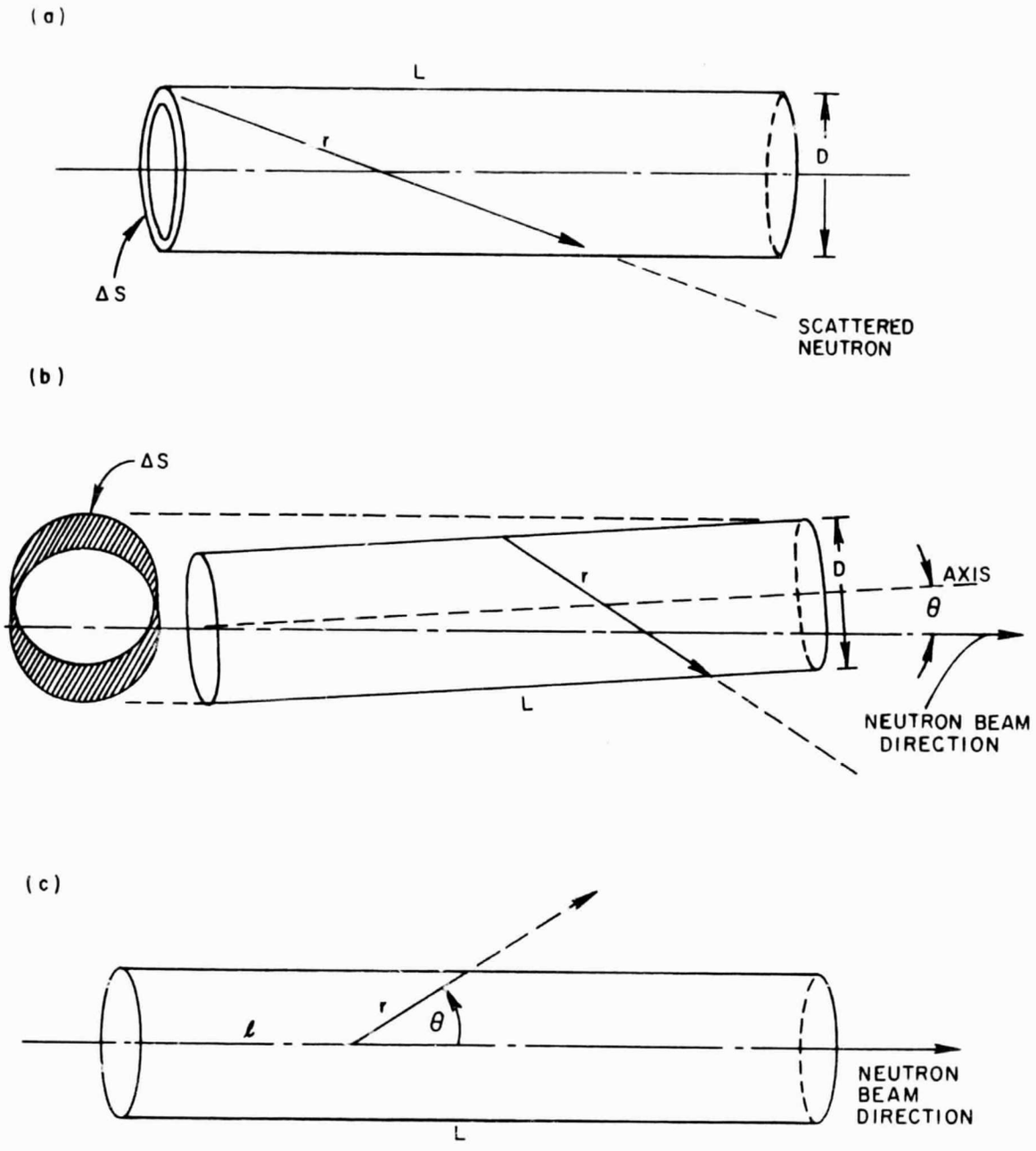

Figure 14. Drawings of the methane counter used to describe the calculation of wall-scattering effects (insets a and b) and multiple-scattering effects in the gas volume (inset c).

$$\frac{dC}{dt} \approx \epsilon_b \frac{d\varphi}{dt} LS \Sigma_s^H \ , \tag{10}$$

so that the fractional contribution of the wall scattering satisfies

$$\frac{dC'/dt}{dC/dt} < \frac{2t\bar{r}}{DL} \ , \tag{11}$$

where t is the wall thickness ($\sim$ 0.1 cm), D is the counter's diameter (5 cm), and L is the counter's active length ($\sim$62 cm). The average path length $\bar{r}$ can be estimated pessimistically by assuming all scattering to occur at the front edge of the wall (see inset a in Fig. 14) and by considering only the variation of path length which occurs in a plane containing the axis of the counter. One then obtains

$$\bar{r} < \frac{2}{\pi}\left[L \log \tan\left(\frac{\pi}{4} + \frac{D}{2L}\right) - D \log \tan\left(\frac{D}{2L}\right)\right] \ , \tag{12}$$

or $\bar{r} < 13.4$ cm. Substituting this value into Eq. 11, we obtain the result

$$\frac{dC'/dt}{dC/dt} < 0.009 \ .$$

Consequently, the wall scattering contribution is negligible provided the counter is properly aligned parallel to the neutron beam.

If the counter axis is misaligned by some small angle θ relative to the direction of the neutron beam, the counter wall presents a larger frontal area ΔS (see inset b of Fig. 14), which is approximately

$$\Delta S \approx 2 LD \sin\theta \ . \tag{13}$$

Since the effective thickness of wall material in the direction of the neutron beam is $(t/\sin\theta)$, Eq. 9 becomes

$$\frac{dC'}{dt}(\theta) < \epsilon_b \frac{d\varphi}{dt} LD \sin\theta \left[1 - \exp\left(-t\Sigma_s^W / \sin\theta\right)\right] \Sigma_s^H \bar{r}, \qquad (14)$$

where Σ_s^W is the macroscopic scattering cross section of the wall material (stainless steel). Eq. 11 then becomes

$$\frac{dC'/dt}{dC/dt} < \frac{4\bar{r}}{\pi D} \sin\theta \left[1 - \exp\left(-t\Sigma_s^W / \sin\theta\right)\right]. \qquad (15)$$

For this case it is more realistic to estimate the average path length $\bar{r}$ by assuming all scattering to occur at the midpoint of the counter length, and we consider again only variations of r in a plane containing the counter axis. Eq. 12 then becomes

$$\bar{r} \lesssim \frac{2}{\pi}\left[\frac{L}{2} \log \tan\left(\frac{\pi}{4} + \frac{D}{L}\right) - D \log \tan\left(\frac{D}{L}\right)\right], \qquad (16)$$

or $\bar{r} \lesssim 11$ cm. In our alignment procedure, a maximum error in alignment is estimated to be such that $\theta \lesssim 0.01$ radians, so that Eq. 15 gives

$$\frac{dC'/dt}{dC/dt} < 0.028 .$$

Consequently, we conclude that neutron flux measurements with the methane gas counter can contain a maximum systematic uncertainty of 3% due to neutron scattering by the counter walls.

3.3.3 Multiple Scattering and Self Shielding

The net count rate (Eq. 1) for the methane gas counter is

$$\frac{dN}{dt}(E_n) = \frac{dC}{dt}(E_n) - \frac{dB}{dt}(E_n) = T(E_n)\epsilon_b(E_n)\frac{d\varphi}{dt}(E_n) SN\sigma_{n,n}(E_n)\left[1-\delta(E_n)\right]$$

$$= T(E_n)\frac{d\varphi}{dt}(E_n) S \sum_i P_i , \qquad (17)$$

where P_i is the average probability for detected n-p scattering with i interactions. The multiple-scattering terms are difficult to evaluate because the detection efficiency and self-shielding effect for each interaction depend upon the amount of energy lost in previous collisions. However, an estimate of the maximum contribution from multiple scattering can be made by neglecting self-shielding and by assuming that recoil protons from all collisions are counted as separate events and detected with the same efficiency. The ratio of the count rate including multiple scattering $\frac{dN}{dt}(E_n)$ to the single-scattering count rate $\frac{dN_1}{dt}(E_n)$ satisfies

$$\frac{dN/dt}{dN_1/dt} = 1 + \frac{P_2}{P_1} + \frac{P_3}{P_1} + \dots , \tag{18}$$

and these assumptions yield the estimate

$$\frac{P_2}{P_1} < \Sigma_s^H(\overline{E}')\,\overline{r} , \tag{19}$$

where $\overline{r}$ is the average path length of the scattered neutron in the gas volume and Σ_s^H is the macroscopic scattering cross section for hydrogen at an average energy $\overline{E}'$ of the singly scattered neutron. The average path length was estimated by considering only neutron scattering along the axis of symmetry with an equal scattering probability along the length L (see inset c in Fig. 14):

$$\overline{r} \cong \frac{1}{L}\int_0^L\int_0^{\pi/2} r(\ell,\theta)P(\theta)d\theta\, d\ell , \tag{20}$$

where $P(\theta)$ is the probability of scattering at the lab angle θ for an isotropic center-of-mass n-p differential cross section. For the counter

used in this work, the above calculation yields $\bar{r} \simeq 4.6$ cm. Consequently, the ratio P_2/P_1 is less than 0.5% at an incident neutron energy of 1 MeV, and less than 1.3% at 100 keV.

Successive proton recoils from neutron multiple scattering in hydrogen occur so rapidly that they are counted as one pulse. The worst case that can occur is a first collision which results in a pulse below the bias h_{min} (as described in Section 3.3) followed by other collisions that result in a combined pulse which exceeds h_{min} and is counted. Since the fraction of these events is much smaller than the ratio P_2/P_1, we conclude that multiple-scattering effects in the proton-recoil data are entirely negligible. By similar considerations, one can also show that a first scattering with a carbon nucleus followed by a second scattering with a hydrogen nucleus also constitutes a negligible fraction ($P_2/P_1 < 1\%$) of the total counting rate. We therefore have

$$\sum_i P_i = \epsilon_b(E_n) N \sigma_{n,n}(E_n) \Psi(E_n) \ , \qquad (21)$$

where $\Psi(E_n)$ is a correction for self-shielding.

The correction $\left[1 - \delta(E_n)\right]$ in Eq. 1 thus reduces to simply a correction for the attenuation of the neutron flux as it passes through the counter of length L:

$$1 - \delta(E_n) = \Psi(E_n) = \left[L\Sigma_t(E_n)\right]^{-1} \left\{1 - \exp\left[-L\Sigma_t(E_n)\right]\right\} \ , \qquad (22)$$

where Σ_t is the macroscopic total cross section of the gas medium. This self-shielding correction was calculated for the methane counter using the total cross sections for hydrogen[11] and carbon,[14] and a plot of $\left[1-\delta(E_n)\right]^{-1}$ vs E_n is shown in Fig. 15.

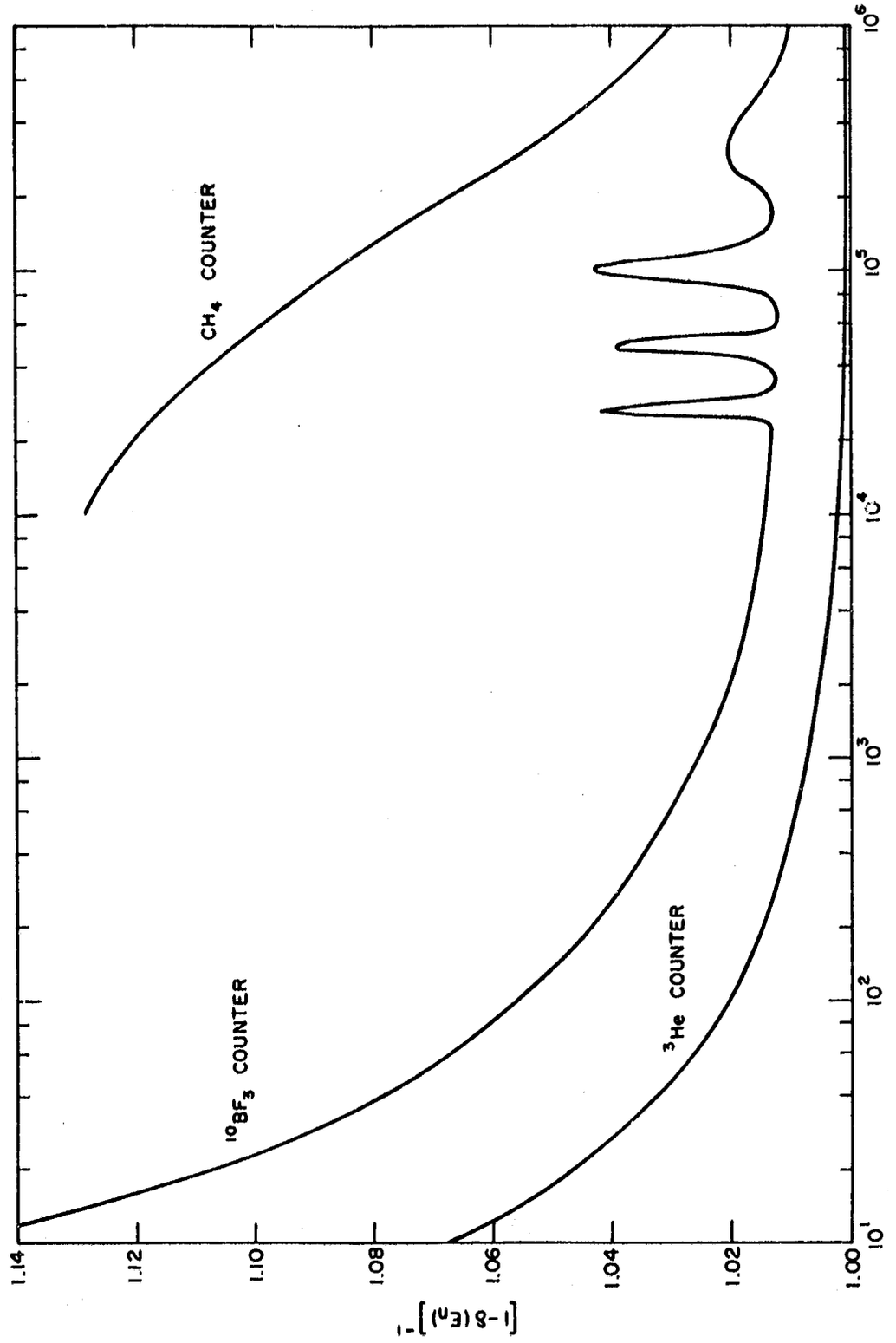

Figure 15. A plot of the self-shielding correction factor vs E_n for CH_4, ^3He, and $^{10}BF_3$ gas counters.

3.3.4 Active Volume Determination

The active volume of gas (the electron multiplying region of the counter) is defined on one end by the aluminum-oxide ceramic window. The other end of the counter contains an electrode assembly which produces an ill-defined region in which the gas multiplication drops to zero. The spatial extent of this region was measured to determine the total active volume (SL) and its uncertainty. This was accomplished by using a counter identical to the methane counter in mechanical and electrical configuration but which was filled with two atmosphere of Xenon gas. The heavy-gas filling allows one to employ a well collimated, low-energy gamma-ray beam for gas multiplication measurements over the length of the counter and in the vicinity of the active volume boundaries. Figure 16 shows the experimental setup as well as the results of these measurements. The length of the active volume of the counter was determined to be 61.8 cm with an estimated uncertainty of 1%.

The gas density was calculated from the temperature and pressure data (see Table 1) supplied by the manufacturer of the counter (Harshaw Chemical Company). The value obtained is 4.90×10^{-5} methane molecules per barn-cm with an estimated uncertainty of 0.3%. The uncertainty in the density is primarily due to the uncertainty in the methane concentration, which was obtained by a mass-spectrometer analysis of a sample of the gas. The sample was drawn from the same bottle that was used to fill the counter.

3.3.5 Spectrum Fraction Determination

In Section 3.3.1, a "sliding bias" $h_{min}(E_n)$ was described which was implemented in the computerized data handling procedure to reject that portion of the pulse-height spectrum which contains carbon recoil events. To infer what fraction $\epsilon_b(E_n)$ of the total proton-recoil spectrum

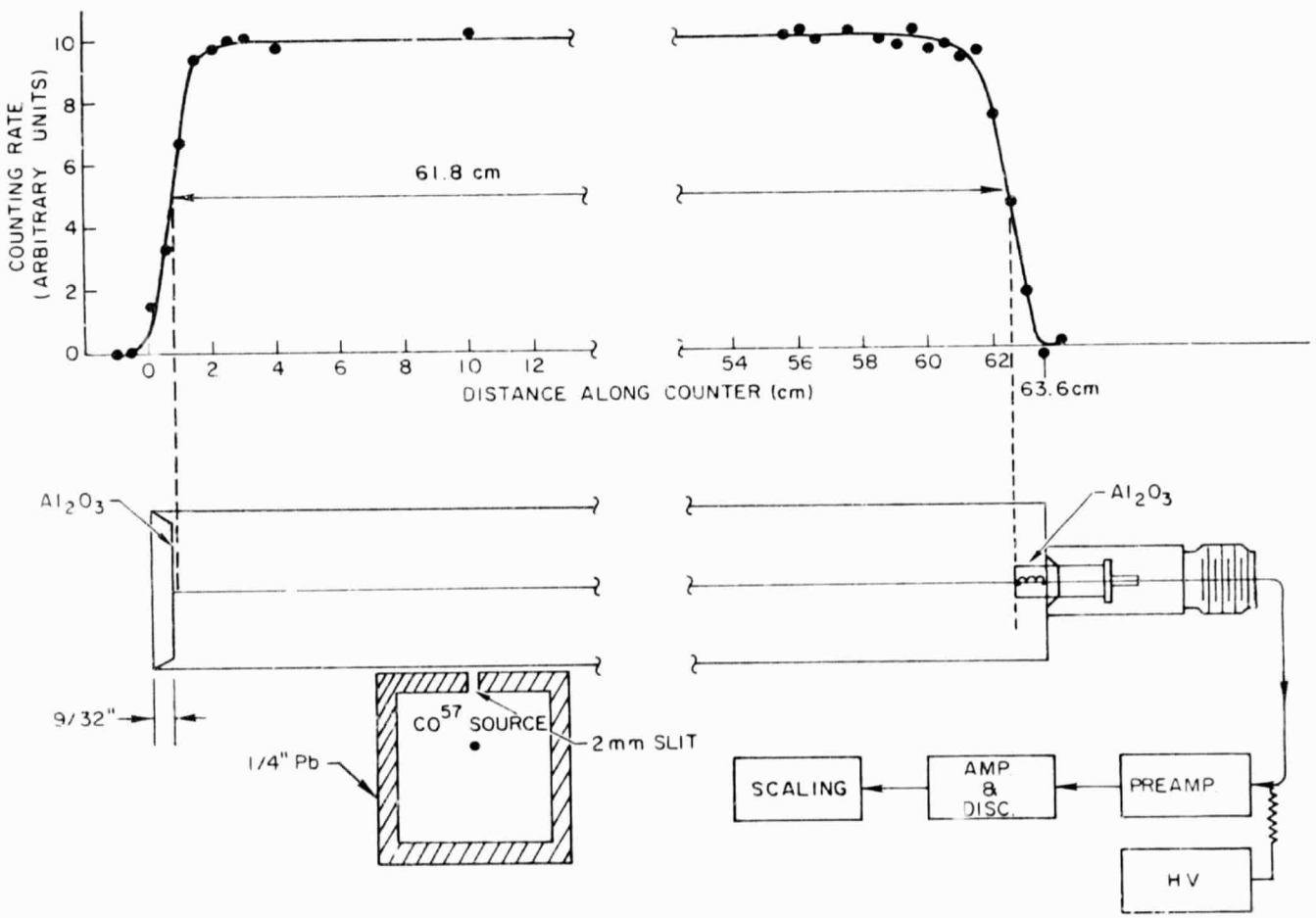

Figure 16. Diagram of the experimental configuration used to determine the active length of a gas proportional counter. The upper curve was obtained with a Xenon-gas proportional counter which had dimensions identical to the methane-gas counter used for neutron spectrum measurements.

lies above the bias (h_{min} is shown as a dotted line in Fig. 11), we performed calculations of the proton pulse-height spectrum for our counter geometry at various incident neutron energies with a Monte Carlo computer code written by Parker, et al.[15] Four calculated spectra are shown in Fig. 11. The shapes of the spectra $y(E_p)$ are essentially trapezoidal, and the ratio $y(E_{p_{max}})/y(0)$ decreases linearly with increasing neutron energy. The calculated behavior of the recoil-protron spectra (shown as solid curves in Fig. 11) agrees very well with the observed spectra for $E_n \geq 100$ keV, where the background is small. Using this energy-dependent trapezoidal shape, the spectrum fraction was found to be, within an uncertainty of about 2%,

$$\epsilon_b(E_n) = 0.70\left[1 - \eta(E_n)\right] , \tag{23}$$

where $\eta(E_n)$ varies linearly from zero at 70-keV neutron energy to 0.05 at 1 MeV.

3.3.6 End-Window Transmission

The end window of the methane gas counter is composed of 0.08-in. (0.203-cm) thick aluminum oxide ceramic. This material scatters a significant fraction of the incident neutron beam, particularly in the region of the strong aluminum resonances at 35 and 88 keV and near the oxygen resonance at 440 keV. Consequently, the net count rate $\langle \frac{dN}{dt}(E_n) \rangle$ averaged over equal lethargy intervals (as shown in Fig. 13) must be corrected for the end-window transmission. Since the flux varies little over the interval of averaging, the correction can be made by simply dividing the averaged count rate by the average transmission $\langle T(E_n) \rangle$ of the end window,

$$\langle T(E_n) \rangle = \int_{E_n-4W}^{E_n+4W} e^{-\Sigma_t(E')x} r(E_n, E')dE' . \tag{24}$$

The quantity Σ_t is the macroscopic total cross section of the alumina window, x is the thickness of the window, and r(E, E') is a Gaussian resolution function which approximates the energy resolution of the measurement,

$$r(E_n, E') = \frac{1}{W\sqrt{\pi}} \exp\left[-\frac{(E_n - E')^2}{W^2}\right] . \qquad (25)$$

The calculation of the resolution width W is described in Ref. 16, and in this case W includes the width of the energy interval used for the average $\langle dN/dt \rangle$. The magnitude of the transmission correction is about 8% over most of the energy range of the methane data, except at 88 keV and 440 keV where it is about 25%. The small-angle scattering from the window into the counter volume was calculated and found to give a negligible ($\lesssim$ 0.2%) contribution to dN/dt.

3.3.7 Neutron Scattering Cross Section for Hydrogen

The n-p scattering cross section calculated by Gammel[11] was used to deduce the neutron flux spectrum $\frac{d\varphi}{dt}(E_n)$ from the methane counter data. Gammel's analytical calculation is based on the central-force effective range approximation[9, 10] and yields values that agree to better than 1% with measured values of the hydrogen total cross section. Although there are no accurate measurements of the n-p cross section in the range 2 keV - 1 MeV, the calculated cross section is assumed to represent the true cross section in this range to an accuracy of 1%. For neutron energies above 100 keV, the table of values given by Gammel[11] are used with linear interpolation. Below 100 keV, we use his analytical expression

$$\sigma_{n,n}(E_n) = 3\pi\left[1.206\ E_n + (-1.86 + 0.09415\ E_n + 1.306\cdot 10^{-4}\ E_n^2)^2\right]^{-1}$$

$$+ \pi\left[1.206\ E_n + (0.4223 + 0.13\ E_n)^2\right]^{-1} , \quad E_n \text{ in MeV.} \qquad (26)$$

3.3.8 Results of Measurements

With the measured observables dC/dt and dB/dt, and all the other necessary quantities in Eq. 1 now determined, one can solve for the neutron flux $\frac{d\varphi}{dt}(E_n)$ with a precision of about 4%, not including the statistical uncertainty in dC/dt. A summary of all the systematic sources of error discussed above (Sections 3.3.2 - 3.3.6) is presented in Table 2.

Table 2

SYSTEMATIC UNCERTAINTIES IN METHANE COUNTER DATA

1.	Wall Scattering	< 3%
2.	Multiple Scattering	< 1%
3.	Active Volume	1%
4.	Spectrum Fraction	2%
5.	Gas Density	0.3%
6.	End-Window Small-Angle Scattering	0.2%
7.	Hydrogen Scattering Cross Section	1%
8.	Net Uncertainty	4%

An estimate of the time necessary to obtain a given statistical precision in the flux measurement can be obtained from the count-rate data shown in Fig. 13. The total number of counts ΔC in the interval Δt corresponding to the interval $\Delta E_n = 0.025\ E_n$ is related to the total number of LINAC pulses ρ by

$$\Delta C = \rho \Delta t(E_n) \left\langle \frac{dC}{dt}(E_n) \right\rangle , \tag{27}$$

where the brackets denote the average over Δt. Using Eq. 2 for the relationship $t(E_n)$, we have

$$\Delta C = \left\langle \frac{dC}{dt}(E_n) \right\rangle (2.03 \times 10^{-4} \text{sec eV}^{-\frac{1}{2}}) E_n^{\frac{1}{2}} \rho . \tag{28}$$

For a precision of 3% ($\Delta C \sim 1000$ cts) and a count rate of $dC/dt \sim 1000$ cps at 70 keV (from Fig. 13), we find that about 1.6×10^6 LINAC pulses are required, or about $2\frac{1}{2}$ hours at 180 pulses/sec repetition rate. Consequently, we see that a precision of 2-3% in the measured quantity are easily obtainable, and hence we can obtain an over-all precision of about 5% in the neutron flux determination.

Figure 17 presents the results of one neutron flux determination. The data above 80-keV neutron energy were obtained from the methane gas counter, and the data below 80 keV were obtained from a relative measurement (using ^{3}He gas counters, as described in Section 3.5) and normalized to the proton-recoil data above 80 keV.

3.4 $^{10}BF_3$ GAS PROPORTIONAL COUNTERS

The $^{10}B(n,\alpha)^7Li$ reaction was used to measure the relative shape of the neutron flux energy spectrum at the 220-meter facility for neutron energies below 80 keV. In addition, we obtained some information on the $^{10}B(n,\alpha)^7Li$ cross section relative to the n-p scattering cross section for neutron energies above 80 keV. The measurements were made with two gas proportional counters containing one atmosphere of boron-tri-fluoride gas enriched in ^{10}B (96%). The dimensions of the counters are identical to those of the methane gas counter (Table 1). The counters were located with their long dimension parallel to the neutron beam at positions A and C shown in Fig. 9.

A third counter was located outside the 8-in. (20.32-cm) o.d. aluminum drift tube, but at the same flight-path distance as the two counters in the neutron beam. The entire configuration was covered with several layers of 0.020-in. (0.051-cm) -thick cadmium sheets to prevent detection of slow "room return" neutrons. The background count rate observed by the outer counters was equivalent to about 2-4% of the count rate observed by the counters in the neutron beam.

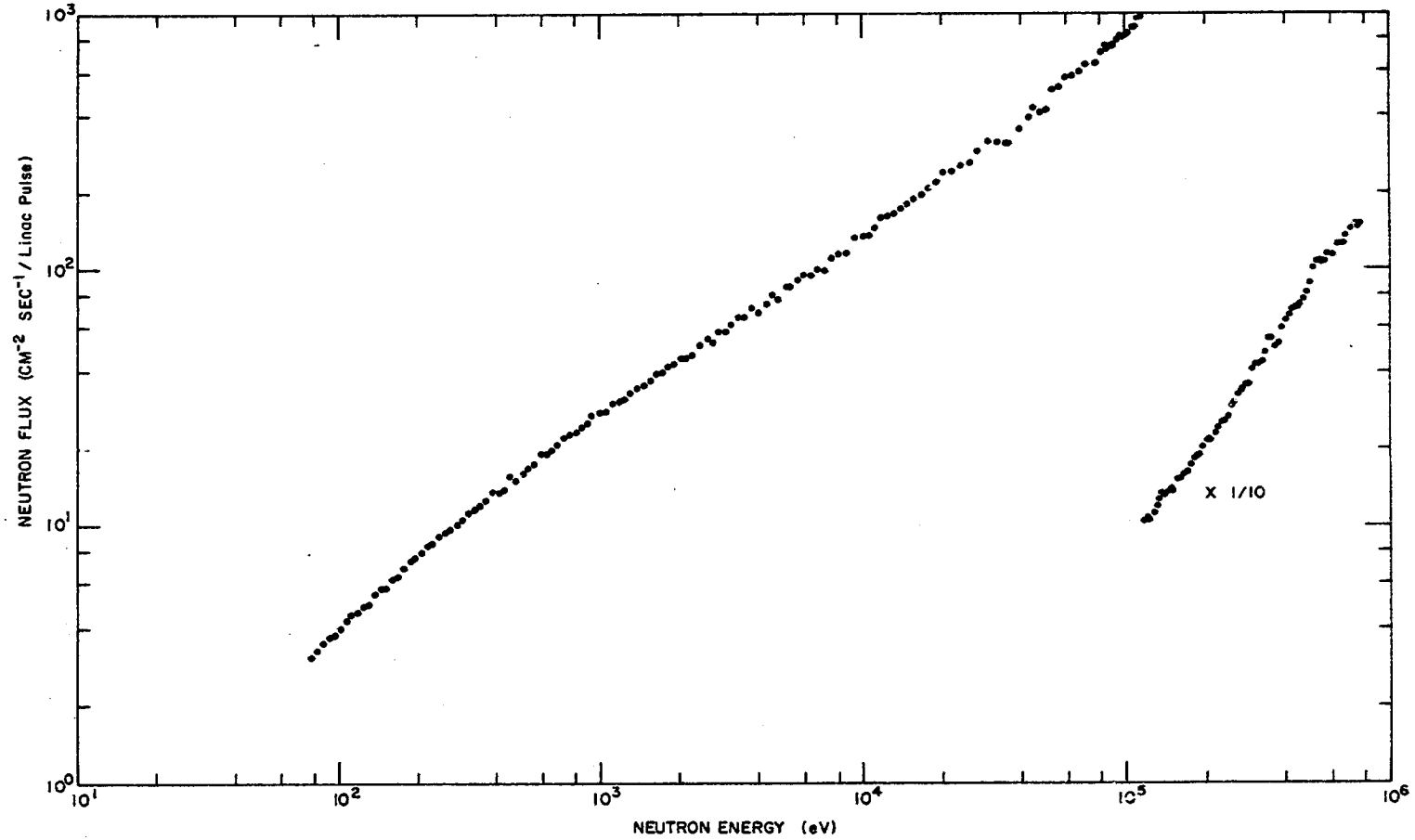

Figure 17. Neutron flux time-of-flight spectrum measured with ^{3}He ($E_n \leq 80$ keV) and CH_4 ($E_n > 80$ keV) gas proportional counters at a 227-meter flight-path distance, with a 0.4 μs LINAC burst width, a peak current of 350-mA, and an electron energy of 40 MeV.

The pulse spectrum obtained with these counters is shown in Fig. 18. Most of the alpha and ^{7}Li particles produced by the $^{10}B(n,\alpha)^{7}Li$ reaction deposit all their kinetic energy in the gas volume of the counter, which accounts for pulses in channels > 100 (see Fig. 18). When the reaction occurs near the wall of the counter, one of the two particles may be deposited in the wall material. If the alpha particle is lost in the wall, the minimum energy deposited in the gas volume is the kinetic energy ($\sim$836 keV) of the ^{7}Li ion, and this accounts for the "knee" of the pulse spectrum at channel 40 in Fig. 18. When the ^{7}Li particle goes into the wall, the energy of the alpha particle ($\sim$ 1.44 MeV) gives rise to the second "knee" observed around channel 70 of Fig. 18. Since the maximum energy given to ^{10}B nuclei in elastic neutron collisions is $\sim 1/3\ E_n$, an electronic threshold may be set in the valley of the pulse spectrum ($\sim$channel 30 in Fig. 18) without any danger of observing ^{10}B recoils and without any change in the detection efficiency of the (n,α) reaction for neutron energies of interest in this work.

Equation 1 in Section 3.3 also describes the count rate observed with the $^{10}BF_3$ gas counters, with the substitution $\sigma_{n,\alpha}$ for $\sigma_{n,n}$. As mentioned above, $\epsilon_b = 1.0$ and is independent of neutron energy. The contribution from multiple scattering events can be shown to be less than 0.1%. Consequently, the factor $1-\delta(E_n)$ in Eq. 1 is taken to be equal to the self-shielding factor,

$$1 - \delta(E_n) \simeq 1 - \tfrac{1}{2}\langle \Sigma_T(E_n)\rangle L , \qquad (29)$$

where Σ_T is the macroscopic total cross section of the $^{10}BF_3$ gas, L is the active length of the counter, and the brackets around Σ_T indicate an average over an energy interval representative of the instrumental resolution of the measurement. The quantity δ was found to be about 0.155 at 10 eV and less than 0.05 at neutron energies greater than 130 eV (even in

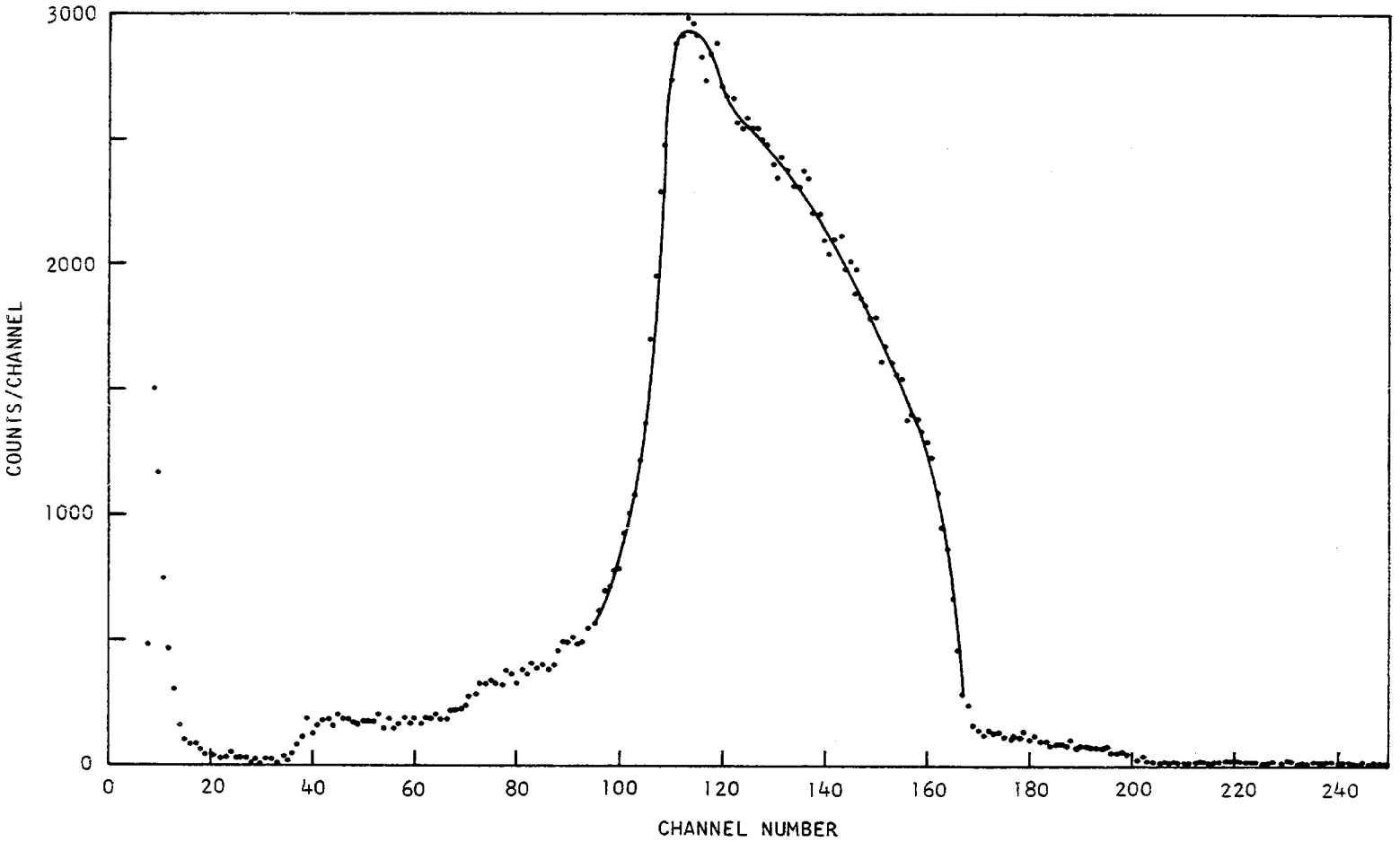

Figure 18. Pulse-height distribution obtained with a $^{10}BF_3$ gas proportional counter (5.08-cm diameter, 60.96-cm active length, and 1-atm of gas pressure) using a thermalized 1-curie Pu-Be neutron source.

the regions of the fluorine resonances near 27 keV, 50 keV, and 100 keV). A plot of $(1-\delta)^{-1}$ vs E_n is shown in Fig. 15. The transmission $T(E_n)$ of the aluminum-oxide end window was treated by the procedure described in Section 3.3.6 using a Gaussian resolution function (Eq. 25) calculated with the appropriate time jitter (5.5 μs) for these counters.

The manufacturer of the $^{10}BF_3$ gas counters was unable to furnish precise temperature and pressure data from which we could obtain an accurate value of the gas density. It was therefore necessary to obtain the thickness of the counter (N in Eq. 1) by the following procedure. Neglecting multiple scattering and background events in the counters, the count rate expression (Eq. 1) can be written as

$$\frac{dC}{dt}(E_n) = \epsilon_b S T(E_n) \frac{d\varphi}{dt}(E_n)\left[1 - \exp(-N\sigma_T(E_n))\right] \frac{\sigma_{n,\alpha}(E_n)}{\sigma_T(E_n)} . \quad (30)$$

At low neutron energies, say $E_n < 0.1$ eV, the counter gas volume absorbs essentially all incident neutrons, and the above expression approaches a limiting value which is independent of N:

$$\frac{dC}{dt}(E_n) = Q \frac{d\varphi}{dt}(E_n) , \quad (31)$$

where Q is approximately constant with energy and equal to $\epsilon_b ST(E_n)$ since $\sigma_{n,\alpha} \approx \sigma_T$. Consequently, if one knows the relative energy dependence of the neutron flux $\frac{d\tilde{\varphi}}{dt}(E_n)$ and the ^{10}B cross sections, the counter thickness N can be obtained from the measured count rate $\frac{dC}{dt}(E_n)$ using Eqs. 30 and 31:

$$N\sigma_T(E_n) = -\ell n\left[1 - \frac{\frac{dC}{dt}(E_n)\sigma_T(E_n)}{k\frac{d\tilde{\varphi}}{dt}(E_n)\sigma_{n,\alpha}(E_n)}\right] , \quad (32)$$

where k is a normalization constant deduced at low energy with a precision of about 1% ,

$$k \equiv \frac{Q\,\frac{d\varphi}{dt}(E_n)}{\frac{d\tilde{\varphi}}{dt}(E_n)} = \left.\frac{\frac{dC}{dt}}{\frac{d\tilde{\varphi}}{dt}}\right|_{E_n < 0.1\ eV} . \qquad (33)$$

For the thickness determination, the relative neutron flux shape $\frac{d\tilde{\varphi}}{dt}(E_n)$ was obtained from a capture measurement in the neutron energy region 0.01 eV to 10 eV with the Gulf General Atomic 20-meter experimental facility[17] using a 5.08-cm diameter gold foil with a thickness of 1.529×10^{-3} nuclei/barn. This determined the flux shape in the region $0.01\ eV \leq E_n \leq 10\ eV$ from the relation

$$\frac{d\tilde{\varphi}}{dt}(E_n) = \frac{\frac{dC_\gamma}{dt}(E_n)}{P_{n,\gamma}(E_n)} , \qquad (34)$$

where dC_γ/dt is the observed capture count rate (corrected for backgrounds) and $P_{n,\gamma}$ is the capture probability which can be calculated with the computer code TACASI[18] from the well-known gold cross section and resonance parameters in this energy region. The precision of the relative flux $d\tilde{\varphi}/dt$ achieved by this procedure is estimated to be about 1%.[19] Since the total cross section of ^{10}B is also known to a precision of 1% in the energy region 0.01 to 10 eV, the thickness of the counters was found (with Eq. 32) to be $(1.40 \pm 0.04) \times 10^{-3}$ nuclei/barn.

When the quantities ϵ_b, S, N, $\langle T(E_n)\rangle$, $\frac{dB}{dt}(E_n)$ and $\left[1-\delta(E_n)\right]$ in Eq. 1 have been determined, the neutron flux $\frac{d\varphi}{dt}(E_n)$ can then be found from the measured count rate $\frac{dC}{dt}$ and the known cross section $\sigma_{n,\alpha}(E_n)$, or, conversely, one can obtain the cross

section $\sigma_{n,\alpha}(E_n)$ with a neutron flux measured by some other method. Since the neutron flux can be obtained more precisely from the proton-recoil gas counter for $E_n \geq 80$ keV (see Section 3.3), the $^{10}BF_3$ counter measurements were used for neutron flux determinations only below 80 keV.

In the energy region 80 keV - 700 keV, an effort was made to obtain the (n,α) cross section relative to the n-p scattering cross section, using the $^{10}BF_3$ and methane data such as shown in Figs. 19 and 13 and the relation (from Eq. 1)

$$\sigma_{n,\alpha}(E_n) = \left\{ \frac{\left[\frac{dC}{dt}(E_n) - \frac{dB}{dt}(E_n)\right]}{\langle T(E_n)\rangle \epsilon_b S N [1-\delta(E_n)]} \right\}_{^{10}BF_3} \left\{ \frac{\langle T(E_n)\rangle \epsilon_b(E_n) S N_H \sigma_{n,n}(E_n)[1-\delta(E_n)]}{\left[\frac{dC}{dt}(E_n) - \frac{dB}{dt}(E_n)\right]} \right\}_{CH_4} . \tag{35}$$

In this expression, the net count rates from the $^{10}BF_3$ and CH_4 counters were obtained in separate measurements, hence the count rates were normalized to the same neutron beam intensity and duration. The neutron beam was monitored during both measurements with the set of ^3He counters described in the next section. An uncertainty of 2% is assigned to the normalization procedure.

The (n,α) cross section obtained by the above procedure was averaged over 20% energy intervals in order to reduce statistical fluctuations and is shown in Fig. 20. The rectangles in the figure indicate the energy resolution of the measurement, which is dominated by the large time jitter (5.5 μs) of the $^{10}BF_3$ counters. From this figure, we see that our results agree with a (1/v) cross section extrapolated from the thermal value[14] to about 200 keV, and that our cross section is lower than the (1/v) extrapolation at higher energies. However, for $E_n > 200$ keV, the $^{10}BF_3$ counter's time jitter degrades the energy resolution to $\Delta E_n/E_n > 0.3$, so that the data at higher energies indicate only the overall trend of the (n,α) cross section.

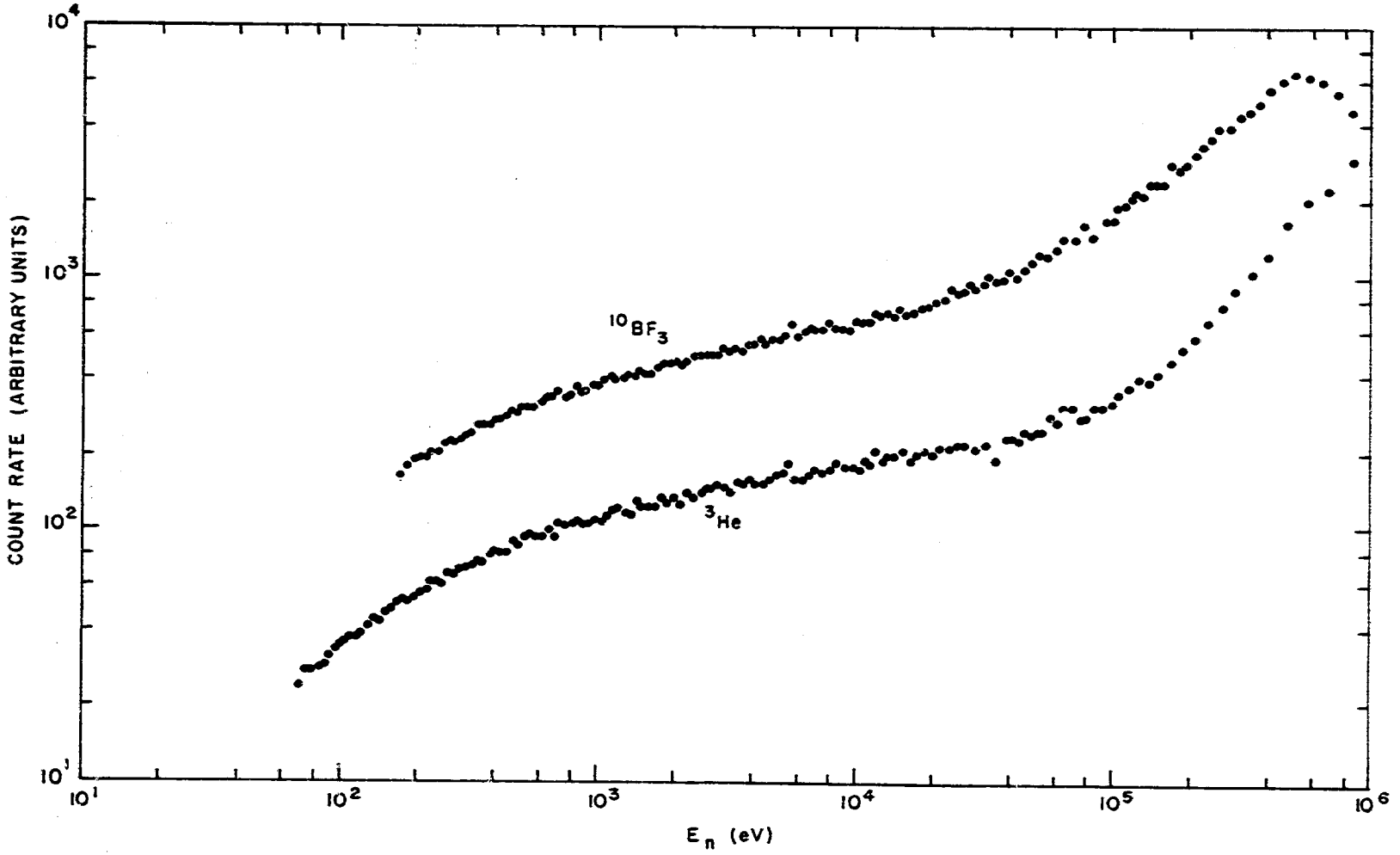

Figure 19. Time-of-flight data obtained at the 220-meter facility with $^{10}BF_3$ and ^3He gas counters. The data have been corrected for backgrounds, self-shielding effects, end-window transmission, and electronic threshold efficiency. (The normalization of these data was adjusted arbitrarily.)

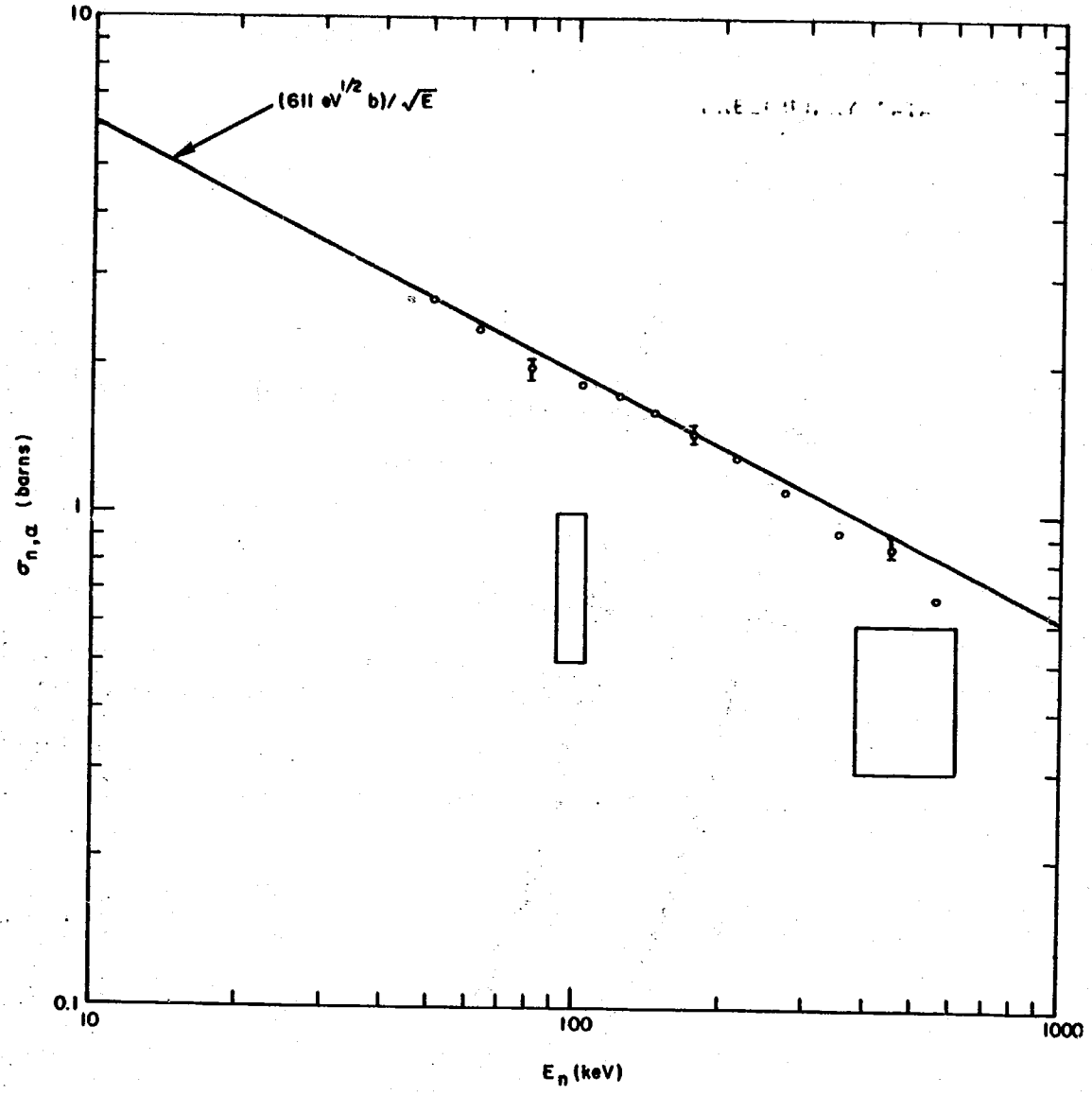

Figure 20. The $^{10}B(n,\alpha)^{7}Li$ cross section obtained from $^{10}BF_3$ and CH_4 gas counter time-of-flight measurements at the 220-meter facility. The uncertainty in the cross section is about 7%. The rectangles indicate an energy interval equivalent to the rectangular time-jitter distribution (5.5 μs) of the $^{10}BF_3$ counters.

3.5 ^{3}He GAS PROPORTIONAL COUNTERS

Neutron detection with the ^{3}He(n, p)T reaction was implemented with four 1-in. (2.54-cm) diameter cylindrical gas proportional counters containing ^{3}He as the major part (97%) of the filling gas. The active length of the counters is 6 inches (15.24 cm) and the gas pressure is 10 atmospheres. For the flux measurements at the 220-meter facility concurrent with the capture cross-section measurements, two counters are located across the outer edges of the 6-in. (15.24-cm) diameter neutron beam (see Figs. 5, 6, and 9). The capture measurements utilize the inner 4-in. (10.16-cm) diameter portion of the neutron beam which is not intercepted by the ^{3}He counters.

To calibrate the response of the ^{3}He counters against the ^{10}B(n, α)^{7}Li cross section and the n-p scattering cross section, auxiliary measurements were made in which the ^{3}He detection system was used concurrently with either a $^{10}BF_3$ counter or a methane counter. For these measurements, the ^{3}He counters are positioned in the beam as shown in inset c of Fig. 9, and the $^{10}BF_3$ or methane counter views the central 2-in. (5.08-cm) portion of the beam.

The count rate $\frac{dC}{dt}(E_n)$ observed from the ^{3}He counters can be expressed as

$$\frac{dC}{dt}(E_n) = K\,\epsilon_b(E_n)\sigma_{n,p}(E_n)\left[1-\delta(E_n)\right]\frac{d\varphi}{dt}(E_n) + \frac{dB}{dt}(E_n)\,, \qquad (36)$$

where K is a constant, ϵ_b the efficiency, δ the multiple scattering and self-shielding correction, $\frac{d\varphi}{dt}$ the incident neutron flux, $\frac{dB}{dt}$ the background count rate, and $\sigma_{n,p}$ the cross section for the ^{3}He(n, p)T reaction.

The background count rate $\frac{dB}{dt}(E_n)$ is primarily due to neutrons scattered into the room by collimators, mylar windows, and detectors which intercept the neutron beam. This background is directly measured by two ^{3}He counters located just outside the neutron beam but near the two counters which intercept the beam, as shown in Fig. 9. Since the

entire ^{3}He detector configuration is far ($\sim$2 meters) from the floor and walls of the room, the counters should all see the same room-return background environment. The background measured by the "outside" counters is typically 2-4% of the count rate observed by the "inside" counters.

The contribution to $\delta(E_n)$ in Eq. 36 from multiple scattering events can be estimated from the first two terms in the collision expansion (see Eq. 18) of the (n, p) reaction probability. We obtain

$$\delta(E_n) \simeq \frac{P_2}{P_1}(E_n) \simeq \frac{\Sigma_s(E_n)}{\Sigma_{n,p}(E_n)} \cdot \Sigma_{n,p}(E')\bar{r} \quad , \tag{37}$$

where Σ_s is the macroscopic scattering cross section for ^{3}He, $\Sigma_{n,p}$ is the macroscopic cross section for the ^{3}He(n, p)T reaction, E' is the energy of the scattered neutron and $\bar{r}$ is the average path length of the scattered neutron through the ^{3}He gas volume. Assuming the maximum energy loss per collision ($E' = E_n/4$) and a (1/v) dependence of $\Sigma_{n,p}$, we have

$$\frac{P_2}{P_1}(E_n) < 2\,\Sigma_s(E_n)\bar{r} \quad . \tag{38}$$

The average path length $\bar{r}$ was calculated with the simplifying assumption of isotropic scattering in the laboratory system and found to be about 2 cm. With this value in the above equation we obtain $P_2/P_1 < 0.002$, a result which is essentially independent of neutron energy since Σ_s is constant for energies less than 1 MeV. Consequently, multiple-scattering contributions can be ignored since they do not alter the shape of the neutron flux spectrum deduced from the data, and the factor $\left[1-\delta(E_n)\right]$ in Eq. 36 is then taken equal to the self-shielding factor given by Eq. 22. A plot of $(1-\delta)^{-1}$ vs E_n is shown in Fig. 15.

In the ^{3}He(n, p)T reaction the triton and proton have a total energy of Q = 764 keV plus the energy of the incident neutron. A pulse is formed in the proportional counter with a magnitude that is directly proportional to the total amount of energy given up by the two particles as they pass through the gas. Figure 21 shows a typical pulse-height distribution obtained with the 1-in. (2.54-cm) diameter counter in an isotropic flux of thermal neutrons. The plateau region (B in Fig. 21) of the pulse-height distribution is formed by particles that do not lose all their energy in the sensitive volume of the counter. The "knee" in the distribution (C in Fig. 21) results from events that occur near the surface of the wall (cathode), where the proton goes into the wall and the triton, which carried off (1/4) Q in kinetic energy, goes into the gas volume.

When the ^{3}He counter is irradiated with fast neutrons having kinetic energy E_n, the peak of the pulse-height distribution from ^{3}He(n, p)T reactions (A in Fig. 21) will be located at a point corresponding to the energy $Q + E_n$. Pulses will also result from neutron elastic scattering events with ^{3}He nuclei, and these must be rejected so that the observed count rate does not depend on the ^{3}He scattering cross section. Consequently, if time-of-flight measurements are to be made using one pulse-height threshold for neutron energies from 1 to 400 keV, the threshold must be set to at least 300 keV, i.e. the energy of the most energetic ^{3}He recoil. However, setting the threshold at some point above the minimum pulses from the (n, p) reaction (C in Fig. 8) results in a detection efficiency $\epsilon_b(E_n)$ which varies with neutron energy, since the peak of the pulse spectrum (A of Fig. 21) shifts with the neutron energy. Moreover, the angular distributions of the reaction products (triton and proton) are isotropic in the laboratory system only when induced by thermal neutrons and are shifted towards the forward direction when induced by fast neutrons. This effect results in a change in the fraction of particles that are lost in the walls of the counter and, hence, changes the number of pulses in the plateau region (B in Fig. 21) relative to the total number of pulses.

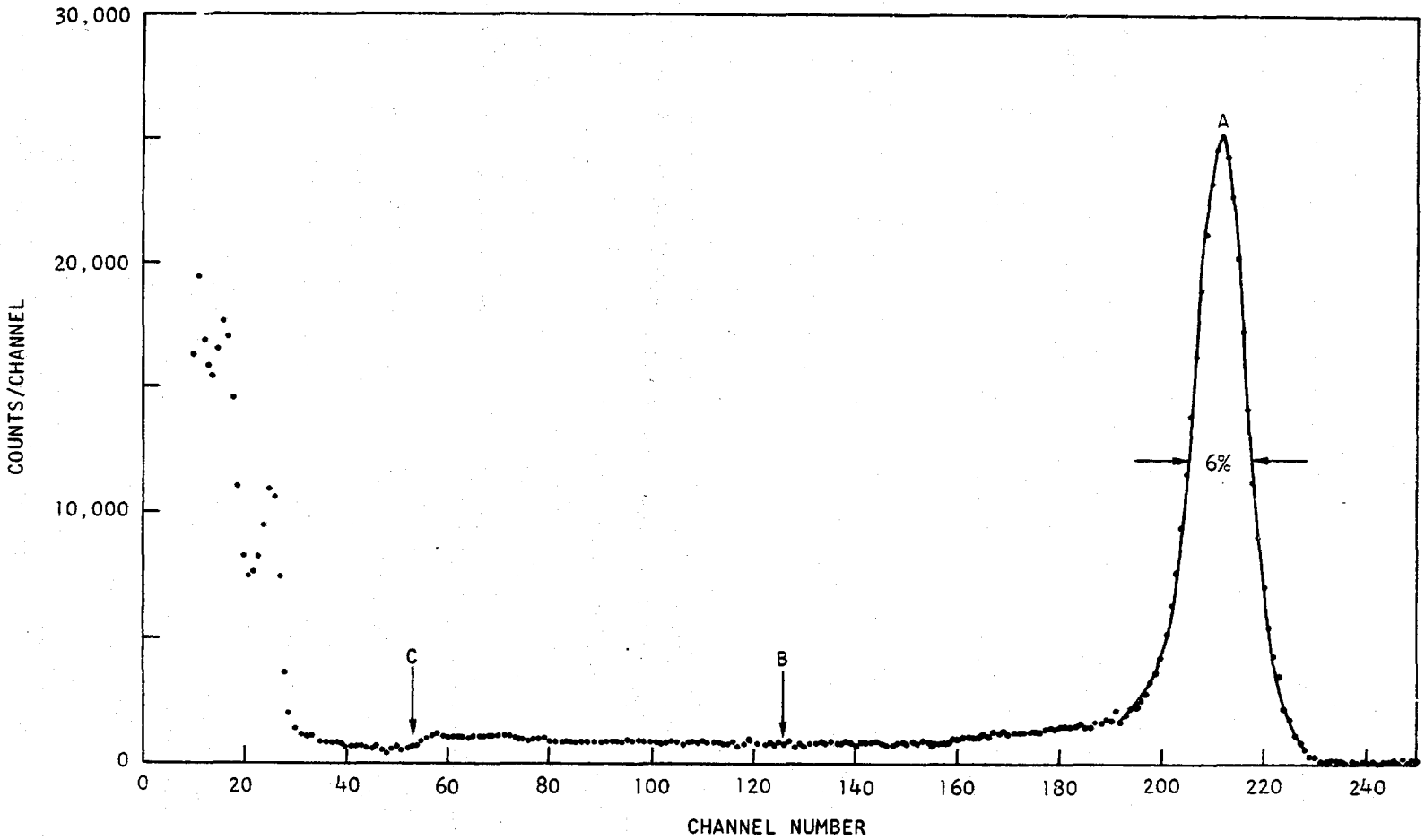

Figure 21. Pulse-height spectrum obtained with two ^{3}He gas proportional counters (2.54-cm diameter, 15.24-cm active length, and 10-atm pressure) using thermalized neutrons from a 1-curie Pu-Be neutron source. The ^{3}He counters are those shown in Figs. 5 and 6.

Thus, a calculation of $\epsilon_b(E_n)$ is not straightforward and the efficiency was determined experimentally from pulse-height spectra obtained with the two-parameter data acquisition mode discussed in Section 3.3.1. Time-of-flight and pulse-height data were recorded by the CDC-1700 computer, and the record was searched by the computer for events corresponding to various small ranges of incident neutron energies. This procedure yielded pulse-height spectra from which the efficiency for a given threshold could be calculated for various neutron energies.

Figure 22 shows three such pulse-height spectra. The efficiency is given by the ratio of the number of counts in the channels above the threshold channel to the total number of counts originating from the ^{3}He(n, p)T reaction. For the lower energies the "knee" in the spectra is easily recognized, and the total number of proton and triton counts can be found from the total counts above the knee. At higher energies ^{3}He recoils obscure details of the lower end of the (n, p) pulse-height spectrum, and it was necessary to extrapolate the spectrum to obtain the total counts. The spectrum was assumed to fall linearly to zero in the region of the ^{3}He recoils. The uncertainty this introduces in the total counts is taken to be the full extrapolated contribution, and this amounts to less than 3.5% for energies less than 400 keV. At the lower energies the uncertainty in ϵ_b is largely statistical and is approximately 1.5%.

Figure 23 shows the values of ϵ_b measured at various neutron energies with a pulse-height threshold fixed at 80% of the peak in the spectrum produced by thermal neutrons. Batchelor, et al.[20] have calculated wall effects in ^{3}He proportional counters for 0, 1/3, 2/3, and 1 MeV incident neutron energies. The values of ϵ_b based on these calculations are also plotted in Fig. 23 and are in good agreement with the measured values.

Possible effects of gain shifts in the ^{3}He detection system induced by bremsstrahlung rays from the neutron source were investigated in the following way. The observed peak position of the pulse-height spectrum

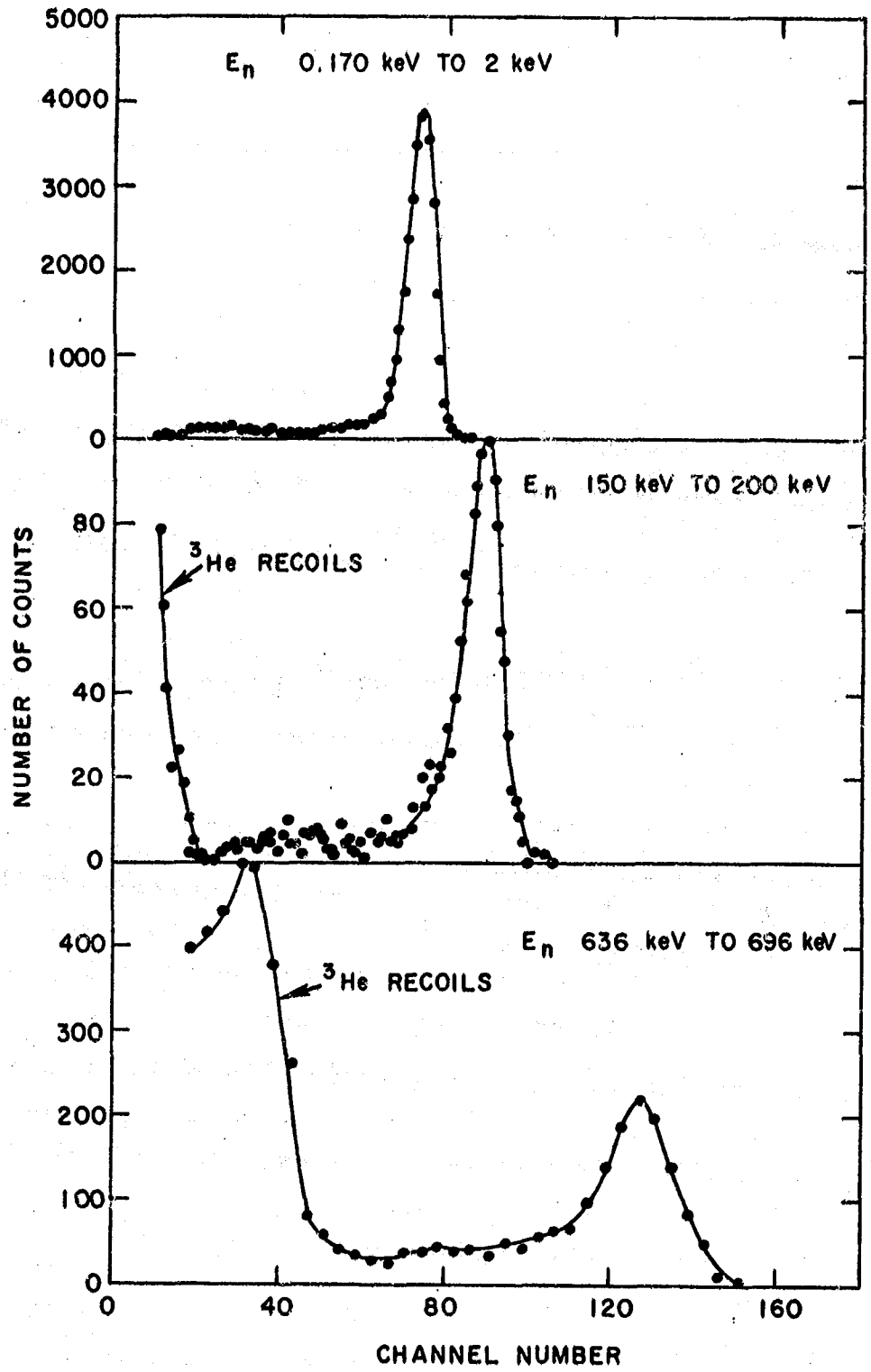

Figure 22. Three pulse-height spectra obtained with ^{3}He gas proportional counters, the 220-meter flight path facility, and a two-parameter mode of data acquisition. The data shown are not corrected for background effects.

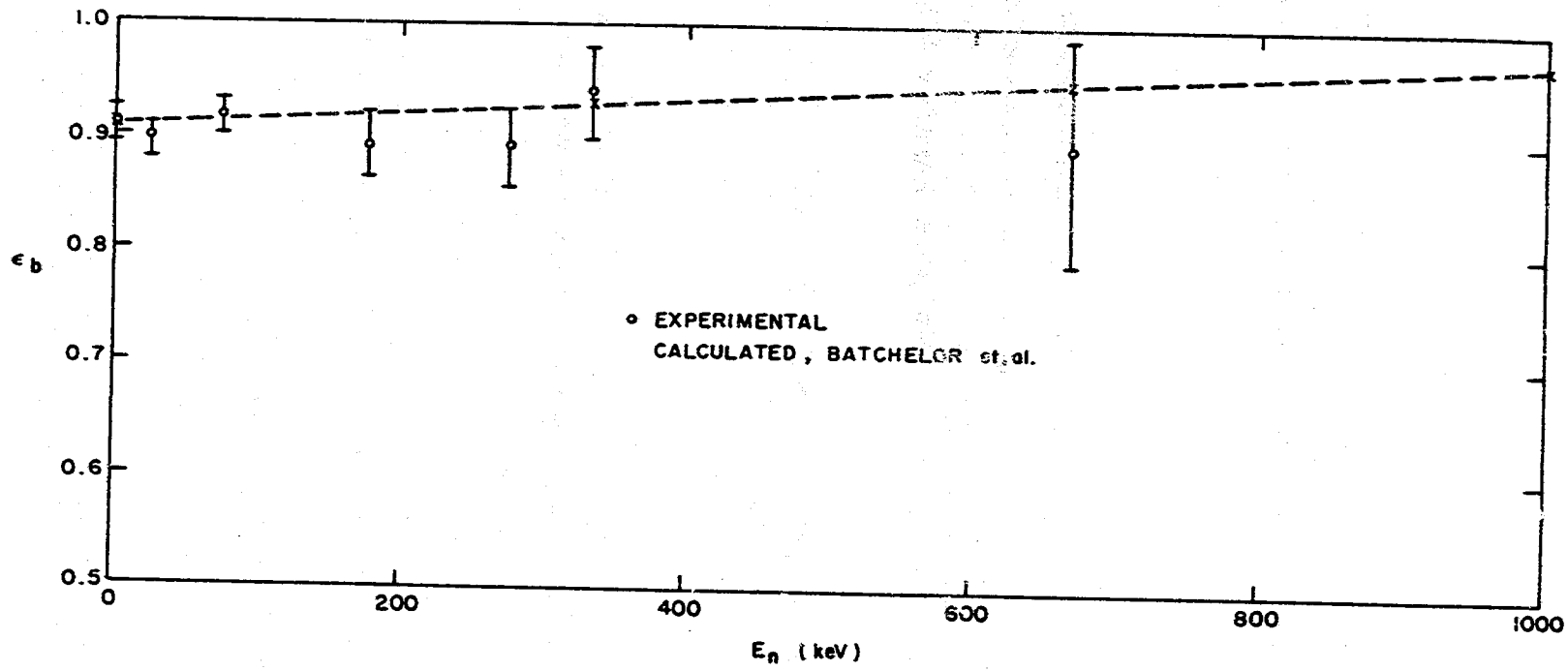

Figure 23. The spectrum fraction vs E_n for ^3He counters which results from a fixed electronic threshold set to 80% of the thermal neutron peak location. The experimental points (open circles) were obtained from pulse-height spectra such as shown in Fig. 22. The calculated points (x) were obtained with a formulation by Batchelor, et al. (20)

from the $^{3}He(n, p)T$ reaction was compared to the calculated peak position $\left[a(\overline{E}_n + Q) + b\right]$, where $\overline{E}_n$ is the average neutron energy for the pulse-height spectrum, Q is the energy released by the reaction, and a and b are constants obtained from a pulse-height spectrum measured with a moderated Pu-Be neutron source, i. e. under conditions where the bremsstrahlung pulse is absent. The observed and calculated peak positions agreed to better than 2% up to a neutron energy of 1 MeV but showed discrepancies thereafter. Thus, for the energies of interest in this work, we find no evidence of any significant nonlinearity in the ^{3}He detector response which could be attributed to bremsstrahlung effects or nonlinear gas multiplication.

The quantity $K\sigma_{n,p}(E_n)\frac{d\varphi}{dt}(E_n)$ obtained from a typical measurement with the ^{3}He counter system is plotted vs E_n in Fig. 19. The same quantity obtained with the $^{10}BF_3$ detection system is also shown in Fig. 19. The ratio $R(E_n)$ of these two quantities should be proportional to the ratio of the respective reaction cross sections, $\sigma_{n,p}/\sigma_{n,\alpha}$; a plot of $R(E_n)$ is shown in Fig. 24.

Based on previous direct and indirect measurements,[21-24] the $^{10}B(n,\alpha)^{7}Li$ cross section varies as (1/v) for neutron energies up to 100 keV, within an uncertainty of about 5%. Within this margin, the fractional deviation of $R(E_n)$ from a constant value then gives the fractional deviation of the $^{3}He(n, p)T$ cross section from a (1/v) behavior. Some recent data for the $^{10}B(n,\alpha)^{7}Li$ cross section are compared to the (1/v) extrapolated cross section in Fig. 25. Our own preliminary results, discussed in Section 3.4, also agree with the (1/v) extrapolation in the neutron energy range 50 keV to 200 keV.

The recommended $^{3}He(n, p)T$ cross section for the neutron energy range from thermal to 100 keV is based primarily on: (1) transmission measurements in the region $0.0003\ eV < E_n < 11\ eV$ by Als-Nielsen and Dietrich;[25] (2) indirect measurements of $\sigma_{n,p}$ in the region

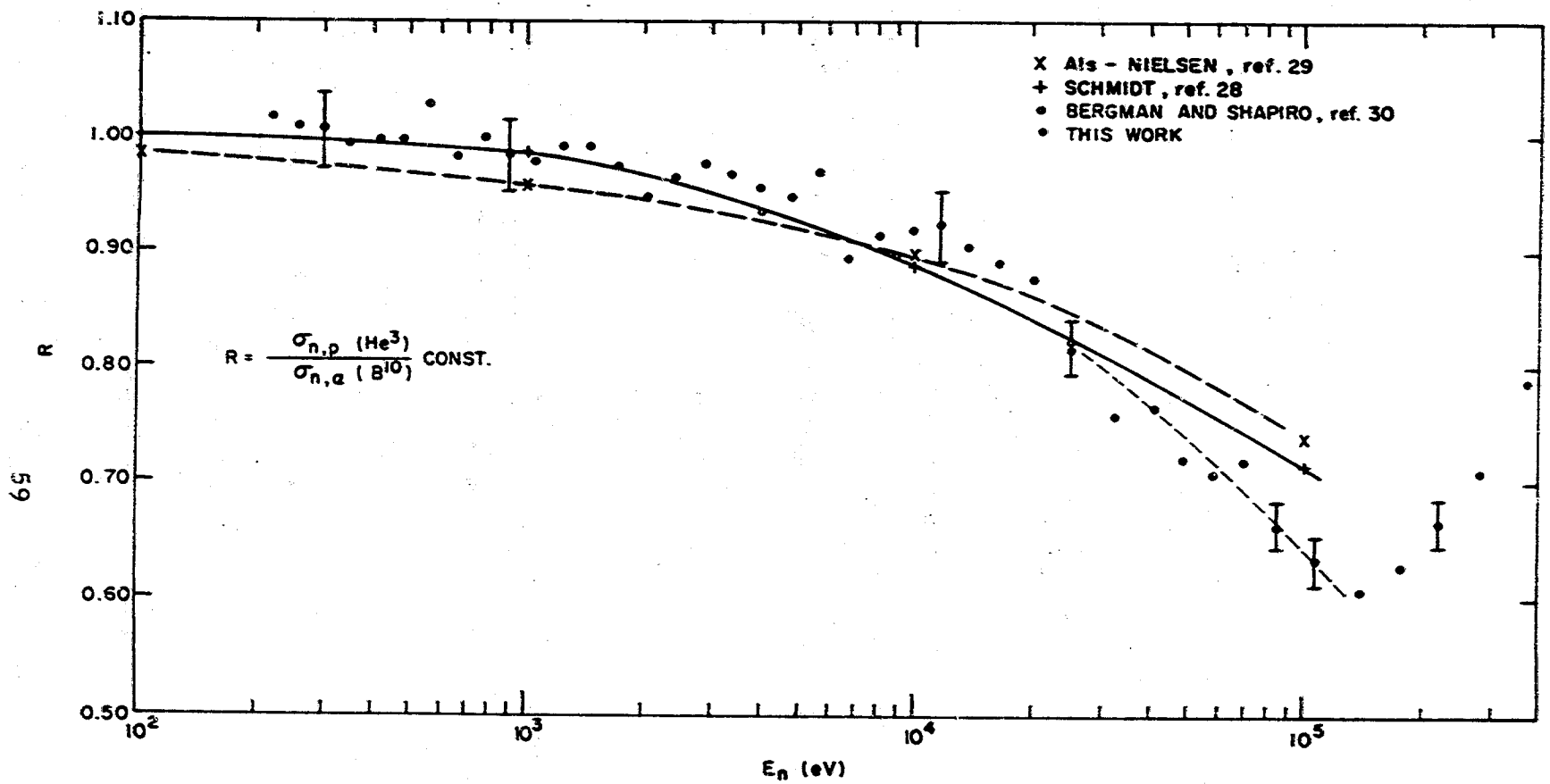

Figure 24. The ratio of ^{3}He counter data to $^{10}BF_3$ counter data (solid circles). The solid and dashed lines represent the deviation from a (1/v) behavior for the ^{3}He(n, p)T cross sections recommended by Als-Nielsen[29] and by Schmidt.[28]

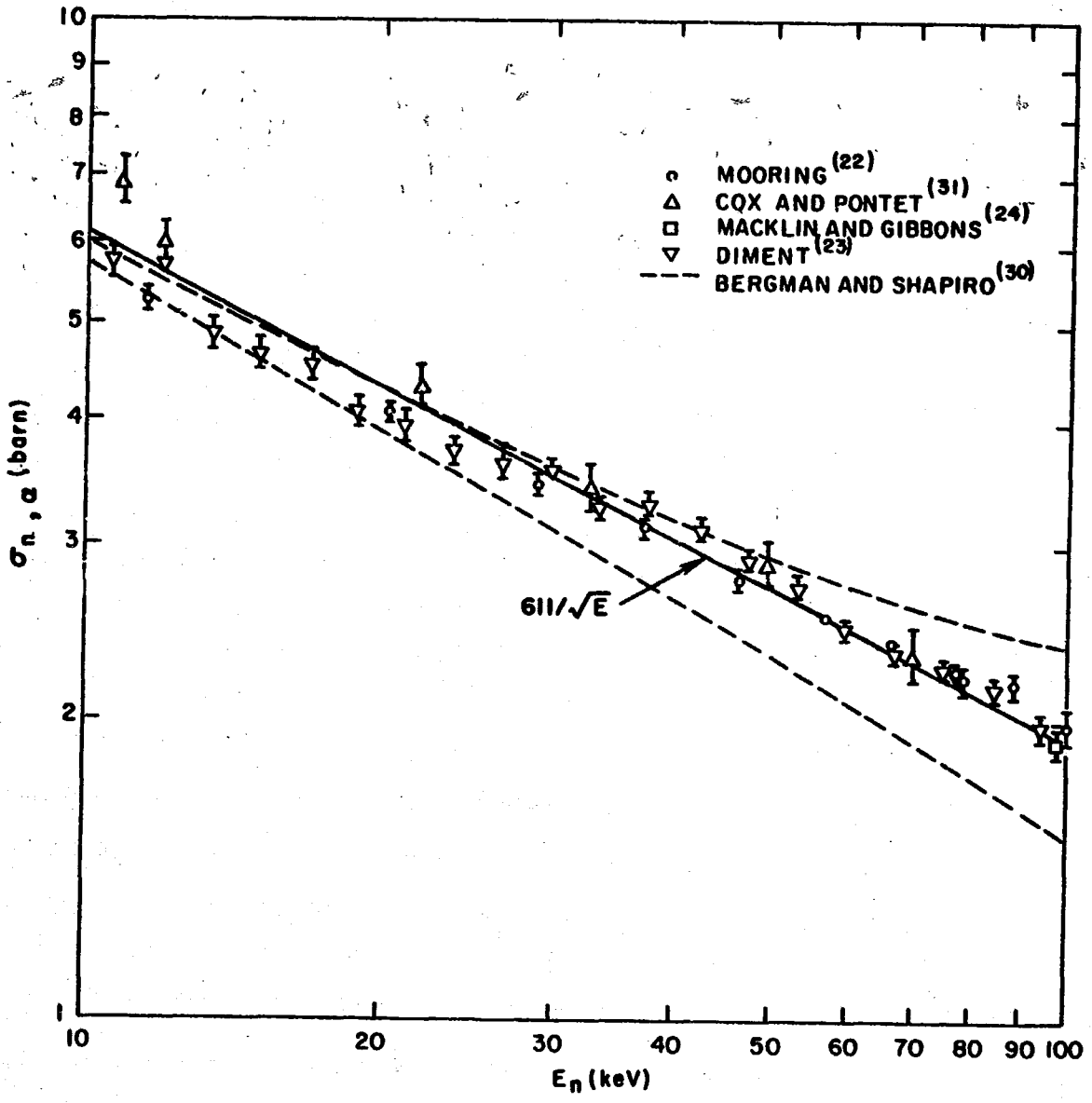

Figure 25. Recent $^{10}B(n,\alpha)$ cross section data between 10 and 100 keV. Dashed lines: lower and upper limit according to Bergman and Shapiro. (30)

5 keV < E_n < 300 keV by Macklin and Gibbons;[26] and (3) the theory of Shapiro,[27] which predicts the energy dependence of $\sigma_{n,p}$ and provides a means to extrapolate between 11 eV and 5 keV. The solid and dashed curves shown in Fig. 24 are obtained from

$$R(E_n) = \sigma_{n,p}(E_n)\, E_n^{\frac{1}{2}}\, (847\ eV^{\frac{1}{2}}\ b)^{-1} \quad , \tag{39}$$

with the recommended (n, p) cross sections by Schmidt[28] and by Als-Nielsen,[29] respectively. Also shown in Fig. 24 are ratios of $\sigma_{n,p}(^3He)/\sigma_{n,\alpha}(^{10}B)$ at 4, 9, and 25 keV which were deduced from the experimental ratios of $\sigma_{n,\alpha}(^6Li)/\sigma_{n,\alpha}(^{10}B)$ and $\sigma_{n,\alpha}(^6Li)/\sigma_{n,p}(^3He)$ reported by Bergman and Shapiro.[30] Within an uncertainty of about 5%, the experimental ratios obtained in this work and those deduced from Bergman and Shapiro's data[30] indicate that the $^3He(n,p)T$ cross sections recommended by Als-Nielsen[29] or by Schmidt[28] describe the true cross section for a neutron energy up to about 25 keV. Above 25 keV, our ratio indicates a larger deviation from (1/v) for $\sigma_{n,p}$ than the recommended cross sections based on Macklin and Gibbon's measurement[26] of the inverse reaction, $T(p,n)^3He$.

Since our data for the $^3He(n,p)T$ cross section depend on the $^{10}B(n,\alpha)^7Li$ cross section, and since the latter is not yet considered to be a precise standard at higher energies, one cannot easily resolve the discrepancy in $\sigma_{n,p}$ at 100 keV. However, since the uncertainty in the normalization of the $\sigma_{n,p}$ measurements by Macklin and Gibbons[26] is reported to be 10%, the discrepancy is really a disagreement in the slope of the $^3He(n,p)T$ cross section vs energy rather than in its absolute magnitude. Since we cannot, as yet, postulate any mechanism that would give rise to a systematic error in the slope of our data, we take the $^3He(n,p)T$ cross section to be that recommended by Schmidt[28] for $E_n \leq 25$ keV, and at higher energies to be that given by the smooth dotted line drawn through our data in Fig. 24, with an over-all uncertainty of 5%.

With this $^{3}He(n, p)T$ cross section, the relative neutron flux is obtained below 100 keV from the ^{3}He counter data by using Eq. 36. For neutron energies above 80 keV, the methane counter measurement of neutron flux is capable of higher precision and better neutron energy resolution. Consequently, for $E_n > 80$ keV the relative neutron flux is obtained with

$$\frac{d\tilde{\varphi}}{dt}(E_n)_A = \left[\frac{d\varphi}{dt}(E_n)_B\right]_{CH_4} \left[\frac{\frac{dC}{dt}(E_n)_A}{\frac{dC}{dt}(E_n)_B}\right]_{^3He} , \qquad (40)$$

where A labels the data corresponding to the capture measurement and B labels the auxiliary measurement with the methane gas counter. The two sets of relative neutron flux data obtained with Eqs. 36 and 40 are then joined together in the overlapping region 80-100 keV so as to give one continuous relative neutron flux shape from 70 eV to about 700 keV. For the analysis of capture cross sections, this relative neutron flux is normalized with the procedure described in Section 4. 2.

4. NEUTRON CAPTURE CROSS SECTIONS FOR TUNGSTEN AND RHENIUM

4.1 CAPTURE DATA

Time-of-flight (n, γ) measurements were made with natural metal samples of W and Re using the pulsed neutron source and 220-meter evacuated flight path described in Sections 2.1 and 2.2. The thickness of the W sample was 8.055×10^{-3} nuclei/barn (approximately 0.127 cm), and the thickness of the Re sample was 4.25×10^{-3} nuclei/barn (approximately 0.0635 cm); both samples were disks 12 cm in diameter. Additional capture data used to normalize these measurements (Section 4.2) were taken with the same samples at the 20-meter facility, which has been described previously[17] in detail. At the 220-meter station, capture gamma rays are detected with a 600-liter (0.6 m^3) liquid scintillator (shown in Figs. 5 and 6) which is similar, except for size, to the larger (4000-liter or 4 m^3) liquid scintillator located at the 20-meter station.

While the efficiency of the large gamma-ray detector can be shown[17] to be relatively insensitive to the gamma-ray cascade mode, this is not necessarily true for the smaller 600-liter detector at the 220-meter station. However, this detector facility was primarily designed for measurements at neutron energies of 1 keV to 1 MeV. There, capture measurements for heavy elements usually represent an average over many levels of the compound nucleus, since the energy resolution is inadequate to resolve individual resonances. Consequently, only an average detection efficiency is involved in this type of measurement, and this average efficiency changes only slowly with neutron bombarding energy.

A block diagram of the instrumentation for the 600-liter detector is shown in Fig. 26. The discriminator threshold was set to reject scintillator pulses that correspond to deposited gamma-ray energies of less than 4 MeV. (This adjustment was made with the aid of the 4.44-MeV gamma ray emitted by a Pu-Be neutron source.) The time history of the (n, γ) events was stored in a multi-channel analyzer using constant time intervals of 2 μsec. The flight path and the LINAC burst width for these measurements were 232.78 meters and 2 μsec, respectively. Since the gamma-ray detector response time is small ($\sim$30 nsec), and since the neutron-source effects on the instrumental energy resolution are also small (see Section 2.1), the experimental conditions result in a triangular time response with a 2-μsec FWHM. The resulting fractional neutron energy resolution is, from Eq. 2,

$$\Delta E_n / E_n = (2.4 \cdot 10^{-4}\ \mathrm{eV}^{-\frac{1}{2}})\, E_n^{\frac{1}{2}} . \qquad (41)$$

The resolution is illustrated in Fig. 27.

Possible overloading effects of the LINAC bremsstrahlung pulse on the instrumentation were investigated by the following procedure. Two measurements of count rate versus flight time were made using a 0.25-in. (0.635-cm) thick carbon sample, with and without a ^{24}Na gamma-ray source placed near the sample but outside the neutron beam. The difference between these two measurements should be the constant count rate observed from the radioactive ^{24}Na source. Since the discriminator threshold was set at 4 MeV, which is near the total gamma-ray energy (4.1 MeV) from the ^{24}Na source, this test is very sensitive to any gain changes induced in the instrumentation by the bremsstrahlung pulse. The recovery of the system was found to be complete in about 10 μsec after the LINAC pulse, which is equivalent to a neutron energy of about 2.7 MeV.

Time-of-flight capture gamma-ray data for W and Re measured with the 220-meter facility are shown in Figs. 28 and 29. Also shown are the backgrounds that have been subtracted from the capture data. The

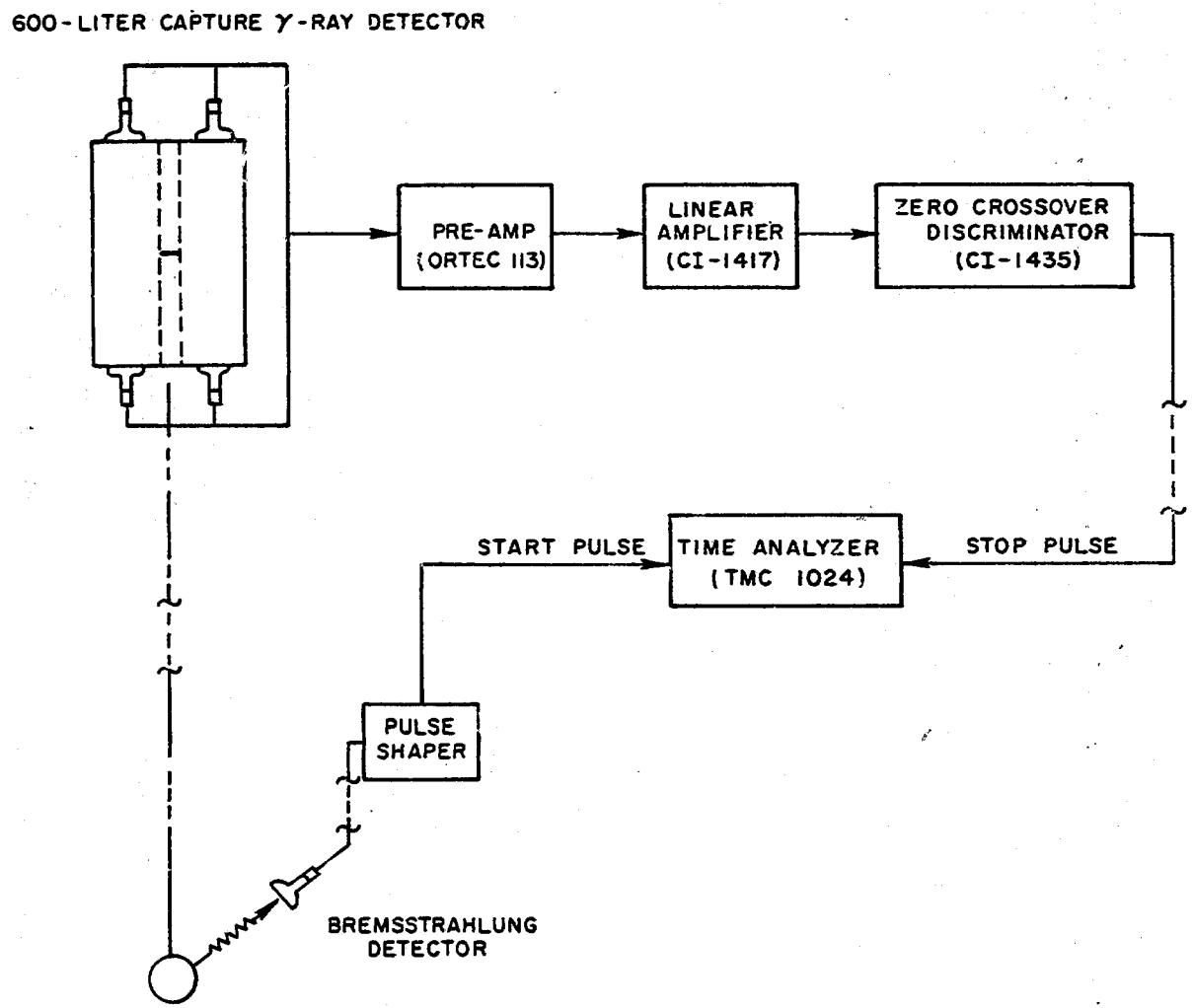

Figure 26. Schematic illustration of instrumentation for 600-liter scintillator.

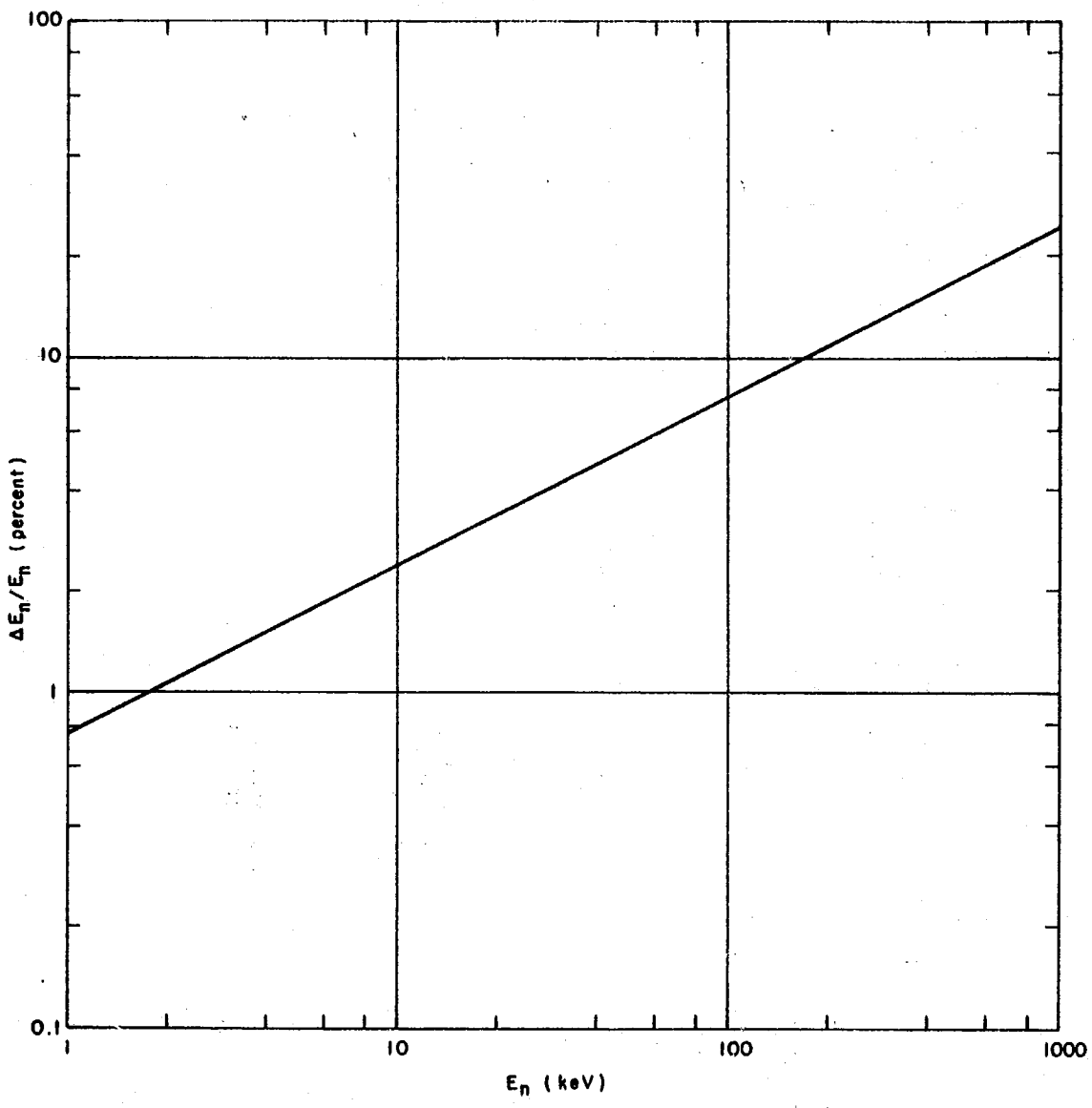

Figure 27. Over-all energy resolution of capture measurements at the 220-meter facility.

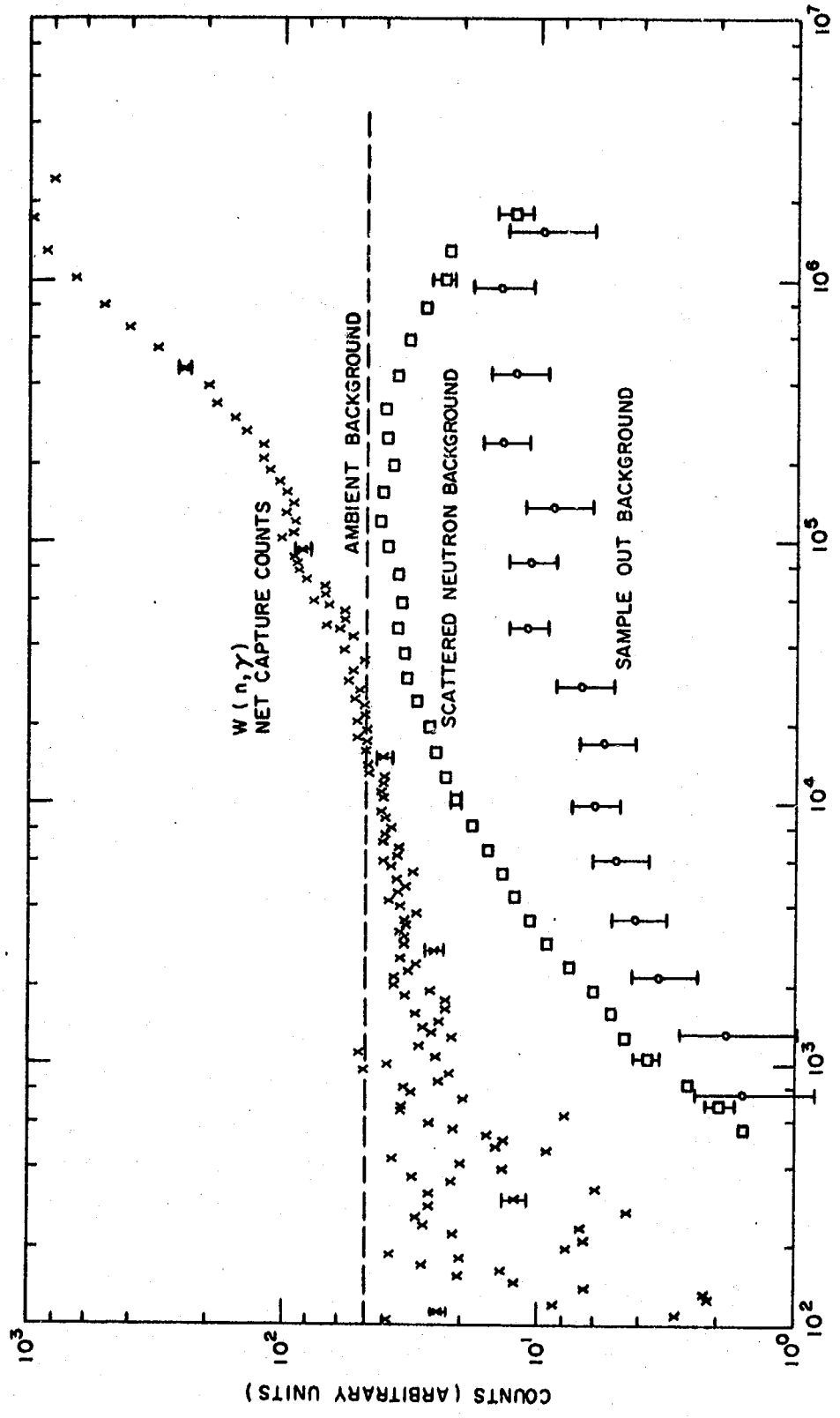

Figure 28. Time-of-flight neutron capture data for tungsten and associated gamma-ray backgrounds.

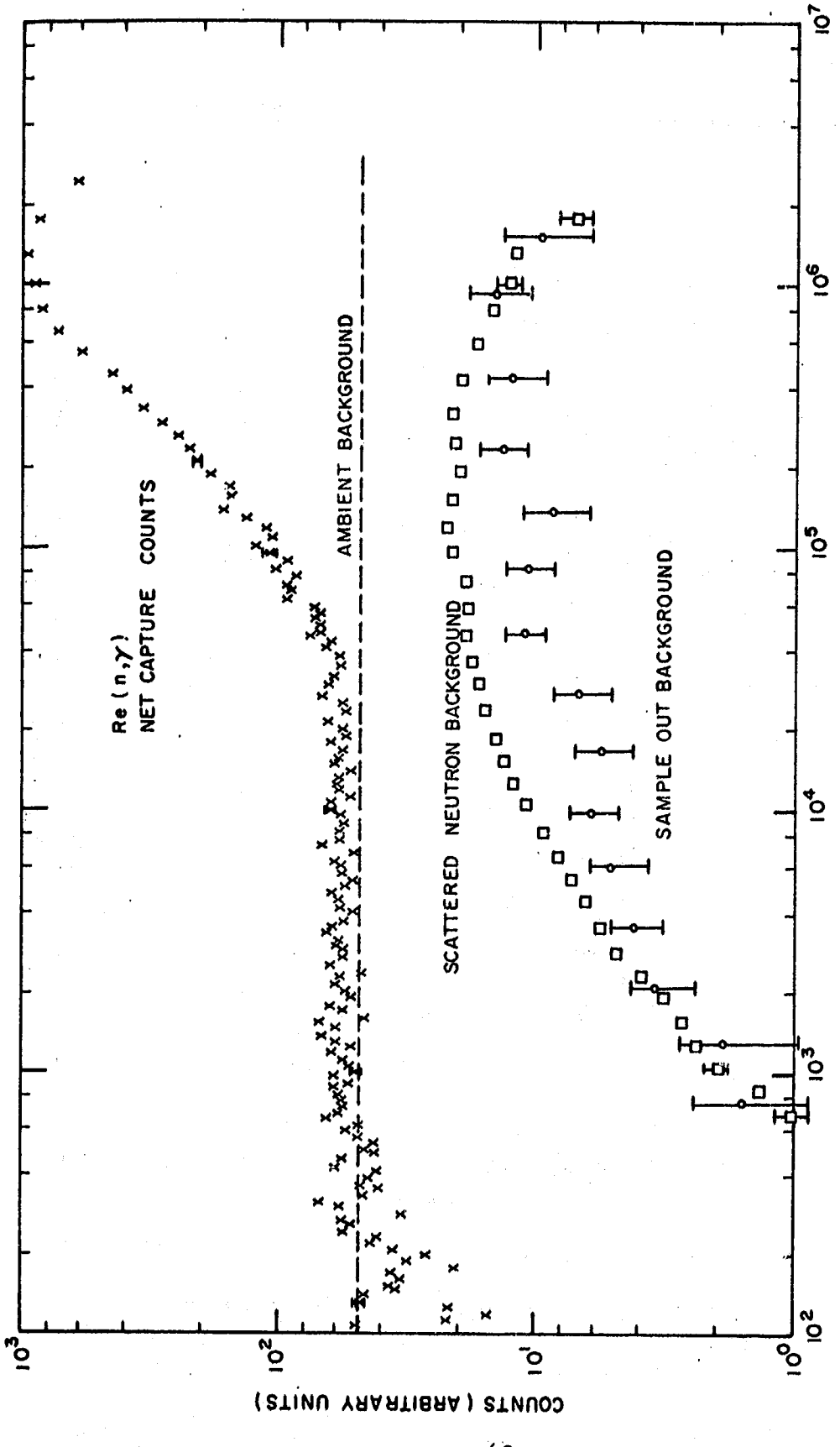

Figure 29. Time-of-flight neutron capture data for rhenium and associated gamma-ray backgrounds.

ambient background arises primarily from cosmic-ray interactions with the detector and from the natural radioactivity present in the detector and its environment. It is determined by a count-rate measurement with the linear accelerator turned off. The time-dependent LINAC-associated background is that background above ambient which is observed with the accelerator on and with no sample in the neutron beam. Its magnitude is proportional to the intensity of the neutron beam and is primarily due to neutrons scattered and captured in the vicinity of the collimator placed just in front of the detector.

The scattered neutron background is the result of neutrons that are scattered by the sample and are subsequently captured in the detector materials. A measure of this background was obtained by substituting a 0.25-in. carbon sample and scaling the observed gamma-ray counts by the ratio of the scattering probabilities for a representative neutron energy of 200 keV. For scattered neutrons from 100 to 700 keV energy, the ratios of the scattering probabilities of W and Re to that of C vary by amounts which produce a maximum change in the net capture counts of 7% for Re and 12% for W. The proper scattering ratio is not known exactly since the mean lifetime of neutrons scattered into the liquid scintillator is about 150 μsec. Consequently the time-dependent background from this source at any flight time is primarily due to neutrons scattered at earlier flight times. Furthermore, the capture sample is surrounded by a natural boron sleeve 0.6-in. thick by 20-in. long (see Fig. 5), which is progressively less transparent to lower energy neutrons having longer flight times. The over-all result is a scattered neutron background which varies slowly with flight time and which is proportional to an average scattering probability determined by the scattering properties of the sample in the upper keV neutron energy range.

To check the effectiveness of our procedures for background subtractions, we made an auxiliary capture measurement of tungsten in which we introduced a thick sodium "notch" filter in the neutron beam between the

first and second collimators (see Fig. 5). The count rate observed in the bottom of the transmission dip (due to the 2.85-keV resonance in ^{23}Na) agreed within 2% with the sum of the measured backgrounds at that neutron energy. We estimate a probable systematic uncertainty for the capture data of 5% due to background subtractions.

The sample-out and scattered-neutron backgrounds were smoothed prior to subtraction by grouping these data into intervals of $\Delta E_n = 0.2\ E_n$ and $0.5\ E_n$, respectively. The net capture counts at lower neutron energies (< 40 keV) were grouped into intervals of $\Delta E_n = 0.05\ E_n$, and at higher energies the interval is determined by the analyzer time channel width of 2 μsec. The total statistical uncertainty in the capture data (Figs. 28 and 29), including contributions from the statistical uncertainties of the backgrounds, attains a maximum near 50 keV of 8% for W and 10% for Re, and it diminishes to about 5% at the lowest and highest energies.

Capture cross sections were obtained from the observed gamma-ray counts by dividing by the incident neutron flux and by applying corrections for multiple scattering and resonance self shielding. The net capture counts $\left[\frac{dN}{dt}(E_n)\Delta t\right]$ observed in the time-of-flight interval Δt at the time corresponding to the energy E_n can be written

$$\frac{dN}{dt}(E_n)\Delta t = \epsilon(E_n) S\, T_\gamma \frac{d\varphi}{dt}(E_n)\Delta t \,\langle P_o(E_n) + P_s(E_n)\rangle , \qquad (42)$$

where $\epsilon(E_n)$ is the gamma-ray detection efficiency, S the sample area, T_γ a constant which accounts for the attenuation of capture gamma rays by the sample, $\frac{d\varphi}{dt}(E_n)$ the incident neutron flux per unit area per unit time of flight, and P_o and P_s are the first-collision and multiple-scattered capture probabilities, respectively. The brackets denote an average over an energy interval typical of the experimental resolution. Since multiply scattered neutrons differ little in energy from the incident neutrons (the average fractional energy loss per collision is $\Delta E/E = 2A/(A+1)^2$ or about one percent for A = 184), we have ignored any

difference in detection efficiency for capture events following one or more elastic collisions and express the average efficiency for a mixture of isotopes as

$$\epsilon(E_n) = \frac{\sum_i a_i \sigma_{\gamma i}(E_n)\epsilon_i(E_n)}{\sum_i a_i \sigma_{\gamma i}(E_n)} \quad , \tag{43}$$

where the i-th isotope has an abundance a_i and a capture cross section $\sigma_{\gamma i}$.

When many levels of the compound nucleus contribute to the measurement, the gamma-ray detection efficiencies ϵ_i for the different isotopes do not vary appreciably with the incident neutron energy until the energy becomes an appreciable fraction of the binding energy U_i less the scintillator threshold energy of 4 MeV, and we write

$$\epsilon(E_n) = \epsilon_o \alpha(E_n) \quad ,$$

$$\epsilon_o \equiv \frac{\sum_i a_i \bar{\sigma}_{\gamma i}\epsilon_i(o)}{\sum_i a_i \bar{\sigma}_{\gamma i}} \quad , \tag{44}$$

where $\bar{\sigma}_{\gamma i}$ are typical isotopic capture cross sections at low energies ($\sim$10 keV), and $\alpha(E_n)$ increases slowly from unity at high energies, say $E_n \gtrsim 100$ keV. (Differences in the ϵ_i for different isotopes were ignored in the correction for resonance self shielding.) The correction $\alpha(E_n)$ was then calculated using isotopic capture cross sections estimated with the code SESH (see below) from average statistical parameters, and using an estimate of the variation of the efficiency of the 600-liter scintillator with incident neutron energy. This efficiency estimate was made assuming the gamma-ray pulse-height distribution $f_i(E_\gamma, E_n)$ for each isotope (i) is stretched linearly with the total energy available for gamma

de-excitation, $f_i(E_\gamma, E_n) = f_i\left(\frac{U_i}{U_i + E_n} E_\gamma, 0\right)$, where U_i is the binding energy. The correction $\alpha(E_n)$ is then

$$\alpha(E_n) = \frac{\left[\Sigma_i a_i \sigma_{\gamma i}(E_n)\right]^{-1} \Sigma_i a_i \sigma_{\gamma i}(E_n) g_i(E_B, E_n)}{(\Sigma_i a_i \overline{\sigma_{\gamma i}})^{-1} \Sigma_i a_i \overline{\sigma_{\gamma i}}\, g_i(E_B, 0)} \quad , \tag{45}$$

where $g_i(E_B, E_n)$ is the gamma-ray pulse-height spectrum fraction above the scintillator discriminator level E_B,

$$g_i(E_B, E_n) = \frac{\int_{E_B}^{U_i+E_n} f_i(E_\gamma, E_n) dE_\gamma}{\int_0^{U_i+E_n} f_i(E_\gamma, E_n) dE_\gamma} \quad , \tag{46}$$

and the $\sigma_{\gamma i}$ are estimated isotopic capture cross sections. The correction $\alpha(E_n)$ is about 1.02 at 200 keV and increases to about 1.10 at 700 keV.

In the present measurements, the gamma-ray transmission through the sample (T_γ) does not vary appreciably with the energy of the incident neutrons, and T_γ is given by an isotopic average similar to that of Eq. 44. For example, for gammas of about 1 MeV energy, a change as large as 30% in the gamma energy would change the transmission of gammas passing through the full thickness of the W sample by less than 5%.[31]

4.2 NORMALIZATION

If we express the measured, un-normalized, incident flux spectrum as

$$\frac{d\tilde{\varphi}}{dt}(E_n) \equiv \frac{1}{C}\frac{d\varphi}{dt}(E_n) \ , \qquad (47)$$

where C is a normalization constant, then the capture probability is determined from the measured quantities according to

$$\langle P_o(E_n) + P_s(E_n)\rangle = \frac{\frac{dN}{dt}(E_n)}{\alpha(E_n)(\epsilon_o ST_\gamma C)\frac{d\tilde{\varphi}}{dt}(E_n)} \ . \qquad (48)$$

The normalization of the capture probability is thus determined by the product $(\epsilon_o ST_\gamma C)$, which can be found by the "saturated resonance" method. In this method, capture data are examined for a low-energy resonance for which the left-hand side of Eq. 48 approaches unity near the resonance energy and hence becomes insensitive to the neutron and radiation widths that characterize the resonance. At the expense of a somewhat greater reliance* on the resonance parameters, the full capture area A_{obs} of the resonance can be used in order to achieve a greater statistical precision; and resonances at energies E_n in different isotopes determine the quantities ($\alpha = 1$)

$$A_{obs} \equiv \Sigma_k \frac{dN}{dt}(E_k)\Delta t_k = \epsilon_i ST_{\gamma i} C \frac{d\tilde{\varphi}}{dt}(E_n)\int_{t_1}^{t_2} dt \langle P_o + P_s\rangle \ , \qquad (49)$$

where the variation of $d\tilde{\varphi}/dt$ over the interval (t_1, t_2) is small. In the present work the integral $\int_{t_1}^{t_2} dt \langle P_o + P_s\rangle$ was calculated with the area-analysis code TACASI.[18] (This Monte Carlo code calculates Doppler

*For example, a 20% change in the neutron width for the 7.65-eV level in ^{183}W produces an 8% change in the calculated capture area between $E_n = 7.26$ eV and $E_n = 8.05$ eV for the sample thickness used in these measurements.

and resolution broadened areas including contributions from adjacent resonances for a flux represented as $d\varphi/dt = KE_n^x$, so that capture areas calculated with $\epsilon_i SK = 1$ and $x = 0$ give the desired integral.) The quantities $(\epsilon_i ST_{\gamma i} C)$ are then determined by comparing the ratio of the observed and calculated areas to the measured flux, and an average of these factors for different isotopes according to Eq. 44 yields the desired factor $(\epsilon_o ST_\gamma C)$.

The range of the capture data taken with the 220-meter flight path does not extend to neutron energies below 70 eV, and the saturated-resonance method was employed for W and Re by taking additional capture data with the 4000-liter scintillator at the 20-meter flight path facility. These data span the energy region 2 eV - 10 keV and overlap the data taken at 220 meters. To improve the accuracy of the normalization, the shape of the neutron flux observed at the 20-meter facility was first smoothed to eliminate small statistical variations by fitting with a minimum χ^2 criterion the flux obtained from the ^{3}He and BF_3 counters with the expression

$$\frac{d\hat{\varphi}}{dt}(E_n) = C' e^{-\beta/\sqrt{E}} E^\gamma \quad , \tag{50}$$

and the optimum values of β and γ were found to be $\beta = 1.39$ and $\gamma = 0.592$. The observed and analytical flux $(d\hat{\varphi}/dt)$ for the 20-meter data are compared in Fig. 30.

The normalization factors $(\epsilon_i ST_{\gamma i} C)$ for the 20-meter capture yields were then obtained from low-energy resonances according to Eq. 49, where $d\varphi/dt \equiv C\, d\hat{\varphi}/dt$. For Re, five resonance capture areas were used for each isotope. For ^{185}Re the resonance energies were 5.92, 7.24, 11.88, 12.88, and 14.64 eV; and for ^{187}Re the following resonances were used: 4.42, 11.14, 16.07, 17.58 and 18.52 eV. The

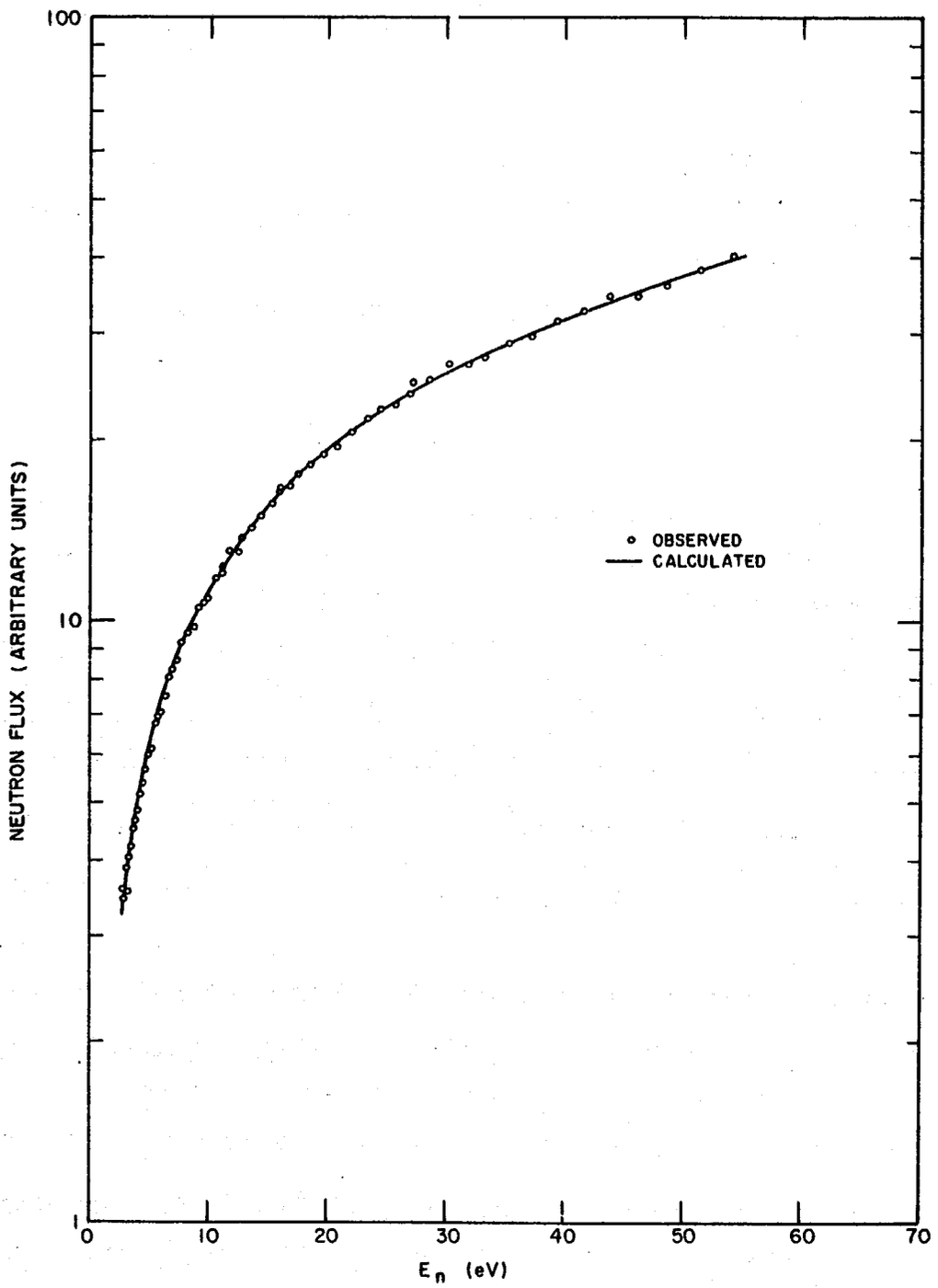

Figure 30. Neutron flux at 20-meter flight path. The curve is the fit to the data using the expression given in the text with $\beta = 1.39$ and $\gamma = 0.592$.

capture areas $\int_{t_1}^{t_2} \langle P_o + P_s \rangle \, dt$ were obtained from the resonance parameters of Ref. 32 and a potential-scattering radius of 8.7 F.[33] The agreement of the observed and calculated resonance shapes was excellent, as is illustrated for typical cases in Fig. 31. Of the ten Re resonances, only those at 7.24 eV in ^{185}Re and at 4.42 eV and 11.14 eV in ^{187}Re were "saturated" ($\langle P_o + P_s \rangle \gtrsim 0.95$ at the resonance energy), although the normalization constants obtained from all the resonances agree closely. For ^{185}Re the five resonances gave an average normalization factor ($\epsilon_i S T_{\gamma i} C$) of 1.71 ± 0.03 (RMS error), and for ^{187}Re we obtained 1.52 ± 0.02, in units convenient to the experiment. The isotopic average according to Eq. 44 then determined the normalization for the 20-meter Re capture data, $(\epsilon_o S T_\gamma C) = 1.58 \pm 0.02$. For W, which has a larger level spacing, only three resonances were suitable, those at 4.16 eV in ^{182}W ($\langle P_o + P_s \rangle = 0.99$), 7.65 eV in ^{183}W ($\langle P_o + P_s \rangle = 0.97$), and 27.13 eV in ^{183}W ($\langle P_o + P_s \rangle = 0.79$). Resonance parameters from BNL 325 and a potential-scattering radius of 6.76 F[33] were used to calculate the capture areas, and ($\epsilon_i S T_{\gamma i} C$) was found to be 1.43 for ^{182}W and 1.61 for ^{183}W, where greater weight was given to the saturated resonance in ^{183}W at 7.65 eV. The uncertainty in these factors due both to the quoted uncertainties in the resonance parameters and to the statistical uncertainties in the observed capture areas is ±2%. To form the isotopic average ϵ_o, the ratios of the efficiencies for ^{184}W and ^{186}W to those of ^{182}W or ^{183}W were determined from the gamma-ray pulse-height distributions of Ref. 19. The present ratio of ϵ_i for ^{182}W to ϵ_i for ^{183}W agrees with that found from these pulse-height distributions to within 1%. The result for the 20-meter W data is $(\epsilon_o S T_\gamma C) = 1.47 \pm 0.04$.

The normalization factors for the W and Re capture data taken at the 220-meter facility were then determined by matching the quotient of the capture data (Figs. 28 and 29 and the flux data (Fig. 17) to the

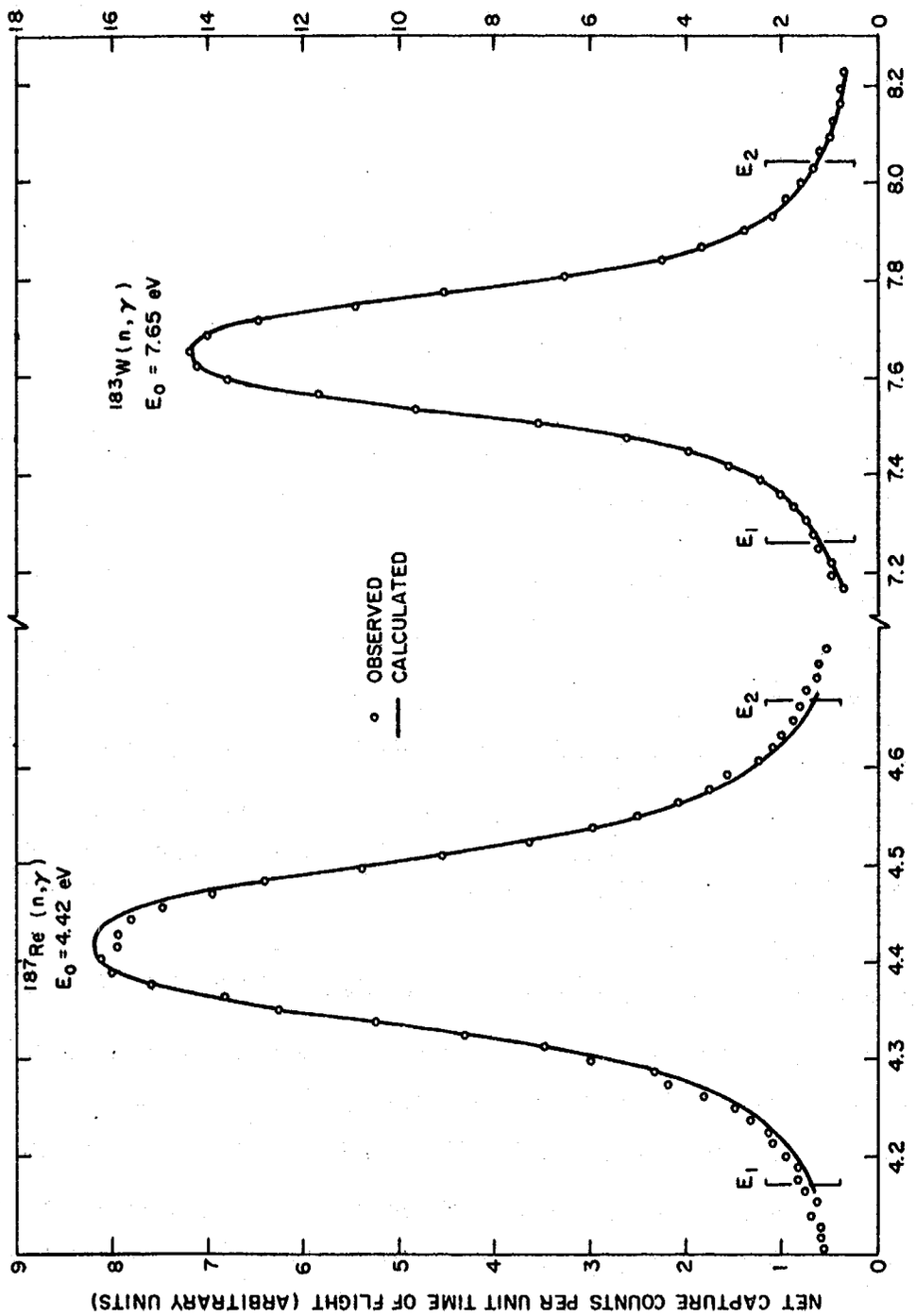

Figure 31. Capture resonances observed at 20-meter flight path facility. The curves are the calculated quantities $\epsilon_i S T_{\gamma i} C \, d\phi/dt\,(E_o) < P_o(E_n) + P_s(E_n) >$ with the factor $(\epsilon_i S T_{\gamma i} C)$ adjusted to reproduce the observed area of the resonance between energy E_1 and energy E_2.

normalized capture yields taken at 20 meters. The two data sets for each sample were matched in the energy region 3-8 keV with an estimated maximum uncertainty of 3% in judging their relative normalizations. (The statistical uncertainties of the 220-meter flux data are less than 3% at all energies.)

4.3 MULTIPLE SCATTERING AND RESONANCE SELF SHIELDING

The average capture cross sections $\langle \sigma_\gamma(E_n) \rangle$ were obtained from the probabilities $\langle P_o(E_n) + P_s(E_n) \rangle$ by taking into account the effects of multiple scattering and resonance self shielding. These effects increase in importance with increasing sample thickness and decreasing neutron energy, and give rise to corrections of 10-20% in the present data at energies lower than 50 keV. The corrections were calculated with the Monte Carlo program SESH[34] which generates a Doppler-broadened resonance cross-section environment for the neutron energy at each collision in a cylindrical sample from distributions of the resonance parameters determined from specified statistical parameters (strength functions, average level spacings, and average radiation widths). The s-, p-, and d-wave strength functions used for the W isotopes were those of Ref. 33. (The d-wave contribution is actually negligible in the energy region where the self-shielding correction is significant, $E_n < 50$ keV.) The s- and p-wave strength functions used for the Re isotopes were those obtained in Ref. 32 from average total and capture cross sections, and the d-wave strength function was taken from Ref. 33. The average radiation widths at low energy for the W isotopes were judged from the data in BNL 325[14] to be 0.057 eV for ^{182}W, ^{184}W, and ^{186}W and to be 0.075 eV for ^{183}W; and the average radiation widths for ^{185}Re and ^{187}Re were taken from Ref. 32. The average observed level spacings at low energy in Re for $\ell = 0$ were taken to be those found in Ref. 32 from average cross sections, and the level spacings for ^{182}W, ^{183}W, and ^{184}W were taken from Ref. 35. The $\ell = 0$ level spacing for ^{186}W, which is not included in Ref. 35, was

adjusted to give best agreement with our data and found to be about 200 eV. The average level spacings for $\ell = 1$ and $\ell = 2$ were obtained from the $\ell = 0$ spacing by assuming the spacing to vary inversely as $\sum_J (2J+1)$, where the sum is over all possible values of the total angular momentum J which are compatible with ℓ. Potential-scattering radii were obtained from Ref. 33. These various parameters produce good agreement with the observed capture probabilities throughout the energy region where the resonance self shielding effect is significant.

The resonance self shielding effect is caused by the resonance structure of the cross section in conjunction with the nonlinear relationship between the cross section and the capture probability. For example, the energy-average of the first-collision capture probability P_o is

$$\langle P_o \rangle = \langle (1-e^{-n\sigma_T}) \frac{\sigma_\gamma}{\sigma_T} \rangle$$

$$\equiv \left[1 - \delta(E_n)\right](1 - e^{-n\langle\sigma_T\rangle}) \frac{\langle\sigma_\gamma\rangle}{\langle\sigma_T\rangle} \quad , \qquad (51)$$

where σ_γ and σ_T are the capture and total cross sections, respectively (Doppler broadened and summed over isotopic contributions), and n is the sample thickness (nuclei per unit area). The difference in $\langle P_o \rangle$ from that given by the average cross sections is then expressed by the positive number $\delta(E_n)$, and $\delta(E_n) = 0$ only when the cross sections vary smoothly over the energy interval of averaging. For W, calculations with the statistical parameters mentioned above give δ(1 keV) = 0.20, δ(7 keV) = 0.04, and $\delta < 0.01$ for $E_n > 50$ keV. For Re, δ(1 keV) = 0.07, and $\delta < 0.01$ for $E_n > 5$ keV.

The calculated fractional multiple scattering contribution $\langle P_s \rangle / \langle P_o + P_s \rangle$ for W was 20% for $E_n = 1$ keV, 15% at 50 keV, and <10% for $E_n > 300$ keV. For Re, $\langle P_s \rangle / \langle P_o + P_s \rangle$ was 20% at 1 keV and less than 10% for $E_n > 50$ keV. For energies higher than the region of

important resonance self-shielding effects, say $E_n > 50$ keV for W and $E_n > 5$ keV for Re, it proved unnecessary to carry out Monte Carlo calculations of the multiple scattering contribution, and an analytical calculation could be used which neglects the effects of neutron energy loss, finite sample radius, and motion of the sample nuclei. Contributions from neutrons captured after one or more inelastic collisions with the sample nuclei were estimated and found to be negligible.

The combined correction for multiple scattering and self shielding (both resonant and non-resonant) can be expressed by writing

$$n\langle\sigma_\gamma(E_n)\rangle = D(E_n)\langle P_o(E_n) + P_s(E_n)\rangle \quad , \tag{52}$$

where D is the total correction to the observed capture probability $\langle P_o + P_s\rangle$ and n is the sample thickness. Self shielding leads to $D > 1$ and multiple scattering to $D < 1$. For W, typical values are D(1 keV) = 1.19 ± 0.06, D(5 keV) = 0.98 ± 0.05, D(10 keV) = 0.87 ± 0.04, and D(50 keV) = 0.91 ± 0.04, where the uncertainties are due to the finite number of Monte Carlo histories used in the calculation. At higher energies, D slowly approaches unity as the effects of (non-resonant) self shielding and multiple scattering diminish. For Re, D(1 keV) = 0.96 ± 0.02, D(5 keV) = 0.91 ± 0.03, and D(10 keV) = 0.93 ± 0.03.

4.4 RESULTS AND DISCUSSION

The average capture cross sections and their total statistical uncertainties are listed in Tables 3 and 4 and are illustrated in Figs. 32 and 33. These uncertainties were obtained by adding in quadrature the statistical uncertainties in the capture and flux data and the uncertainty in the Monte Carlo calculation of $D(E_n)$ described above. In addition to the statistical uncertainties, a total "absolute" uncertainty in the normalization of $\langle\sigma_\gamma(E_n)\rangle$ for $E_n \leq 80$ keV is estimated to be 11% for W and 9% for Re. These were obtained by adding (not in quadrature) the

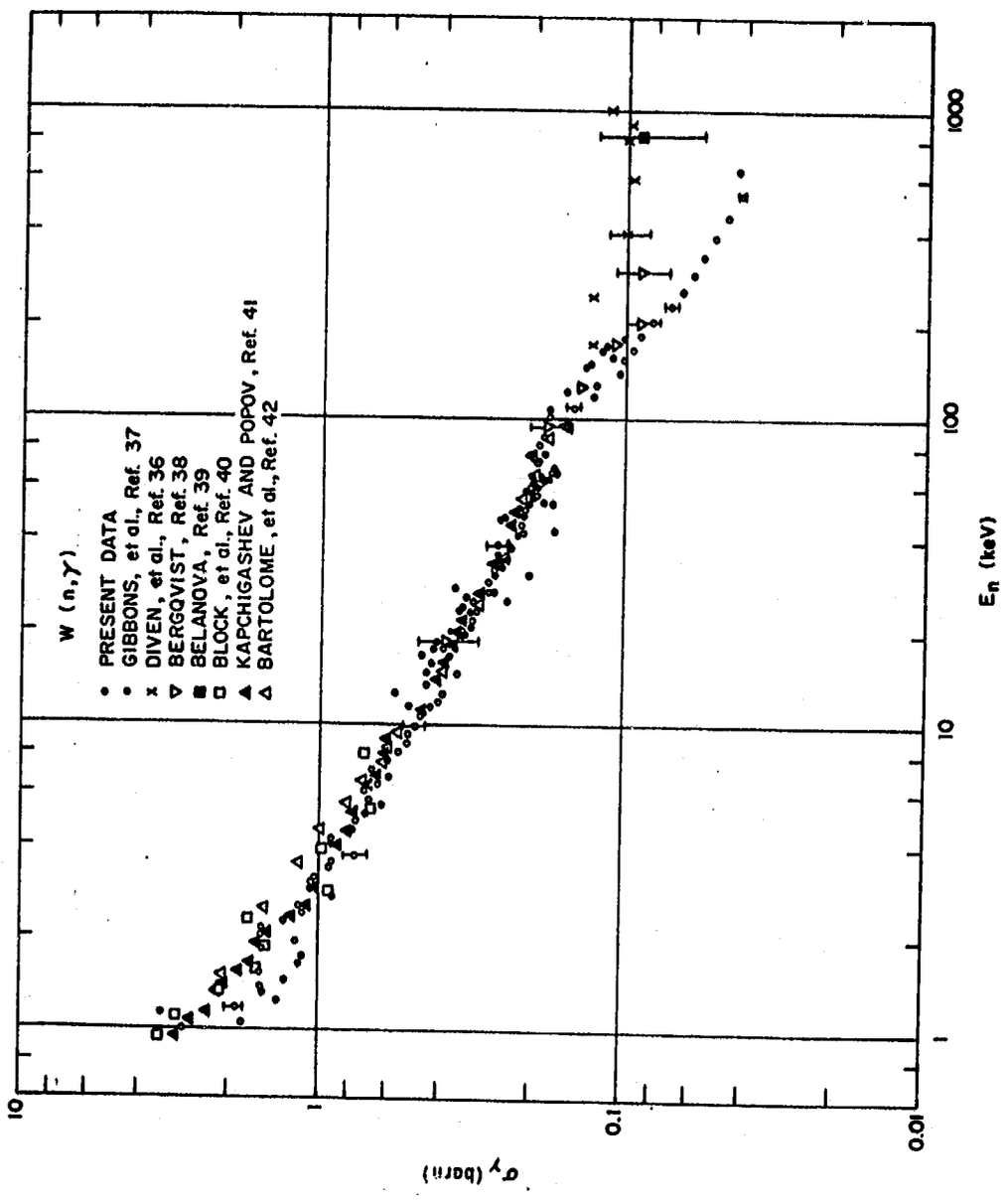

Figure 32. Neutron capture cross sections for tungsten.

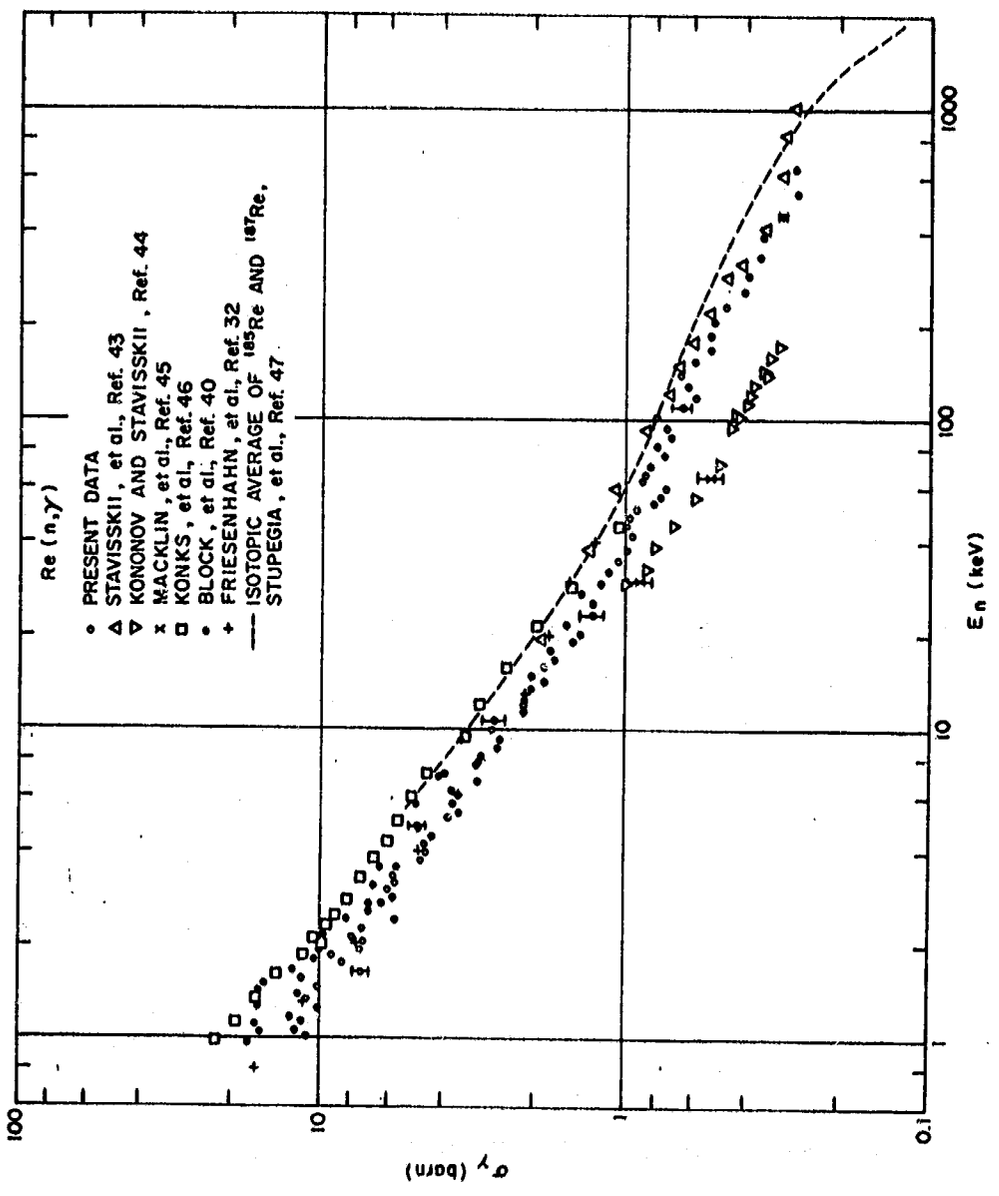

Figure 33. Neutron capture cross sections for rhenium.

Table 3

NEUTRON CAPTURE CROSS SECTION FOR NATURAL TUNGSTEN

Energy (keV)	Cross Section (barn)	Relative Uncertainty (percent)
1.005	2.84	7
1.060	1.80	7
1.120	3.33	7
1.185	1.90	7
1.250	1.38	7
1.316	1.53	7
1.387	1.57	7
1.463	1.30	7
1.547	1.58	8
1.637	1.17	8
1.736	1.12	8
1.834	1.52	8
1.931	1.20	8
2.036	1.54	8
2.150	1.53	8
2.274	1.31	8
2.408	1.12	8
2.555	1.19	8
2.716	.908	9
2.873	1.06	9
3.026	1.06	9
3.190	1.03	9
3.369	.927	9
3.563	.925	9
3.744	.759	9
4.004	.909	9
4.256	.917	9
4.533	.782	9
4.838	.757	9
5.130	.711	9
5.402	.623	9
5.697	.691	9
6.016	.715	9
6.363	.646	9
6.741	.593	9
7.154	.682	8
7.606	.598	8
8.102	.551	8
8.648	.518	8
9.251	.517	8
9.920	.489	8

TUNGSTEN CROSS SECTION (Cont'd.)

Energy (keV)	Cross Section (barn)	Relative Uncertainty (percent)
10.66	.474	8
11.35	.439	8
11.95	.404	8
12.59	.394	8
13.29	.443	8
14.05	.420	8
14.88	.356	8
15.78	.395	8
16.76	.379	8
17.85	.390	8
19.03	.345	8
20.35	.343	8
21.80	.319	8
23.42	.305	8
25.22	.319	8
27.23	.282	8
29.50	.282	8
32.07	.270	8
34.98	.247	8
38.31	.264	8
42.14	.215	8
45.39	.221	8
47.77	.251	8
50.36	.214	8
53.15	.176	8
56.19	.196	8
59.49	.204	8
63.10	.186	8
67.04	.176	7
71.37	.195	7
76.12	.206	7
81.37	.193	7
87.18	.184	7
93.64	.158	7
100.8	.180	6
108.9	.149	6
118.0	.129	6

TUNGSTEN CROSS SECTION (Cont'd.)

Energy (keV)	Cross Section (barn)	Relative Uncertainty (percent)
128.2	.126	6
139.9	.105	6
153.2	.101	5
168.5	.0954	5
186.2	.0899	5
206.9	.0822	5
231.2	.0716	5
260.1	.0648	4
294.7	.0598	4
336.8	.0558	4
388.5	.0508	3
453.2	.0465	3
535.4	.0419	3
642.3	.0430	2

Table 4

NEUTRON CAPTURE CROSS SECTION FOR NATURAL RHENIUM

Energy (keV)	Cross Section (barn)	Relative Uncertainty (percent)
1.005	11.03	6
1.060	12.03	6
1.120	11.52	6
1.185	12.70	6
1.250	10.09	6
1.316	11.06	6
1.387	12.00	6
1.463	10.17	6
1.547	11.56	6
1.637	7.33	6
1.736	8.48	6
1.834	9.20	6
1.931	7.49	6
2.036	7.26	5
2.150	7.95	5
2.274	7.34	5
2.408	5.67	5
2.555	6.99	5
2.716	6.30	5
2.873	5.80	6
3.026	6.03	6
3.190	5.70	6
3.369	5.78	6
3.563	5.60	6
3.774	4.65	6
4.004	4.50	6
4.256	4.59	6
4.533	4.35	7
4.838	4.82	7
5.130	3.81	7
5.402	3.52	7
5.697	3.68	7
6.016	3.55	7
6.363	3.74	7
6.741	3.03	7
7.154	3.93	8
7.606	3.08	8
8.102	3.00	8
8.648	2.66	8
9.251	2.56	8
9.920	2.77	8

RHENIUM CROSS SECTION (Cont'd.)

Energy (keV)	Cross Section (barn)	Relative Uncertainty (percent)
10.66	2.70	8
11.35	2.15	8
11.95	2.17	8
12.59	2.17	8
13.29	2.11	8
14.05	1.83	9
14.88	2.02	9
15.78	1.83	9
16.76	1.71	9
17.85	1.79	9
19.03	1.49	9
20.35	1.40	9
21.80	1.57	9
23.42	1.29	9
25.22	1.29	9
27.23	1.40	10
29.50	1.21	10
32.07	1.13	10
34.98	1.07	10
38.31	.989	10
42.14	.949	10
45.39	.998	10
47.77	.979	10
50.36	.917	10
53.15	.807	10
56.19	.776	10
59.49	.734	9
63.10	.888	9
67.04	.856	9
71.37	.831	9
76.12	.758	8
81.37	.798	8
87.18	.706	8
93.64	.736	7
100.8	.800	7
108.9	.657	7
118.0	.598	7
128.2	.631	7
139.9	.663	6
153.2	.598	6

RHENIUM CROSS SECTION (Cont'd.)

Energy (keV)	Cross Section (barn)	Relative Uncertainty (percent)
168.5	.524	6
186.2	.527	6
206.9	.517	5
231.2	.471	5
260.1	.412	4
294.7	.396	4
336.8	.363	3
388.5	.354	3
453.2	.308	3
535.4	.276	3
642.3	.280	2

systematic uncertainties due to background subtractions, the uncertainties in the normalization constants ($\epsilon_o ST_\gamma C$) for the capture yields measured with the 20-meter flight path, and the uncertainty in judging the normalization of the 220-meter yields relative to the 20-meter data. For $E_n >$ 80 keV, an additional absolute uncertainty of 2% is present from the estimated uncertainty in judging the normalization of the flux data obtained with the CH_4 counter relative to the flux measured with the ^{3}He counters.

Also shown in Figs. 32 and 33 are previous measurements of the capture cross sections for W and Re. The present W data are in reasonable agreement with previous results up to an energy of about 200 keV but differ seriously at higher energies from the previous data, especially those of Diven, et al.[36] This difference is not easily explained, and another complete set of capture data for W was taken at the 220-meter facility to back up the present measurements. The shape of the capture data in the two measurements was reproduced exactly within small statistical uncertainties. Moreover, cross sections reduced from the capture data in this energy region using a flux obtained from the ^{3}He counters and the evaluated[28] ^{3}He(n, p)T cross section are also essentially identical to our final result using the flux obtained with the methane counter. The total, combined correction for the scintillator efficiency, multiple scattering, and self shielding varies by less than 5% over the region 100-700 keV, so that the shape of $<\sigma_\gamma(E_n)>$ is determined to within 5% by simply using the ratio of the observed capture counts to the flux data. It is thus exceedingly difficult to render suspect the shape of the present cross section data at higher energies, and we must only conclude that the present data reflect a considerable improvement in the capability to make this measurement.

The present results for Re at lower energies ($\lesssim$20 keV) support the previous data obtained[32] with the 20-meter flight path at this laboratory for isotopically enriched samples and agree fairly well at high

energies (> 100 keV) with the data of Stavisskii, et al.[43] Except for this; there are significant differences between the present results and all other previous measurements. The disagreement between the present data and those of Konks, et al.,[46] (unpublished) and of Stupegia, et al.,[47] which also span a large energy range, is principally one of normalization. The present data overlap these two sets of data and agree fairly well with both in regard to the shape of the cross section vs energy but disagree with both by about 20% in normalization. The flux data used in the activation measurements of Stupegia, et al., were obtained using White's[48] fission cross sections for ^{235}U, and the total statistical and absolute uncertainties for the capture data are reported to be about 3% and 7%, respectively. Since the estimated absolute uncertainty of the present data is about 10%, the difference of 20% in normalization between the present results and those of Stupegia, et al., seems quite significant.

In summary, this program has resulted in the capability to measure capture cross sections with an absolute uncertainty of about 10% and a statistical uncertainty not exceeding 10% over a neutron energy range of some six orders of magnitude, with the resolution at higher energies shown in Fig. 27. Continuing improvements in the experimental facility will soon result in an even greater capability for making this measurement. A recent modification of the LINAC injector system will allow us to improve the time resolution of the neutron beam by a factor of ten with no sacrifice of intensity. We are installing a ^{6}LiH annular shield in place of the natural boron shield (shown in Fig. 5) which should reduce to negligible proportions the present uncertainty due to the scattered neutron background. The reduced background will also permit us to make a more detailed study of capture gamma-ray spectrum fractions at high energies for the 600-liter scintillator. Theoretical work in progress includes the development of a systematic treatment of average capture cross sections based on the optical model. This study is directed toward

the very attractive possibility of making confident predictions of capture cross sections over a large energy range for materials that have not, or cannot, be measured.

5. CONCLUSIONS

In order to achieve accurate time-of-flight measurements of the neutron capture cross sections required in this contract, we have undertaken an intensive development program to improve capabilities to perform neutron flux measurements over a wide range of energies. Proportional counters containing ^{3}He gas were studied for use in monitoring the incident neutron flux simultaneously with a capture measurement. The response of the ^{3}He counters for different neutron energies less than 80 keV was calibrated against the energy dependence of the $^{10}B(n,\alpha)^{7}Li$ reaction which has a well established (1/v)-behavior in this energy range. At higher energies, the ^{3}He counters were calibrated against the very well known energy variation of the n+p scattering cross section. This was accomplished by devising an on-line data acquisition system that handles correctly the variation of the recoil-proton energy spectrum with incident neutron energy. In addition to providing an improved means of monitoring the neutron flux spectrum in a capture experiment, this work has also resulted in some new cross section data for the reactions $^{3}He(n, p)T$ and $^{10}B(n,\alpha)^{7}Li$.

The neutron capture cross sections for natural tungsten and rhenium were then measured over the energy region 1-700 keV with an over-all statistical uncertainty of less than 10% and an uncertainty in normalization which is also about 10%. Significant differences are found between the present results and previous data. While the difference for $Re(n,\gamma)$ is principally one of normalization, the shape of the cross section for $W(n,\gamma)$ differs seriously at higher energies from that of previous data based on the capture-plus-fission cross section for

^{235}U. We conclude that the present data based on the n+p cross section at higher energies reflect a significant improvement in the capability for making this measurement.

REFERENCES

1. B. Curtis, et al., Rev. Sci. Inst. 20, 388 (1949); also E. Graves, et al., Rev. Sci. Inst. 20, 579 (1949).

2. V. V. Verbinski, et al., Oak Ridge National Laboratory Report, ORNL-3360, September 1962. (Unpublished).

3. B. C. Diven, Phys. Rev. 120, 556 (1960).

4. J. U. Koppel, Nucl. Sci. and Eng. 8, 157 (1960).

5. A. Michaudon, J. of Nucl. Energy, Parts A/B, 17, 165 (1963).

6. S. Glasstone and M. C. Edlund, The Elements of Nuclear Reactor Theory, D. Van Nostrand Co., Inc., N. Y., p. 101 (1952).

7. O. K. Harling, Nucl. Inst. and Methods, 34, 141 (1965).

8. W. N. English and G. C. Hanna, Can. J. of Phys. 31, 768 (1953).

9. J. S. Schwinger, Phys. Rev. 72, 742 (1947).

10. H. Bethe, Phys. Rev. 76, 38 (1949).

11. J. L. Gammel, Fast Neutron Physics, Part II, eds. J. B. Marion and J. L. Fowler, Interscience Publishers, Inc., New York, p. 2185 (1963).

12. J. J. Schmidt, KFK-120, Part I, p. A7 (1966).

13. W. D. Allen and A. T. G. Ferguson, Atomic Energy Research Establishment (Gt. Brit.) Report NP/R1720 (1956).

14. J. R. Stehn, et al., Brookhaven National Laboratory Report BNL-325, Second Ed., Supplement No. 2, p. 6-0-2 (1964).

15. J. B. Parker, et al., Nucl. Inst. and Methods, 23, 61 (1963).

16. F. H. Fröhner and E. Haddad, Nucl. Phys. 71, 129 (1965).

17. E. Haddad, et al., Nucl. Instr. and Methods, 31, 125 (1964).

18. F. H. Fröhner, General Atomic Report GA-6906, August 1966, (unpublished).

19. S. J. Friesenhahn, et al., Nucl. Sci. and Eng. 26, 487 (1966).

20. R. Batchelor, et al., Rev. Sci. Instr. 26, 1037 (1955).

21. S. A. Cox and F. R. Pontet, J. Nucl. Energy, 21, 271 (1967).

22. F. P. Mooring, et al., Nucl. Phys. 82, 16 (1966).

23. K. M. Diment, AERE R 5224 (1967).

24. R. L. Macklin and J. H. Gibbons, Phys. Rev. 165, 1147 (1968).

25. J. Als-Nielsen and C. W. Dietrich, Phys. Rev. 133, B925 (1964).

26. R. Macklin and J. Gibbons, Proc. International Conference on the Study of Nuclear Structure with Neutrons, Antwerp, Belgium (North Holland Pub. Co., Amsterdam, 1966) p. 498.

27. F. L. Shapiro, Soviet Phys. JETP, 7, 1132 (1958).

28. J. J. Schmidt, KFK 120/II (1965).

29. J. Als-Nielsen, CCDN-NW/6, p. 9 (1967).

30. A. A. Bergman and F. L. Shapiro, Soviet Phys. JETP, 13, 895 (1961).

31. U. Fano, et al., Handbuch der Physik, Vol. 38/2, p. 660, Springer-Verlag, Berlin (1959).

32. S. J. Friesenhahn, et al., J. of Nucl. Eng. 22, 191 (1968).

33. K. K. Seth, et al., Phys. Lett, 13, 70 (1964).

34. F. H. Fröhner, Gulf General Atomic Report GA-8380, January 1968, (unpublished).

35. A. Gilbert and A. G. W. Cameron, Can. J. Phys. 43, 1446 (1965).

36. B. Diven, et al., Phys. Rev. 120, 556 (1960).

37. J. H. Gibbons, et al., Phys. Rev. 122, 182 (1961).

38. I. Bergqvist, Arkiv Fysik, 23, 425 (1963).

39. T. S. Belanova, et al., Atomnaya Energiya 19, 3 (1965).

40. R. C. Block, et al., Neutron Time-of-Flight Methods (Saclay Conf.), p. 203 (1961).

41. S. V. Kapchigashev and Yu. P. Popov, Atomnaya Energiya, 15, 120 (1963).

42. Z. M. Bartolome, et al., Rensselaer Polytechnic Institute Report RPI-328-123 (1968) (unpublished).

43. Yu. Ya. Stavisskii, et al., Atomnaya Energiya, 19, 42 (1965).

44. V. N. Kononov and Yu. Ya. Stavisskii, Atomnaya Energiya, 19, 457 (1965).

45. R. L. Macklin, et al., Phys. Rev. 129, 2695 (1963).

46. V. A. Konks, et al., Private Communication to Murray D. Goldberg, et al., (1964). Data given in BNL-325, Second Ed., Suppl. No. 2, p. 75-0-5 (1966).

47. D. C. Stupegia, et al., J. Nucl. Energy, 19, 767 (1965).

48. P. H. White, J. Nucl. Energy, A/B 19, 325 (1965).

NASA DISTRIBUTION LIST

NASA Lewis Research Center
21000 Brookpark Road
Cleveland, Ohio 44135

	Name	No. of Copies	Mail Stop
Attention:	Sam Barile	10	49-2
	Dr. Bernard Lubarsky	1	3-3
	John E. Dilley	1	500-309
	Technology Utiliz. Office	1	3-19
	Library	2	60-3
	Report Control Office	1	5-5
	Donald Bogart	1	49-2
	Donald F. Shook	1	49-2
	John C. Liwosz	1	49-2
	Vincent F. Hlavin	1	3-14

NASA Scientific and Technical Information Facility — 1
Box 5700
Bethesda, Maryland 20014

NASA Ames Research Center — 1
Moffett Field, California 94035
Attention: Library

NASA Flight Research Center — 1
P. O. Box 273
Edwards, California 93523
Attention: Library

NASA Goddard Space Flight Center — 1
Greenbelt, Maryland 20771
Attention: Library

NASA Langley Research Center — 1
Langley Station
Hampton, Virginia 23365
Attention: Library

NASA Manned Spacecraft Center — 1
Houston, Texas 77001
Attention: Library